Rockefeller University
Digital Commons @ RU

Student Theses and Dissertations

2022

Uncovering Regulators of Whole-Body Metabolism by Chemoproteomic Profiling of the Adipocyte Secretome

Chan Hee J Choi

Follow this and additional works at: https://digitalcommons.rockefeller.edu/student_theses_and_dissertations

 Part of the Life Sciences Commons

UNCOVERING REGULATORS OF WHOLE-BODY METABOLISM BY CHEMOPROTEOMIC PROFILING OF THE ADIPOCYTE SECRETOME

A Thesis Presented to the Faculty of
The Rockefeller University
in Partial Fulfillment of the Requirements for
the degree of Doctor of Philosophy

by
Chan Hee J. Choi
June 2022

© Copyright by Chan Hee J. Choi 2022

UNCOVERING REGULATORS OF WHOLE-BODY METABOLISM BY CHEMOPROTEOMIC PROFILING OF THE ADIPOCYTE SECRETOME

Chan Hee J. Choi, Ph.D.
The Rockefeller University 2022

A major threat to human health, obesity is associated with increased risk of cardiometabolic complications such as cardiovascular disease, type 2 diabetes, hypertension, and many types of cancers. Whereas white adipocytes efficiently store energy in the form of triglycerides, thermogenic brown and beige adipocytes can dissipate energy into heat. Adipose tissue is now considered an important endocrine organ, and increasing evidence suggests that divergent metabolic effects of different types of adipocytes are in part mediated by their secretory function. In addition, dysregulation of adipose tissue's secretory function in the setting of chronic positive energy balance plays a central role in the pathophysiology of obesity and its complications. However, the vast majority of bioactive peptides secreted by adipose tissue, collectively referred to as adipokines, remain uncharacterized. We employed bio-orthogonal non-canonical amino acid tagging (BONCAT) and mass spectrometry to comprehensively characterize the secretome of murine visceral and subcutaneous white adipocytes and interscapular brown adipocytes. Over 600 proteins were identified, the majority of which showed cell type specificity with functional enrichment. BONCAT was also applied *in vivo* to label and characterize the nascent serum proteome of mice, and bioinformatic analyses suggested that adipose tissue is an important contributor to the serum proteome. We here describe two candidate adipokines identified from these profiling studies, C11orf54 and leucine-rich α-2 glycoprotein 1 (LRG1). C11orf54 was shown to be a cold-induced, brown/beige enriched protein. Despite the lack of a signal peptide, the long isoform (isoform 1) of C11orf54 was validated to be a *bona fide* secreted factor, while the short isoform (isoform 2) was predominantly intracellular. Functional studies with mice lacking C11orf54 isoform 1 suggest that it may regulate total body energy expenditure. Further studies will be performed to validate and decipher the molecular mechanism underlying this physiological effect. LRG1 was identified as an obesity-regulated adipokine secreted by mature adipocytes. Plasma LRG1 levels were increased in aged and diet-induced obese (DIO) mice. LRG1 overexpression significantly improved glucose and insulin tolerance in DIO mice, despite equivalent body weights. AAV-mediated longitudinal overexpression of LRG1 in the *db/db* model of type 2 diabetes resulted in accelerated weight gain due to increased white fat mass, but improved insulin tolerance and a delayed diabetic phenotype. This effect was associated with markedly reduced macrophage accumulation in white adipose tissues and a dramatic reduction in systemic inflammation. At the molecular level, LRG1 was shown to bind extracellular cytochrome *c* (Cyt *c*), whose levels in serum increased with both diet-induced and genetic obesity. LRG1's ability to bind Cyt *c* led to dampening of Cyt *c*'s pro-inflammatory effect on the macrophage innate immune signaling pathway. These data support a new role for LRG1 as an insulin sensitizer and modulator of inflammation with therapeutic potential. Overall, the work described here provides a thorough characterization of the secretome of white and brown adipocytes, and functional studies on previously undescribed adipokines elucidate novel mechanisms at the intersection of obesity, inflammation, and associated pathology.

This thesis is dedicated to my family

ACKNOWLEDGMENTS

Paul, I was told that PhD trainees end up resembling their mentors in many ways, and I am privileged to have spent my formative years of development as a young scientist under your mentorship. Your guidance, our scientific discussions, and our almost daily interactions over the past six years were everything I hoped to gain from a thesis advisor and much more. Thank you for providing me with the freedom to explore whatever topics I am interested in. I still remember the day you approached me during my rotation and briefed me on the challenges involved in studying secreted factors. You asked if my undergraduate background in chemical biology suggested any methods to address them, to which my answer at the time was no. I did follow up by saying I will keep thinking about it, and it surprises me to this day how that seemingly random conversation eventually led to all the work presented here in this thesis. Your patience and encouragement helped me survive during the most difficult times. I am extremely proud of what the lab has achieved under your leadership, and look forward to many more to come. Thank you.

Thank you to my faculty advisory committee members, Drs. David Allis, Rick Lifton, and James Lo, for providing your insights and feedback over the years. I am honored just to be able to share my work with such renowned experts, let alone receive scientific feedback. Thank you, Dr. Alan Saltiel, for serving as the external examiner and providing helpful feedback. Your work on inflammation and metabolic diseases inspired my thesis project in many ways.

I would also like to thank the Rockefeller University Resource Centers for providing help on various aspects of the work presented here. Thank you, Henrik Molina of the Proteomics Resource Center, for teaching me how to prepare samples for mass spectrometry and analyze proteomic datasets. Thank you, Tom Carroll of the Bioinformatics Resource Center, for providing sophisticated bioinformatic analyses. Thank you, Chingwen Yang and members of the CRISPR and Genome Editing Center, for generating the KO mouse lines for us. Many thanks to Bioimaging Resource Center for teaching me how to use the microscope, Genomics Resource Center for processing our sequencing samples, and Comparative Bioscience Center for maintaining our mouse colonies.

Thank you, Tri-Institutional MD-PhD program directors and staff members, for supporting me to pursue my passion. I still vividly remember how happy I was when I received the acceptance phone call, and matriculating into this program is one of the best decisions I have made. Thank you, Rockefeller University Dean's Office, for always being so helpful and keeping me on track.

To all my former and current colleagues of the Cohen lab, thank you so much for bearing with me all these years. Will, thank you for all the help you provided on almost every aspect of this work. All the preparations you provided for our mouse work and the long hours spent together in the mouse procedure room will not be forgotten. Your dedication and passion for science sustained me during the difficult times. I am very proud of what you accomplished, and look forward to many more that you will achieve as a graduate student at M.I.T. Audrey, thank you for your contribution to this work during its relative infancy. Our efforts back then may not have led to specific figures, but they were fundamental to everything that followed. Thank you, Jingyi, for being a wonderful colleague. You shaped the lab in many ways, and I am lucky that my time in the lab almost completely overlapped with you. Thank you, Mascha, for sharing your

expertise on immunology. I feel extremely fortunate that around the time you joined the lab, my project's direction also turned towards inflammation. Thanks, Kaja, for organizing lab gatherings and continuing with many of the proteomics effort. I am certain and hopeful these efforts will soon come to fruition. Thank you, Sarah Szwed, for being such a positive force in the lab. The help you provided during the shutdown was essential to this work. Rico, thank you for helping with the imaging efforts, and I look forward to where your efforts will lead. Thank you, Aarthi, François, and Xiaojing, for all the advice and for being such friendly colleagues. Many thanks to former members of the Cohen lab, including Lily, Sarah, Sean, and Olivia. Thank you, Tobias, for having been my bay mate, and I am very happy that your work is generating a lot of interest. I miss the lasagna lunch and hanging out with your cats.

I am extremely grateful to my friends and family for all the support they have been providing. Thank you, Dr. Hyosung Lee, for introducing me to science and teaching me chemistry. Thank you to my sister, brother-in-law, and nephew; you all bring so much joy to our family. Thank you, mom and dad, for all your dedication. I would not have made it this far without your vision and support.

Last but not least, I would like to express my deepest gratitude to Annsea Park. These past years with you have been the happiest and most meaningful years in my life. I could not be more fortunate to be with someone who can help each other grow both personally and professionally. I cannot wait to see what the future holds for us.

TABLE OF CONTENTS

LIST OF FIGURES

LIST OF TABLES

LIST OF ABBREVIATIONS

AAV	Adeno-associated virus
Ad	Adenovirus
Adipoq	Adiponectin
AHA	L-Azidohomoalanine
ANCOVA	Analysis of covariance
ANOVA	Analysis of variance
B6	C57BL/6J
BAT	Brown adipose tissue
BMI	Body mass index
BMDM	Bone marrow-derived macrophage
BP	Biological process
C11orf54	Chromosome 11 open reading frame 54
CFD	Complement factor D/adipsin
CM	Conditioned media
CuAAC	Copper(I)-catalyzed azide-alkyne cycloaddition
Cyt *c*	Cytochrome *c*
Cxcl10	C-X-C motif chemokine ligand 10
DAMP	Damage-associated molecular pattern
db/db	C57BLKS-*Lepr*^{db} homozygote
DIO	Diet-induced obesity
eGFP	Enhanced green fluorescent protein
ER	Endoplasmic reticulum
eWAT	Epididymal white adipose tissue
Fabp4	Fatty acid-binding protein 4
FBS	Fetal bovine serum
FL	FLAG tag
GO	Gene Ontology
gRNA	Guide ribonucleic acid
GSEA	Gene set enrichment analysis
GTT	Glucose tolerance test
HFD	High fat diet
iBAQ	Intensity-based absolute quantification
Il1b	Interleukin 1 beta
Il6	Interleukin 6
iWAT	Inguinal white adipose tissue
IP	Immunoprecipitation
IP-10	Interferon gamma-induced protein 10
ITT	Insulin tolerance test
kDa	Kilodalton
KO	Knockout
LFQ	Label-free quantification
LRG1	Leucine-rich α-2 glycoprotein 1
LRR	Leucine-rich repeat
MCP-1	Monocyte chemoattractant protein 1
Met	L-Methionine

MIG	Monokine induced by gamma interferon
MIP-1α	Macrophage inflammatory protein-1 alpha
MS	Mass spectrometry
m/m	C57BLKS-*Dock*^{7m} homozygote
NAFLD	Non-alcoholic fatty liver disease
NASH	Non-alcoholic steatohepatitis
Nos2	Nitric Oxide Synthase 2
ORF	Open reading frame
PBS	Phosphate-buffered saline
PCA	Principal Component Analysis
Pparg	Peroxisome proliferator-activated receptor gamma
Prdm16	PR-domain containing protein 16
RBP4	Retinol binding protein 4
RT	Room temperature
RT-qPCR	Reverse transcription-quantitative polymerase chain reaction
SubQ	Subcutaneous
STS	Staurosporine
SVF	Stromal vascular fraction
TAMRA	Tetramethylrhodamine
TLR4	Toll-like receptor 4
TNFα	Tumor necrosis factor alpha
tSNE	t-distributed stochastic neighbor embedding
Ucp1	Uncoupling protein 1
Visc	Visceral
WT	Wild type

CHAPTER 1. INTRODUCTION

1.1 Obesity as a major public health threat

With close to half of adults in the U.S. and over 1 billion worldwide projected to be obese by 2030, obesity is a major threat to human health (Ward et al., 2019). As excess adiposity is associated with increased risk of various obesity-related diseases such as cardiovascular disease, type 2 diabetes, hypertension, and many types of cancers (Poirier et al., 2006), this dramatic rise in prevalence has profound implications from a public health perspective. Indeed, obesity is now a leading cause of preventable, premature death, second only to smoking (Angelantonio et al., 2016; Masters et al., 2013). The estimated medical costs of obesity in 2008 was $147 billion per year, a sharp rise from $78.5 billion in 1998 (Finkelstein et al., 2009). These data highlight the need to better understand the mechanisms linking excess adiposity and its complications. Such efforts have the potential to lead to the development of novel therapeutic approaches to treat obesity and its sequelae.

1.2 Fat distribution and health outcomes

Body mass index (BMI) remains the gold standard for diagnosing patients with obesity, but increasing evidence suggests that the pattern of fat distribution is also an important marker of metabolic outcome. Waist circumference, a measure of intra-abdominal or visceral (Visc) adiposity, can be a stronger predictor than BMI for cardiometabolic conditions including diabetes, dyslipidemia, and coronary heart disease (Klein et al., 2007). On the other hand, lower body or subcutaneous (SubQ) adiposity is thought to be benign or even protective (Fox et al., 2007; Porter et al., 2009).

Lipectomy or transplantation studies of fat depots provide evidence that intrinsic properties of Visc and SubQ adipocytes contribute to these differences in metabolic effects. Studies in rodents have shown that surgical removal of various Visc adipose tissues, most often gonadal or perinephric or both, improve insulin resistance, whereas removal of SubQ fat depots do not confer the same benefit (Gabriely et al., 2002; Shi et al., 2007). Transplantation of SubQ fat from a donor mouse into the abdominal cavity of a recipient mouse leads to a decrease in overall body fat and improvement of glucose homeostasis, whereas a similar transplantation procedure with a Visc adipose tissue does not lead to any difference in metabolic phenotype compared to sham (Tran et al., 2008).

The disproportionate effect on whole-body metabolism brought about by transplantation of a relatively small amount of tissue also suggests a potential role for secreted factors mediating the effects to a systemic level. Dysfunctional adipose tissue in the setting of excess fat accumulation and subsequent dysregulation in endocrine function contribute significantly to the pathophysiology of obesity and its sequelae. Visc fat in obesity is particularly susceptible to inflammation with increased infiltration of immune cells such as macrophages, leading to greater production of pro-inflammatory cytokines and chemokines (Tchkonia et al., 2013). The degree of macrophage infiltration in the omental fat and lower circulating adiponectin levels are predictors of insulin resistance in obese individuals (Klöting et al., 2010). Inflammation that occurs as a consequence of obesity plays a direct causative role in development of insulin resistance (Saltiel & Olefsky, 2017). These data therefore suggest inflammation and disruption of endocrine function as important mechanistic links between Visc adiposity and metabolic disease.

1.3 Different types of adipocytes

Although the above classification scheme based on anatomical location distinguishes SubQ and Visc fat, both are white adipose tissue (WAT) depots, which contain white adipocytes that are efficient at storing excess energy in the form of triglycerides. Mammals possess another type of adipose tissue, called brown adipose tissue (BAT). Brown adipocytes can dissipate energy into heat through a process known as non-shivering thermogenesis. This process is mediated by a mitochondrial protein called UCP1, which uncouples the mitochondrial electron transport chain from ATP synthase (Fedorenko et al., 2012). Although BAT was initially thought to be present only in small hibernating mammals and infants for humans, studies with PET-CT scans have shown that adult humans also possess BAT interspersed around the supraclavicular region (Cypess et al., 2009; Virtanen et al., 2009; van Marken Lichtenbelt et al., 2009). In addition, human BAT may serve to protect against not only hypothermia but also obesity and related diseases. Active BAT is associated with enhanced energy expenditure (Yoneshiro et al., 2011), insulin sensitivity (Lee et al., 2014), and overall cardiometabolic health (Becher et al., 2021).

Rodent studies have demonstrated that adipocytes within each depot originate from separate lineages and exhibit distinct characteristics (Chau et al., 2014; Shao et al., 2019). In addition to white and brown adipocytes, recent studies have identified a third type of adipocyte, called beige adipocytes. Beige adipocytes are similar to brown adipocytes in their ability to dissipate energy as heat via uncoupled respiration, but arise within WAT from a distinct lineage (Wang & Seale, 2016). Whereas Visc WAT contains predominantly white adipocytes, SubQ WAT has been shown to contain a mixture of white and thermogenic beige adipocytes. Analyses of transcriptomic profiles have demonstrated that murine beige adipocytes demonstrate a molecular signature that resembles that of human brown adipocytes (Sharp et al., 2012; Shinoda et al., 2015; Wu et al., 2012). In addition, studies using transgenic mouse models with increased beige fat mass but with deletion of *Ucp1* have shown that UCP1 is completely dispensable for thermogenic function and promoting metabolic benefit (Ikeda et al., 2017). These studies highlight the need to better understand the biology of white, beige, and brown adipocytes beyond their bioenergetic functions to be able to harness their functions for therapeutic purposes.

1.4 Adipose tissue as an endocrine organ

1.4.1 Adipokines: bioactive peptides secreted by adipose tissue

Adipose tissue was originally viewed as a form of connective tissue that functions as a passive storage depot for excess nutrients. However, several seminal studies in the 1990s changed this notion by demonstrating that adipose tissue is a dynamic endocrine organ that secretes polypeptides and other small molecules that can signal to other organs to coordinate energy homeostasis. This section describes recent advances in understanding and characterizing the adipose secretome and the effect of these factors on metabolic health and disease.

The appreciation of adipose tissue as an endocrine organ was largely effected by the discovery of leptin, which was identified by positional cloning of the gene mutated in *ob/ob* mice (Zhang et al., 1994). In the absence of leptin, these mice are hyperphagic, morbidly obese, and have a constellation of metabolic and endocrine abnormalities consistent with a state of perceived starvation (Ahima et al., 1996). Leptin is now appreciated to be the afferent signal in a homeostatic feedback pathway that regulates food intake and energy expenditure, with low leptin levels driving

increased food intake and reduced energy expenditure and increased leptin levels promoting decreased food intake and increased energy expenditure. However, most obese individuals have elevated leptin levels and are leptin resistant, which has limited the efficacy of leptin as a treatment for obesity (Heymsfield et al., 1999; Maffei et al., 1995), though it can provide important therapeutic benefits in patients with lipodystrophy (Oral et al., 2002).

Adiponectin is an adipose-derived hormone that has also been the subject of intense study since its discovery in 1995 (Scherer et al., 1995). Adiponectin is a 30 kDa protein that can form higher order, multimeric complexes. Adiponectin signals to a number of tissues to promote beneficial metabolic effects, including increased insulin sensitivity and decreased inflammation. Among the best characterized actions of adiponectin is its ability to increase insulin sensitivity in the liver, resulting in decreased hepatic glucose production (Berg et al., 2001; Combs et al., 2001). Adiponectin levels are decreased in the setting of obesity, and strikingly, transgenic overexpression of adiponectin allows maintenance of metabolic health even in morbidly obese, leptin-deficient mice (Kim et al., 2007). Adiponectin signals through two receptors, AdipoR1 and AdipoR2, which are widely expressed (Yamauchi et al., 2003). The effects of adiponectin appear to be dependent on receptor-mediated increases in ceramidase activity, resulting in decreased intracellular ceramide concentrations (Holland et al., 2011). A recent study showed that adiponectin receptors themselves possess ceramidase activity (Vasilliauskaite-Brooks et al., 2017).

These groundbreaking studies on leptin and adiponectin have served as a model for a growing field of research investigating the function of adipose-derived endocrine factors. Interestingly, the first described adipose secreted factor was adipsin, a circulating serine protease whose levels decrease markedly in the setting of obesity (Cook et al., 1987; Flier et al., 1987). Adipsin was subsequently shown to be identical to complement factor D (CFD) (Rosen et al., 1989), though its physiological role was unclear for many years. Recently, adipsin-mediated generation of complement component C3a has been shown to signal to pancreatic β cells to promote insulin secretion (Lo et al., 2014) by preserving β cell function (Gómez-Banoy et al., 2019).

Now considered an important endocrine organ, adipose tissue has been shown to secrete a large number of bioactive peptides, collectively referred to as adipokines. Moreover, BAT-specific secreted factors, called batokines, are increasingly appreciated as important contributors to the benefits associated with BAT activation beyond thermogenic function (Cohen and Kajimura, 2021; Villarroya et al., 2017). Some of these factors and their functions are listed and summarized in **Table 1.1.**

Table 1.1. Selected list of adipokines and their functions

Adipokine	Main Functions
Adiponectin	Increases insulin sensitivity; decreases inflammation
Adipsin	Activates alternative complement pathway; promotes insulin secretion in pancreatic β cells
ANGPTL2	Pro-inflammatory; atherogenic
Apelin	Stimulates glucose uptake in skeletal muscle and adipose tissue; decreases insulin secretion in pancreatic β cells
Asprosin	Stimulates hepatic glucose release
BMP-4	Promotes adipogenesis and browning of WAT
BMP-7	Promotes brown adipogenesis and mitochondrial biogenesis; increases energy expenditure; decreases food intake
BMP-8b	Enhances BAT response to β3-adrenergic stimulation; activates sympathetic output; induced by estrogens and may contribute to sex-differences in BAT activity
Chemerin	Chemotaxis of dendritic cells and macrophages; regulates adipogenesis
CTRP family	Glucose-lowering effects; anti-inflammatory
Endotrophin	Stimulates fibrosis, endothelial cell migration and macrophage infiltration; promotes insulin resistance
FGF21	Increases hepatic fatty acid oxidation; promotes adipogenesis and browning of WAT; anti-inflammatory effects
Lipocalin 2	Associated with insulin resistance
Leptin	Regulates appetite and energy expenditure
NRG4	Attenuates hepatic lipogenesis; promotes neurite outgrowth
Omentin-1	Enhances insulin-stimulated glucose uptake; anti-inflammatory; anti-atherogenic
Progranulin	Associated with diet-induced obesity and insulin resistance; may promote tissue remodeling and angiogenesis
RBP4	Promotes insulin resistance; stimulates hepatic gluconeogenesis
Resistin	Promotes insulin resistance, inflammation, and endothelial dysfunction
SFRP5	Suppresses oxidative metabolism and promotes adipocyte growth by inhibiting WNT signaling
Slit2-C	Stimulates adaptive thermogenesis
TNFα	Pro-inflammatory; impairs insulin signaling
Vaspin	Improves glucose tolerance and insulin sensitivity; reduces food intake

1.4.2 Secreted enzymes

In addition to signaling biomolecules, recent discoveries have highlighted the role of adipose-derived secreted proteins with catalytic activities, facilitating propagation of necessary nutrients, metabolites, and cofactors to distant tissues. With the broad physiologic impact they can have in orchestrating whole-body metabolism and the relative ease with which they can be targeted therapeutically, these secreted enzymes will likely constitute a crucial component of the adipose tissue secretome.

eNAMPT (Visfatin or PBEF)

The gene product of *Nampt* has been known by many names; it was called pre-B-cell colony-enhancing factor (PBEF) for its role in synergizing the activity of cytokines that promote pre-B-cell colony formation (Samal et al., 1994) and visfatin for its proposed role as a visceral-enriched adipokine that can bind to and activate insulin receptors (Fukuhara et al., 2005, 2007). Subsequent studies, however, had difficulty replicating the visceral-enriched expression pattern (Berndt et al., 2005) or its activation of insulin receptors (Revollo et al., 2007).

NAMPT is an enzyme, nicotinamide phosphoribosyltransferase, which catalyzes the formation of nicotinamide mononucleotide (NMN), the rate-limiting step of nicotinamide adenine dinucleotide (NAD+) biosynthesis (Rongvaux et al., 2002). The enzyme is secreted by brown and white adipocytes and is present in both intracellular and extracellular compartments (Revollo et al., 2007). The intracellular form (iNAMPT) is acetylated, and under fasted conditions, SIRT1-mediated lysine deacetylation leads to its secretion as an extracellular enzyme (eNAMPT) (Yoon et al., 2015). eNAMPT contributes significantly to the circulating NMN pool, providing building blocks for NAD+ synthesis in pancreatic β-cells to support insulin secretion (Revollo et al., 2007) and in the hypothalamus to increase locomotor activity (Yoon et al., 2015) and food intake (Brunetti et al., 2012).

The role of eNAMPT in the context of obesity has been a subject of debate. Mice with adipose-specific knockout of NAMPT suffer from multi-organ insulin resistance in the adipose tissue, skeletal muscle, heart, and liver, suggesting that adipose-derived eNAMPT is necessary to maintain whole body glucose homeostasis (Stromsdorfer et al., 2016). Human studies, however, suggest that high serum levels of eNAMPT are associated with obesity and type 2 diabetes (Garten et al., 2015). A possible explanation for these conflicting observations is that while adipose-derived eNAMPT is necessary for cells to respond to insulin, excess secretion of the enzyme in obesity and subsequent dysregulation of NAD+ metabolism may impair glucose homeostasis.

PM20D1

Brown and beige adipocytes specialize in dissipating energy into heat. The classic thermogenic mechanism requires UCP1, an inner mitochondrial membrane protein, which uncouples the electron transport chain from ATP synthesis (Fedorenko et al., 2012). With increased interest in targeting this pathway to increase energy expenditure and promote weight loss, there has been a great expansion of knowledge regarding brown and beige adipogenesis (Wang & Seale, 2016) and regulation of UCP1 expression (Kajimura et al., 2015).

Recent studies suggest that brown and beige adipocytes may not be the only sites where thermogenesis can occur. Long and colleagues identified peptidase M20 domain-containing 1 (PM20D1) as a brown and beige adipose-secreted enzyme that promotes thermogenesis in other tissues that do not express UCP1 (2016). PM20D1 catalyzes condensation of fatty acids and amino acids into N-acyl amino acids and the reverse hydrolysis reaction, of which the former reaction predominates in plasma (Long et al., 2016). These N-acyl amino acids act on distant sites, such as skeletal muscle, to promote uncoupled respiration through an unknown, UCP1-independent mechanism (Long et al., 2016).

How exactly these N-acyl amino acid species promote proton leak is an open question. Preliminary binding assays suggest they may act as a ligand for various mitochondrial membrane proteins of the SLC25 carrier family (Long et al., 2016). The relevance of PM20D1 to human biology is also not yet known. Nevertheless, the enzyme or its product could potentially serve as useful markers of brown/beige fat activity or even as a therapeutic agent to increase energy expenditure.

1.4.3 Lipokines: signaling lipid species secreted by adipose tissue

Adipocytes not only store, but can also secrete various lipid species. Free fatty acids are released by adipocytes as a nutrient source during fasting and provide a link between excess adiposity and insulin resistance (Randle et al., 1963; Roden et al., 1996), prostaglandins such as PGE2 and PGI2 modulate lipolysis and vasodilation (Axelrod et al., 1976; Axelrod & Levine, 1981), and monobutyrin (1-butyryl-glycerol) promotes angiogenesis during adipocyte differentiation (Dobson et al., 1990). With advances in our understanding of the secretory capacity of adipocytes and their lipidomic profile, novel adipose-derived de novo lipogenesis products with endocrine and paracrine functions are starting to be characterized (Yilmaz et al., 2016). In this section, we review newly characterized lipokines, or signaling lipids secreted by adipocytes, as agents of inter-organ communication and regulators of whole-body metabolism.

Palmitoleic acid

Palmitoleic acid and its conjugate base palmitoleate are monounsaturated fatty acids (C16:1n7). Its endocrine function was first described in FABP4/5 double knockout mice, which are protected from diet-induced obesity and its complications (Cao et al., 2008). Lipidomic profiling revealed that adipose tissue from *Fabp4/5*$^{-/-}$ mice produced greater amounts of palmitoleate, which acts in an endocrine fashion to inhibit lipogenesis in the liver and sensitize insulin signaling in the liver and skeletal muscle (Cao et al., 2008). Corroborating these findings, oral administration of palmitoleate in diabetic KK-Ay mice rendered them resistant to diet-induced obesity and improved their glycemic profile (Yang et al., 2011). Acting on macrophages, palmitoleate was also found to have an anti-inflammatory effect (Souza et al., 2017; Chan et al., 2015), which may contribute to insulin-sensitizing effects in the skeletal muscle (Talbot et al., 2014) and protection against atherosclerosis (Çimen et al., 2016).

Whether increased levels of palmitoleate in circulation leads to metabolic benefit in humans has been controversial. Palmitoleate concentrations in serum do seem to correlate with insulin sensitivity, but they also correlate with abdominal obesity and certain types of cancer, with unclear effects on cardiovascular health and hepatic steatosis (Frigolet & Gutiérrez-Aguilar, 2017). Many of these epidemiologic studies are obscured by various forms and sources of palmitoleate present in the serum. In addition, palmitoleate may exist almost exclusively in an inactive, protein-bound form, so the level of bioactive palmitoleate may not correlate with serum levels (Huber & Kleinfeld, 2017). Further research is necessary to characterize how much the adipose tissue contributes to circulating palmitoleate and its role in human metabolic health.

Branched fatty acid esters of hydroxyl fatty acids (FAHFAs)

Branched fatty acid esters of hydroxyl fatty acids (FAHFAs) have been discovered as a novel lipid class with anti-diabetic and anti-inflammatory functions (Yore et al., 2014; Moraes-Vieira et al., 2016). Mice with adipocyte-specific overexpression of Glut4 have improved glucose tolerance despite having greater adiposity and elevated serum fatty acids (Shepherd et al., 1993; Herman et

al., 2012). Profiling the lipidome of SubQ WAT from Glut4-transgenic and WT mice revealed that FAHFAs were highly enriched in fat depots of transgenic mice compared to WT (Yore et al., 2014). In mice, administration of palmitic acid-hydroxy stearic acid (PAHSA), the most highly upregulated species among FAHFAs, was sufficient to improve glucose tolerance by enhancing insulin and GLP-1 secretion and suppressing pro-inflammatory cytokine secretion by macrophages (Yore et al., 2014). Analysis of human serum and fat samples revealed that PAHSA levels correlated with insulin sensitivity, with significantly lower levels found in insulin resistant individuals (Yore et al., 2014). Therefore, deficiency of PAHSA, and more broadly FAHFA, may contribute to glucose intolerance, such that restoring their levels in insulin resistant individuals may be an attractive target to treat diabetes.

1.4.4 Extracellular vesicles

Extracellular vesicles (EVs), small membrane-bound vesicles secreted by cells into the extracellular space, have recently emerged as a mechanism of intercellular communication (Raposo & Stoorvogel, 2013). Generally referred to as exosomes for endosome-derived and microvesicles for plasma membrane-derived vesicles, these circulating particles facilitate cell-cell communication by transporting various bioactive molecules, such as lipids, proteins, and RNA (Raposo & Stoorvogel, 2013).

Initial evidence that adipose tissue can secrete EVs came from in vitro experiments. EVs could be successfully purified by differential centrifugation of conditioned medium obtained from cultured adipose tissue explants (Deng et al., 2009; Koeck et al. 2014) or adipocyte cultures (Ogawa et al., 2010). In addition, EVs obtained from mouse serum (Phoonsawat et al., 2014), differentiated 3T3-L1 cell lines (Ertunc et al., 2015), and rat primary adipocyte cultures (Lee et al., 2015) were found to contain fat-cell specific proteins such as aP2 and adiponectin, suggesting that mature adipocytes can contribute to EVs in circulation. Hence, secretion of EVs may be a novel means through which adipocytes communicate with distant organs and regulate whole-body metabolism under both physiologic and pathophysiologic conditions (Huang-Doran et al., 2017). Here, we focus on studies in which adipose-derived EVs were shown to regulate whole-body metabolism as endocrine mediators.

Adipose-derived EVs and obesity

One of the hallmark changes observed in obese adipose tissue is macrophage accumulation and formation of crown-like structures (CLS) (Weisberg et al., 2003; Lumeng et al., 2007; Ouchi et al., 2011). Although adipocytes secrete various pro-inflammatory cytokines as mediators of this adipocyte-macrophage crosstalk, studies suggest that EVs may also contribute. Deng and colleagues purified EVs from cultured Visc WAT explants of wild-type and *ob/ob* mice, which were subsequently labeled with a fluorescent dye to show that peripheral blood monocytes were one of the major targets of adipose-derived EVs (2009). Functionally, EVs from *ob/ob* mice promoted differentiation of bone-marrow derived monocytes into macrophages with increased pro-inflammatory cytokine secretion compared to those from WT mice; in turn, conditioned medium obtained from macrophages pre-treated with *ob/ob* adipose-derived EVs were able to induce insulin resistance in C2C12 myocytes (Deng et al., 2009). This suggests that adipose-derived EVs may be one of the mediators through which adipocytes communicate with immune cells and induce pathophysiologic changes observed in the setting of obesity, such as insulin resistance.

aP2: crosstalk with liver

aP2, encoded by *Fabp4*, is a member of the fatty acid binding protein superfamily known for its abundant expression in differentiated adipocytes (Hotamisligil & Bernlohr, 2015). While its intracellular function as a lipid chaperone and regulator of lipid signaling has been widely studied, aP2 is also secreted by adipocytes and detected in human serum at high concentrations (Xu et al., 2006). In fact, serum aP2 concentrations positively correlate with BMI and insulin resistance, suggesting circulating aP2 as a potential biomarker of metabolic dysfunction (Xu et al., 2006; Kaess et al. 2012). Recently, work with 3T3-L1 adipocyte cell cultures has shown that aP2 is actively secreted by adipocytes in a regulated fashion, with various lipolytic signals increasing the aP2 concentration in the conditioned medium (Cao et al., 2013). Interestingly, treating adipocytes with various inhibitors of the classical endoplasmic reticulum-Golgi secretory pathway failed to inhibit aP2 secretion (Cao et al., 2013), and it was later demonstrated that aP2 is secreted via a nonclassical exosome-like pathway (Ertunc et al., 2015). Both *in vitro* and *in vivo* experiments demonstrated that recombinant aP2 promotes hepatic glucose production, while neutralization of circulating aP2 by IgG improved glucose homeostasis in obese mice (Cao et al., 2013). Further studies will be needed to characterize to what extent circulating aP2 proteins are in EVs or free in circulation. Other questions that remain include the scope of aP2 action in the body and the mechanism downstream of exosome uptake at target tissues.

EV-associated miRNAs

In addition to proteins, EVs contain nucleic acid species, especially microRNAs (miRNAs) (Zhang et al., 2015). Differential expression of various miRNA species is observed across different fat depots, obese and non-obese states, stages of adipogenesis, and models of inflammation, suggesting their diverse role in post-transcriptional regulation of metabolic homeostasis (Arner & Kulyté, 2015). Metabolic state also affects vesicle-transported miRNAs in circulation. In serum samples obtained from patients with type 1 or type 2 diabetes, distinct profiles of miRNAs are present, some of which could be used as biomarkers (Guay & Regazzi, 2013).

Thomou and colleagues discovered that ADicerKO mice, which lack miRNA processing capability specifically in adipocytes, have reduced exosomal miRNA in circulation, which could be partially rescued by transplantation of adipose tissues, especially BAT (Thomou et al., 2017). Hence, adipocytes may be one of the major contributors of circulating miRNA. In addition, by demonstrating that adipose-derived exosomes could regulate *Fgf21* expression in the liver and that human-specific miRNA-containing exosomes secreted from the BAT of one mouse can regulate luciferase-3'-UTR expression in the liver of another mouse, this finding supports the notion that adipose-derived exosomal miRNAs can signal to other cell types (Thomou et al., 2017). Questions remain as to the extent of target organs other than the liver that adipose-derived exosomal miRNAs act on and whether intercellular communication mediated by exosomal miRNA contributes to regulation of whole-body metabolism.

Adipose-derived EVs and cancer

Obesity is a risk factor for various types of cancers including malignant melanoma (Karimi et al., 2016). Adipocyte exosomes may provide a causal link for this association. Lazar and colleagues demonstrated that treating melanoma cells with 3T3-F442A-derived exosomes can enhance cancer cells' ability to migrate and metastasize to the lungs, and such effects were amplified when

exosomes were derived from adipocytes of obese mice as opposed to those from lean mice (Lazar et al., 2016). Adipose-derived exosomes were enriched with enzymes of the fatty acid oxidation (FAO) pathway, and providing melanoma cells with these proteins seemed to promote an aggressive phenotype, as pharmacologic inhibition of the FAO pathway in cancer cells abrogated the effects of exosome treatment (Lazar et al., 2016). While it remains unknown whether exosomes play a role in promoting other types of malignancies associated with obesity, adipose-derived EVs may serve as a mechanism by which excess adiposity promotes cancer initiation or progression.

1.4.5 Summary of adipose tissue endocrine function

The studies detailed above, along with many others, indicate the central role that adipose tissue plays in coordinating systemic metabolism via crosstalk with other tissues. While a number of adipokines have been extensively studied, bioinformatic analyses predict that adipose tissue secretes >1,000 adipokines, the vast majority of which remain unstudied. Addressing this knowledge gap calls for a detailed characterization of the adipose secretome to better understand how adipocytes communicate with other cells and tissues to coordinate systemic metabolism. Such efforts have the potential to illuminate fundamental biological processes and to identify new therapeutic candidates for treatment of obesity and associated diseases.

1.5 Methods to profile the secretome

Transcriptomic profiling coupled with application of secretion prediction algorithms is often utilized to identify secreted proteins. Many of these bioinformatic tools utilize machine learning algorithms that analyze the primary amino acid sequences to predict the presence of a signal peptide (SignalP5.0), number of transmembrane domains (TMHMM2.0), proteolytic cleavage sites for glycosylphosphatidyl (GPI) anchors (Pred-GPI), and subcellular localization (DeepLoc1.0, SecretomeP2.0) (Almagro Armenteros et al., 2017, 2019; Bendtsen et al., 2004; Krogh et al., 2001; Pierleoni et al., 2008). However, this approach is limited by the accuracy of the prediction software and could omit non-classically secreted factors. Alternatively, direct detection of proteins in medium conditioned by cultured cells could be performed using mass spectrometry (MS), such as liquid chromatography tandem-mass spectrometry (LC-MS/MS). Such proteomic analyses are commonly performed in serum-free conditions because fetal bovine serum (FBS) proteins interfere with detection of relatively low abundance secreted proteins in the conditioned medium (CM). Serum starvation, however, induces a complex and unpredictable response from cultured cells, making physiologic interpretation difficult (Pirkmajer & Chibalin, 2011).

To overcome these limitations, a chemoproteomic technology called BONCAT has been applied for secretome profiling (Dieterich et al., 2006; Eichelbaum, 2012). L-Azidohomoalanine (AHA) is a non-toxic, non-canonical amino acid with structural similarity to L-methionine (Met). AHA can be recognized by cells' native translational machinery and incorporated into the nascent proteome in place of Met. The azide functional group in AHA does not exist in nature, so peptides containing AHA can be targeted for bio-orthogonal chemical conjugation strategies called click chemistry. Applying this technique to cultured adipocytes allows for selective enrichment of low abundance nascent proteins for proteomic analysis of serum-containing CM.

1.6 Summary

Adipose tissue secretes a constellation of bioactive peptides, or adipokines, many of which regulate whole-body energy homeostasis and inflammation. It is becoming increasingly appreciated that different types of adipocytes demonstrate distinct secretory profiles. In obesity, divergent impact on whole-body metabolism conveyed by different types of adipose tissues is likely mediated by changes in their secretory profiles. Dysregulation of adipose tissue endocrine function is therefore a key feature of obesity and a major contributor to its sequelae. We sought to better elucidate these systemic mediators secreted by adipocytes, especially focusing on characterizing the secreted factors that contribute to or protect from development of obesity-related diseases. To that end, we employed BONCAT to comprehensively profile the adipose secretome and nascent serum proteome of mice. From these data, we identified C11orf54, a cold-induced, brown/beige-enriched factor with an unusual mode of secretion. We also identified leucine-rich α-2 glycoprotein 1 (LRG1) as a novel adipokine. We find LRG1 is secreted by mature adipocytes and increased in obesity. While serum LRG1 levels have been shown to be positively correlated with BMI (Pek et al., 2018), the functional relevance of this association was unknown. We demonstrate using *in vivo* models of obesity that LRG1 improves fasting glucose and insulin tolerance and reduces adipose tissue macrophage accumulation. At the molecular level, LRG1 binds extracellular cytochrome *c* (Cyt *c*) released from dead/dying cells and dampens Cyt c's pro-inflammatory effect on macrophages. Together, LRG1 is a crucial regulator of metabolic health as an insulin sensitizer and suppressor of systemic inflammation in obesity. These data provide a comprehensive characterization of the secretome of different types of adipocytes, elucidating novel mediators of whole-body metabolism with therapeutic potentials.

CHAPTER 2. Characterization of adipocyte secretome and nascent plasma proteome using BONCAT

2.1 Introduction

Conventional methods to profile the secretome of cultured cells and tissues have allowed limited interpretation of the results due to various artifacts, such as the need to use serum-free medium. We employed a chemical proteomics approach called BONCAT to profile the secretome of cultured primary adipocytes. L-Azidohomoalanine (AHA) is a non-toxic, synthetic amino acid that bears structural similarity to L-methionine (Met) and can therefore be incorporated into the proteome in place of Met (Dieterich et al., 2006) (**Figure 2.1**). Since azide functional groups do not exist in nature, selective and robust chemical conjugation methods such as copper(I)-catalyzed azide-alkyne cycloaddition (CuAAC), or click chemistry, can then be performed to specifically label or enrich for AHA-labeled peptides. This approach can be applied to proteomic analysis of conditioned medium (CM). Culturing cells in FBS-supplemented growth medium that contains AHA instead of Met leads to metabolic labeling of the secretome with AHA, which can in turn be covalently conjugated with alkyne agarose beads to selectively enrich for proteins that are actually secreted by cultured cells. By subjecting the conjugated beads to rigorous washing conditions, most of the FBS proteins can be removed, after which the enriched peptides on the beads can be directly digested and subjected to MS analysis. This method has been shown to provide secretome profiles that are better reflective of the physiologic state of the cells without any bias against proteins with low Met content (Eichelbaum et al., 2012).

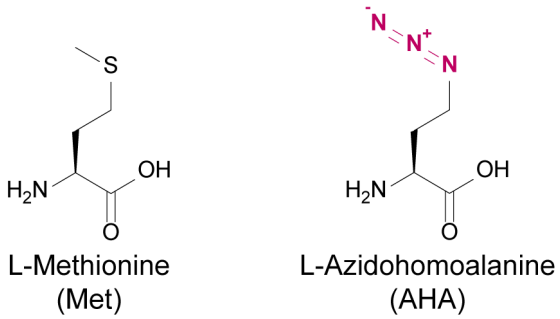

Figure 2.1. Chemical structures of L-Methionine (Met) and L-Azidohomoalanine (AHA)

The BONCAT method can also be applied to study proteomes *in vivo*. Previous studies have shown that AHA can be administered via the diet or intraperitoneal (IP) injection, enabling successful metabolic labeling of tissue proteins (Calve et al., 2016; McClatchy et al., 2015). However, it has not been tested whether this method can be used to label the nascent serum proteome in mice. With the goal of identifying novel circulating factors that regulate whole-body energy homeostasis, we applied the BONCAT technology to profile the secretome of primary adipocytes *in vitro* and the nascent serum proteome *in vivo*.

2.2 Employing BONCAT to profile the secretome of primary adipocytes

2.2.1 Overview of the BONCAT workflow

To profile the secretome of different types of primary adipocytes, stromal vascular fraction (SVF) from epididymal white adipose tissue (eWAT), inguinal white adipose tissue (iWAT), and interscapular brown adipose tissue (BAT) from 7-week-old male C57BL/6J (B6) mice was differentiated *in vitro* into primary Visc, SubQ, and Brown adipocytes, respectively. Adipocytes

were pulsed with Met-deficient media containing 0.1 mM AHA or 0.1 mM Met as negative controls for 24 hours, after which CM was collected (**Figure 2.2**).

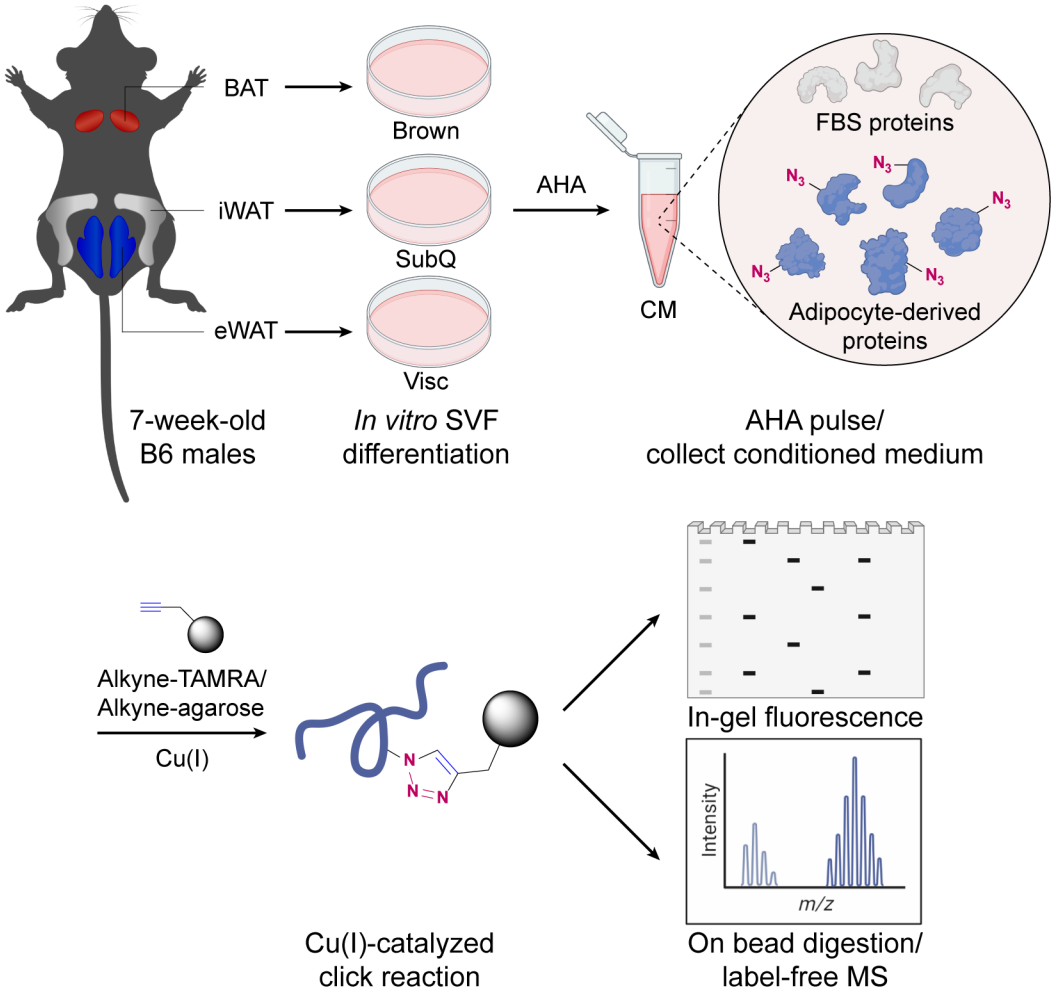

Figure 2.2. Schematic diagram of MS-based secretome analysis from primary Visc, SubQ, and Brown adipocytes using BONCAT

Of note, all three cell types showed comparable lipid droplet accumulation (**Figure 2.3A**) and expression of mature adipocyte markers such as *Fabp4*, *Pparg2* and *Adipoq* (**Figure 2.3B**). *In vitro* primary adipocytes recapitulated characteristic gene expression patterns observed *in vivo*, with expression of brown-enriched genes such as *Prdm16* and *Ucp1* highest in Brown, intermediate in SubQ, and lowest in Visc (**Figure 2.4**).

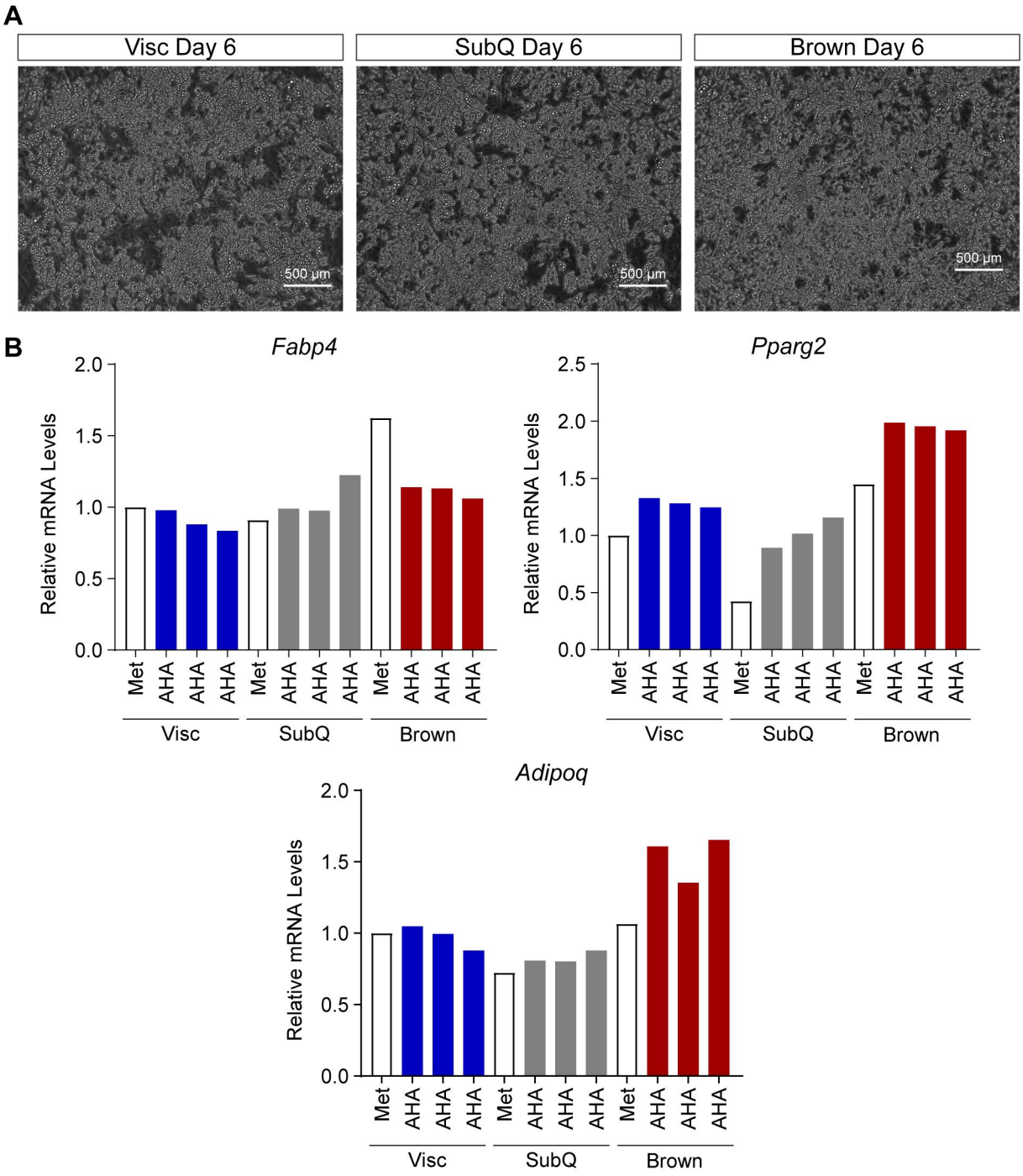

Figure 2.3. Validation of primary adipocyte differentiation

(**A**) Phase-contrast microscope images of mature Visc, SubQ, and Brown adipocytes on day 6 of differentiation. Scale bars are indicated. (**B**) Relative mRNA levels of mature adipocyte genes.

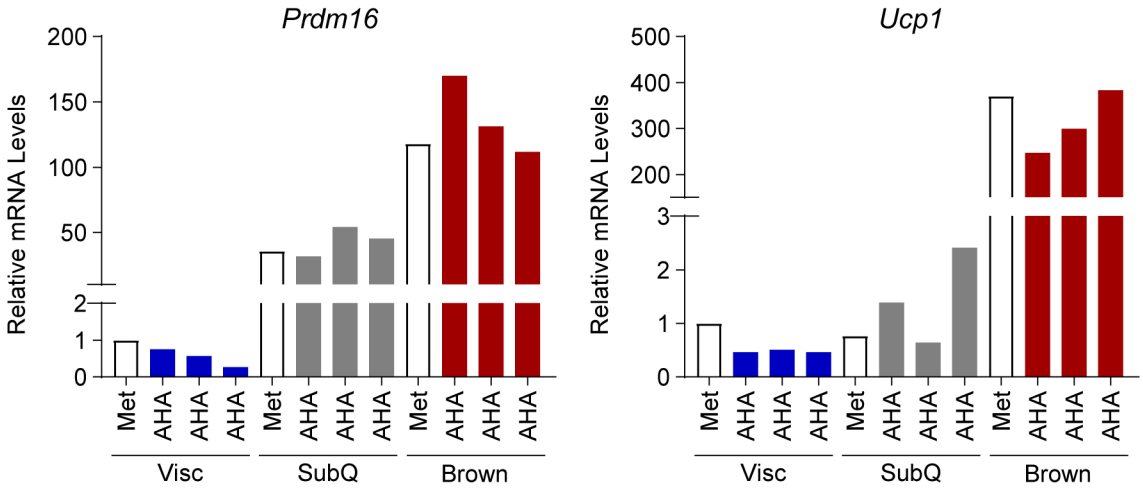

Figure 2.4. Primary adipocytes recapitulate *in vivo* gene expression signature
Relative mRNA levels of brown adipocyte-enriched genes, *Prdm16* and *Ucp1*.

To visualize azide-labeled secreted proteins, CM was subjected to a copper-catalyzed azide-alkyne cycloaddition (CuAAC) reaction with tetramethylrhodamine (TAMRA)-alkyne. In-gel fluorescence analysis of AHA-treated CM proteins highlighted adipocyte-derived proteins as bands positive for TAMRA fluorescence, while CM from control Met-pulsed adipocytes showed minimal background signal (**Figure 2.5**). Differential fluorescent band patterns were observed across the three types of adipocytes, suggesting cell type-specific secretory profiles.

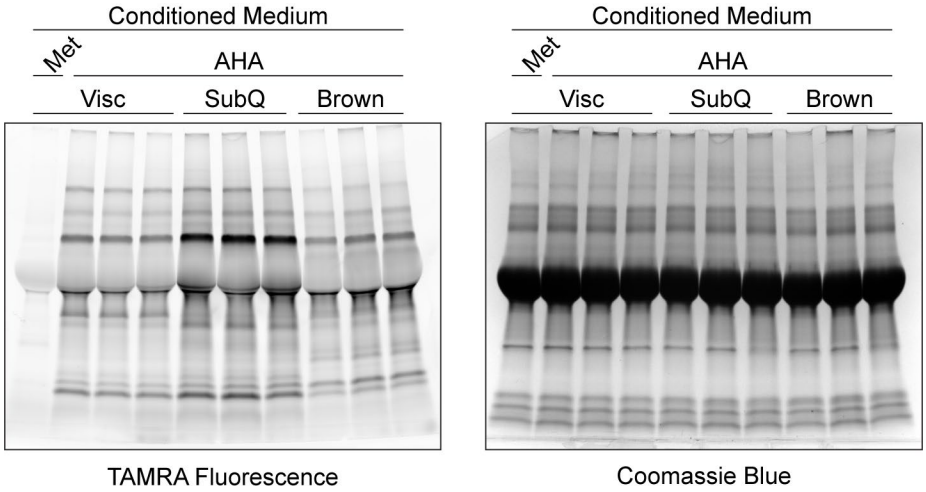

Figure 2.5. In-gel fluorescence analysis of TAMRA-conjugated CM proteins
Equivalent amounts of protein are loaded from FBS-containing media conditioned by Met-pulsed (lane 1) or AHA-pulsed (lanes 2-10) adipocytes. Bands positive for TAMRA fluorescence (left) and Commassie Blue-stained gel as loading control (right).

For identification and quantitative analysis of the secretome across the three adipose cell types, azide-labeled proteins were enriched from CM by conjugating with alkyne agarose beads. On-bead digestion with Lys-C and trypsin was performed, and the resulting peptides were subjected to label-free MS and analyzed using MaxQuant. We detected a total of 742 proteins, of which 138 were excluded as reverse hits or FBS contaminants (**Figure 2.6A**). The intensity-based absolute

quantification (iBAQ) value estimates a protein's molar abundance (Schwanhäusser et al., 2011), and summation of all non-reversed, non-contaminant iBAQ intensities (Σ iBAQ) of a sample can estimate total moles of proteins detected (Shin et al., 2013). Σ iBAQ value calculated for each sample validated enrichment of proteins in AHA-pulsed samples compared to Met-pulsed controls (**Figure 2.6B**). Σ iBAQ intensities across samples closely correlated with in-gel fluorescence (**Figure 2.5**), both of which showed highest abundance of secreted proteins in SubQ CM.

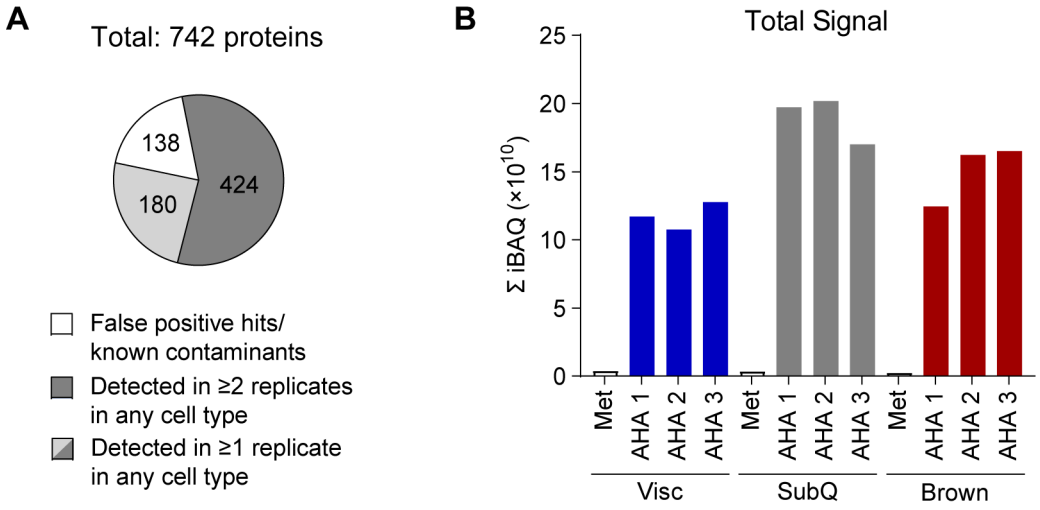

Figure 2.6. Overview of proteins identified and quantified by label-free MS
(**A**) Number and distribution of detected proteins based on exclusion criteria and number of replicates a protein was detected in. (**B**) Sum of iBAQ intensities (Σ iBAQ) across 604 quantified proteins in each CM.

2.2.2 Comparison of detected proteins with annotated or predicted secreted factors

We next used bioinformatic analyses to examine how many of these AHA-labeled proteins detected by MS are reported or predicted secreted factors. Cross-referencing 594 genes from 604 detected proteins with the gene ontology (GO) cellular component database, a large majority of proteins (413/594, 70%) were annotated to be located in the extracellular space (**Figure 2.7A**).
We performed retrospective secretion prediction analysis on primary amino acid sequences of 604 proteins, evaluating the proportion of proteins predicted to be secreted by the classical ER/Golgi pathway (SignalP5.0, TMHMM2.0), subcellular localization (DeepLoc1.0), glycosylphosphatidylinositol (GPI)-anchors (PredGPI), and non-classical routes (SecretomeP2.0) (Almagro Armenteros et al., 2017, 2019; Bendtsen et al., 2004; Krogh et al., 2001; Pierleoni et al., 2008). More than two-thirds of the proteins (413/604, 68%) were predicted to be secreted via the classical pathway, while non-classical secretion constituted about 10% (62/604) (**Figure 2.7B**). Overall, 79% of detected proteins (479/604) met at least one criterion of secretion prediction (**Figure 2.7B**). More than 20% of the identified proteins would not have been predicted to be secreted by these algorithms, highlighting the imperfect nature of *in silico* predictions and the value of directly measuring secreted protein levels.

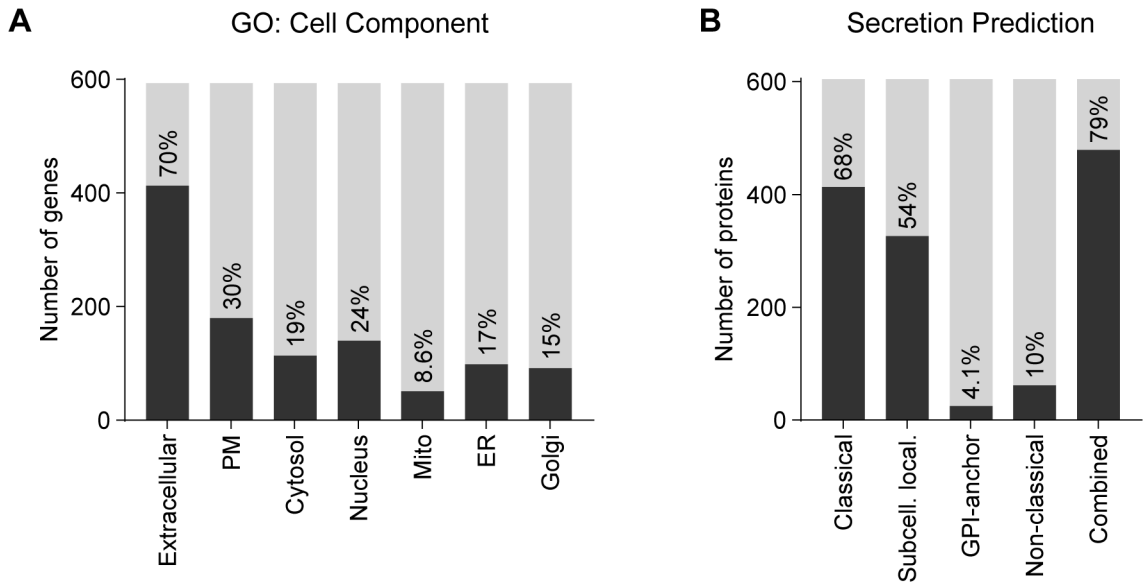

Figure 2.7. Comparison with annotation database or *in silico* secretion prediction
(**A**) Number and proportion of genes annotated to GO cell component terms. Extracellular, extracellular region, space, or matrix; PM, plasma membrane; Mito, mitochondrion; ER, endoplasmic reticulum; Golgi, Golgi apparatus. (**B**) Number and proportion of proteins predicted to be secreted by prediction algorithms.

2.2.3 Differential analysis reveals cell type-specific secretome with functional enrichment

Previous studies have demonstrated distinct secretory profiles across adipose cell types in humans and mice (Deshmukh et al., 2019; Hocking et al., 2010; Khan et al., 2018; Roca-Rivada et al., 2015). Consistent with these studies, plotting correlations of all nine AHA-pulsed samples against each other showed that biological replicates correlate tightly with one another ($R > 0.97$), whereas correlations across different cell types were lower ($0.74 < R < 0.91$) (**Figure 2.8**). Similarly, principal component analysis (PCA) showed that each cell type's secretory profile formed a distinct cluster (**Figure 2.9A**). For further analysis, we focused on the 424 proteins detected in at least 2/3 replicates (**Figure 2.6A**). We found that 255 proteins were detected in all three cell types (**Figure 2.9B**). Interestingly, Brown CM contained the most diverse array of protein species with the greatest number of uniquely detected secreted factors (**Figure 2.9B**). For a more quantitative analysis, we compared their Log2-transformed label-free quantification (LFQ) intensities, imputing any missing values with a left-shifted Gaussian distribution. One-way ANOVA yielded 348 proteins with significantly different ($q < 0.01$) secretory profiles across cell types, and unbiased clustering was performed based on these proteins' levels in CM (**Figure 2.9C**). Clusters 1 and 4 contained proteins enriched in CM of Visc and Brown, respectively. Proteins in cluster 2 were most abundant in CM of SubQ followed by Visc, both white adipocytes. Cluster 3 was highly secreted by SubQ and Brown adipocytes and contained proteins such as SLIT2 (Svensson et al., 2016), suggesting enrichment of beige/brown secretome. Cluster 4 comprised the largest number of proteins (125/348), consistent with the finding that Brown CM contained the greatest number of unique proteins. Ranking proteins by decreasing order of abundance, we found high levels of many well-described adipocyte secreted factors such as CFD, RETN, ADIPOQ, and RBP4 (**Figure 2.9D**). We also noticed that many cluster 2 proteins ranked highly based on abundance, while cluster 4 proteins skewed towards lower abundance (**Figure 2.9D**). Taken together, these results

suggested that while SubQ adipocytes demonstrate high secretory capacity, the brown adipocyte secretome is characterized by a diverse array of proteins, many of which are secreted at lower levels.

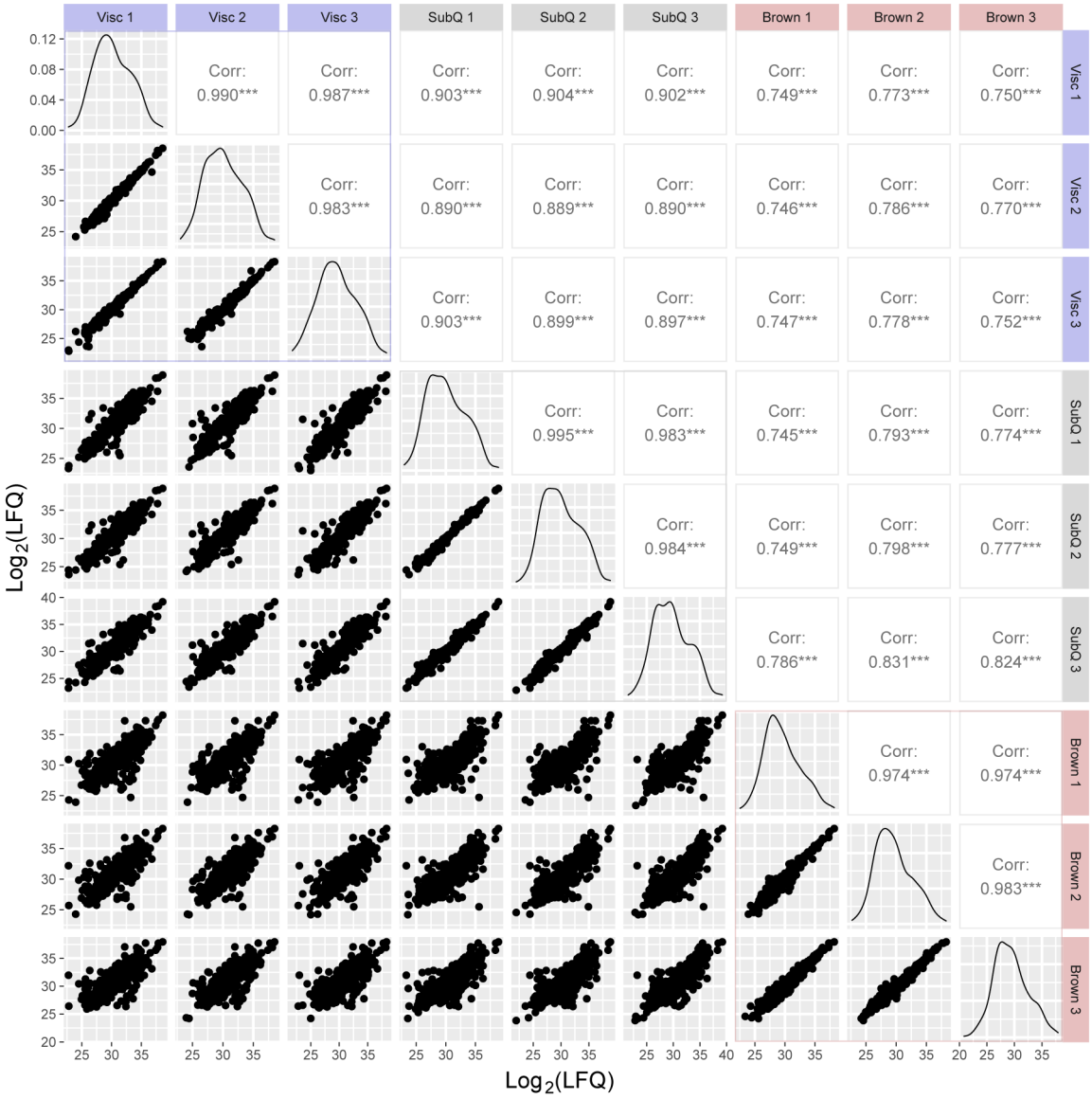

Figure 2.8. Pairwise comparisons of AHA-pulsed samples
Scatterplot Log_2(LFQ) intensities are displayed on the bottom-left, distribution on the diagonal, and Pearson correlation coefficients on the top-right.

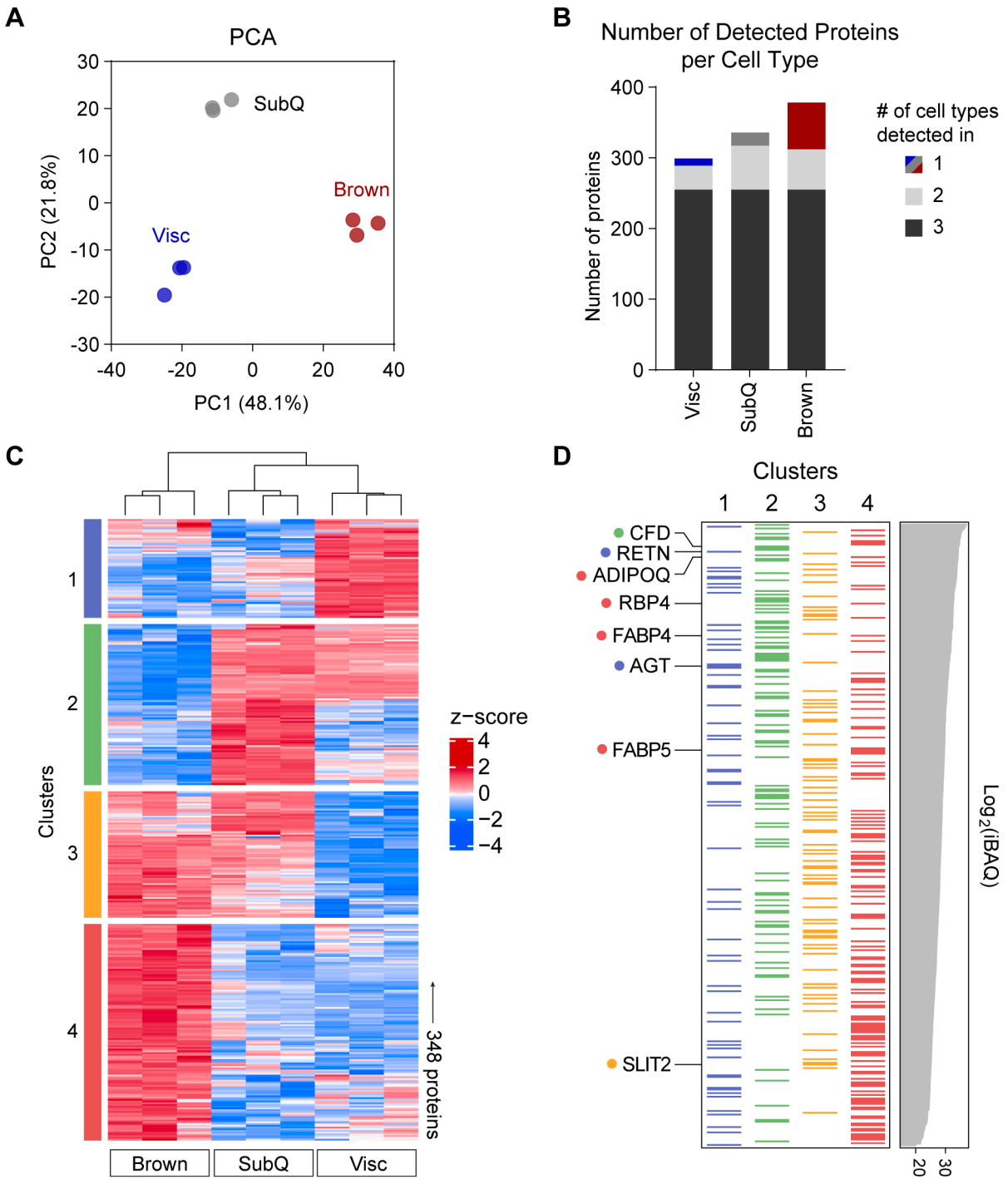

Figure 2.9. Differential analysis of CM proteins from Visc, SubQ, and Brown adipocytes
(**A**) PCA of AHA-pulsed samples. (**B**) Number of proteins detected in at least 2 of 3 replicates per cell type, color-coded based on number of cell types a protein is detected in. (**C**) Heatmap of 348 differentially secreted proteins across cell types. (**D**) 348 proteins grouped in clusters from (C) and arranged in decreasing order of iBAQ intensities. Previously described adipokines are indicated.

To assess whether these distinct clusters demonstrate functional enrichment, we performed pathway analysis using DAVID (**Figure 2.10A**) (Huang et al., 2009a, 2009b). Visc CM-enriched cluster 1 was overrepresented with proteins involved in immune response and complement activation, such as C1QA, C1QB, C1QC, and CFH (**Figure 2.10B**). Proteins with a role in collagen fibril organization and extracellular matrix formation, such as COL1A1, COL3A1, COL5A2, and SFRP were enriched in cluster 2 (**Figure 2.10C**). Cluster 3 (beige/brown enriched) showed overrepresentation of mononuclear cell migration factors and regulators of angiogenesis (**Figure 2.10D**). Finally, Brown CM-specific proteins in cluster 4 were enriched for axon guidance and neuronal differentiation factors such as NRP1, SEMA3C, SLIT3, and NGF, consistent with the importance of innervation for BAT thermogenic function (**Figure 2.10B**) (Wang et al., 2020; Zeng et al., 2019).

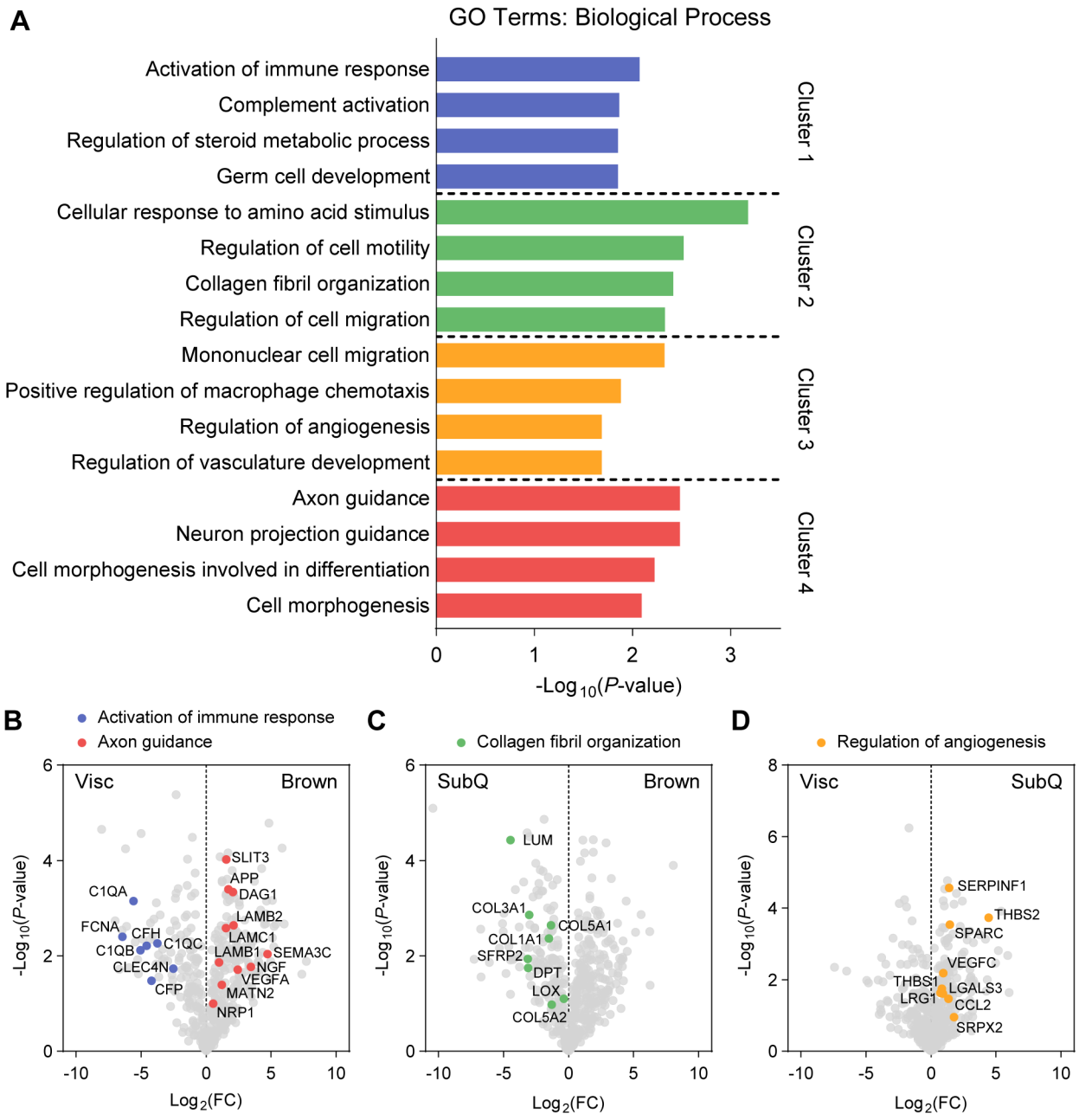

Figure 2.10. Pathway analysis of differentially secreted proteins
(**A**) Top 4 overrepresented GO biological process terms per cluster and their enrichment scores. (**B-D**) Pairwise comparisons of Log_2(LFQ) intensities between Visc and Brown (**B**), SubQ and Brown (**C**), and Visc and SubQ (**D**) CM. Proteins and their annotated pathway terms from (A) are indicated.

2.3 BONCAT profiling of nascent serum proteome *in vivo*

2.3.1 Intraperitoneal AHA injection enables metabolic labeling of serum proteome

To metabolically label serum proteins with AHA *in vivo*, we administered 0.1 g/kg/day of AHA IP to chow-fed 5-week-old male B6 animals for two consecutive days (**Figure 2.11A**). We did not notice any major adverse effects at this dose, and body weights did not differ between PBS- and AHA-injected animals (**Figure 2.11B**).

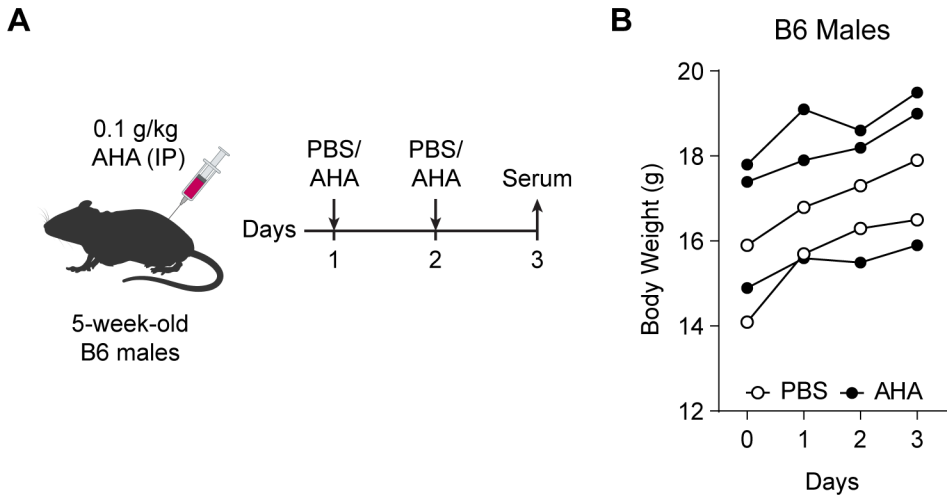

Figure 2.11. Administration of AHA to B6 mice

(**A**) Schematic of AHA IP injections. (**B**) Body weights of mice injected with PBS (n = 2) or AHA (n = 3).

24 hours after the second injection, animals were sacrificed and serum was collected. Similar to CM proteins, we tested if this protocol was sufficient to introduce serum proteins that had incorporated AHA. CuAAC conjugation of serum proteins with TAMRA-alkyne and in-gel fluorescence analysis showed increased signal across most bands in the AHA group along with some AHA group-specific fluorescent bands (**Figure 2.12A**). We used alkyne agarose beads to enrich the azide-labeled nascent proteome and performed MS analysis. Σ iBAQ showed successful enrichment in animals injected with AHA (**Figure 2.12B**). Of note, this experiment was done without dietary Met restriction or depletion of abundant serum proteins, which limited the depth of proteome labeling and identification. However, this approach still enabled detection of 201 proteins (198 proteins in AHA-pulsed samples), including classical adipokines such as ADIPOQ, adipsin (CFD), and RBP4 (**Figure 2.12C**).

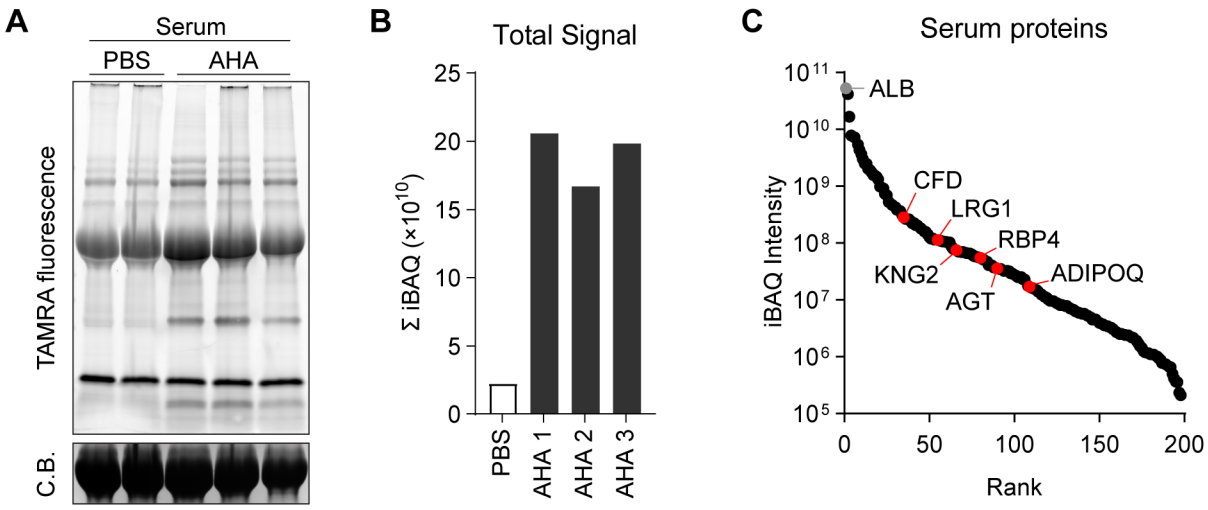

Figure 2.12. Validation of AHA incorporation into serum
(**A**) In-gel fluorescence analysis of TAMRA-conjugated serum proteins from PBS-pulsed (lanes 1 and 2) or AHA-pulsed (lanes 3-5) mice. C.B., Coomassie Blue. (**B**) Sum of iBAQ intensities (Σ iBAQ) across all quantified proteins in each serum. (**C**) iBAQ intensities of detected serum samples arranged in decreasing order.

2.3.2 Bioinformatic tissue origin prediction of serum proteins

Because AHA can be incorporated into the proteome of any tissue, the detected serum proteins originate from multiple tissues. We therefore employed bioinformatic analyses to predict the tissue source of these serum proteins. We cross-referenced 190 genes from 198 detected proteins with a publicly available RNA-Seq dataset from the ENCODE Consortium (Davis et al., 2018; Dunham et al., 2012). We applied a t-distributed stochastic neighbor embedding (t-SNE) algorithm to each protein and its tissue mRNA levels from the ENCODE/LICR dataset and plotted these data on a 2D plane (**Figure 2.13**). Each gene was color coded with respect to its highest expressing tissue. The majority of proteins were most highly expressed by the liver, which comprised the largest cluster (104/190, 55%) and included albumin (*Alb*), apolipoproteins, complements, and serine protease inhibitors (Serpins). BAT, the only adipose tissue whose mRNA levels were profiled in the dataset we analyzed, formed a cluster of 14 genes (7.4%). As expected, classical adipokines known for highly adipose-specific expression such as adiponectin (*Adipoq*) and adipsin (*Cfd*) belonged to this group, along with a recently described batokine, *Kng2* (Peyrou et al., 2020).

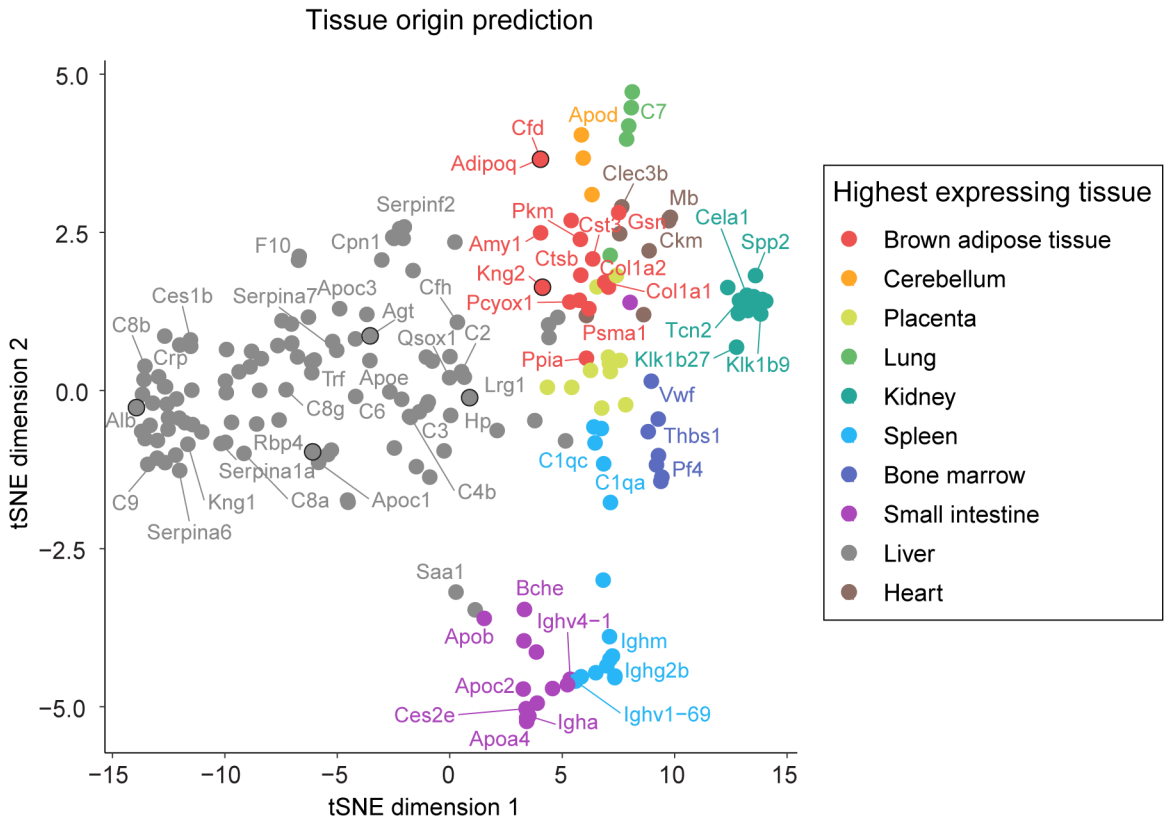

Figure 2.13. Tissue origin prediction of serum proteins
t-SNE clustering of detected serum protein genes based on tissue mRNA expression levels from the ENCODE/LICR dataset

2.3.3 Quantitative analysis of adipose tissue enrichment

BioGPS offers microarray-based transcriptomic data across a much wider variety of mouse tissue and cell types including two adipose tissues, eWAT and BAT (Wu et al., 2009, 2013, 2016). In order to estimate the contribution of adipose tissue expression to the detected serum proteins, we numerically scaled the degree of adipose tissue enrichment for each of the detected serum proteins using the BioGPS dataset. Adipose enrichment for each gene was defined as the number of tissues with expression levels significantly lower than that of eWAT, BAT, or combined. We divided this value by the total number of pairwise comparisons (i.e., total number of tissues - 2 adipose tissues) to obtain the percentage adipose tissue enrichment score. Among the top-enriched genes were many well-described adipokines such as *Adipoq*, where 76 of 86 tissues (88.4%) expressed *Adipoq* at significantly lower levels than eWAT and BAT combined (**Figure 2.14**). We also identified genes yet to be described as adipokines, such as *Lrg1* and *Amy1* (**Figure 2.14**). Many genes, such as *Rbp4*, *Agt*, and *Lrg1*, showed high expression in adipose tissues as well as the liver. On the t-SNE plot, these genes were grouped with other liver-specific genes, but located closer to the adipose tissue cluster (**Figure 2.13**). Still, their percentage adipose tissue enrichment scores were all >80%, as few other tissues express those genes.

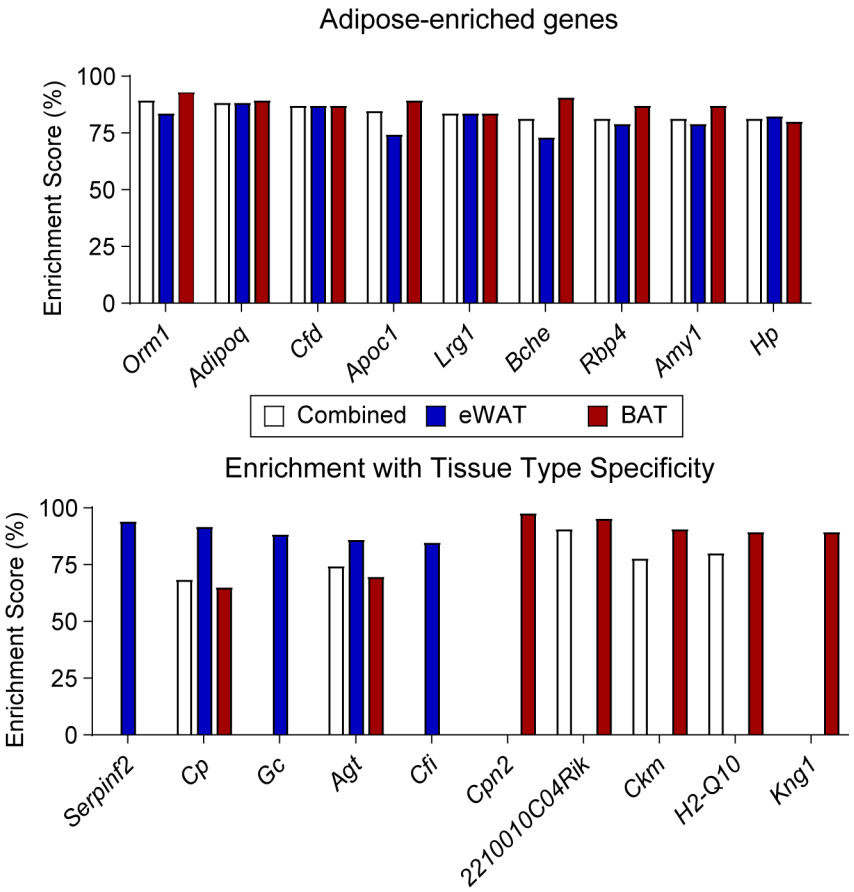

Figure 2.14. Tissue enrichment analysis of serum proteins
Adipose tissue-enriched serum protein genes and % enrichment scores calculated from Bio-GPS dataset.

2.4 Discussion

We applied a chemoproteomic technology to comprehensively profile the secretome of three major types of murine primary adipocytes, revealing unique secretory profiles of each cell type with differential functional enrichment. This method can also be applied *in vivo* to profile the nascent serum proteome, and bioinformatic analysis demonstrated that adipose tissue is an important contributor to the serum proteome.

More than 70% of proteins in our adipocyte CM dataset were annotated to be localized in the extracellular space or predicted to be secreted. The low rate of intracellular protein detection demonstrates the advantage BONCAT provides by enabling FBS supplementation. While the remaining 20% of proteins not predicted or annotated to be secreted include leakage of abundant intracellular proteins such as tubulins and actins, many are non-classically secreted proteins such as GAPDH (Takenouchi et al., 2015), FABP4/5 (Cao et al., 2013; Hotamisligil and Bernlohr, 2015). With careful validation, our dataset can greatly expand the scope of the adipose secretome to encompass classical and non-classical modes of secretion. We have also demonstrated that BONCAT can label nascent serum proteins *in vivo* via relatively facile AHA IP injections under normal feeding conditions. With additional fractionation/depletion steps commonly utilized in serum proteome analyses, this technique can be further utilized to study the nascent serum

proteome in response to stimuli that are difficult to model *in vitro*, such as obesity, fasting/feeding, and changes in ambient temperature. Novel technologies for *in vivo* profiling of cell type-specific proteomes using non-canonical amino acids (Alvarez-Castelao et al., 2017; Krogager et al., 2018) or proximity labeling (Branon et al., 2018; Wei et al., 2021) are on the horizon. This study provides a baseline profile of the nascent serum proteome from which cell type enrichment analyses can be performed, and bioinformatic pipelines implemented to predict tissue origin would be useful in cross-referencing with transcriptomic datasets.

Quantitative analysis of the secretome across adipocytes demonstrated that more than half of the detected proteins were differentially secreted across cell types. In addition to well-known factors such as RETN and AGT, Visc CM proteins were characterized by relative abundance of factors involved in activation of immune processes and complements. SubQ CM demonstrated abundant secretion of extracellular matrix proteins, including various types of collagens. Finally, it is interesting to note that brown adipocyte CM contained the most diverse array of proteins at relatively low abundance, including paracrine mediators known to affect axon guidance or neurite outgrowth. Such factors may play an important role in regulating innervation necessary for thermogenic fat function (Chi et al., 2018, 2021; Wang et al., 2020; Zeng et al., 2019).

CHAPTER 3. C11orf54 is a non-canonically secreted beige/brown-enriched factor

3.1 Introduction

Although BAT activation is associated with a range of cardiometabolic benefits (Becher et al., 2021), it is increasingly appreciated that UCP1-dependent energy dissipation is only one mechanism among a wide variety of thermogenic brown/beige adipocyte functions that promote metabolic health. In fact, a transgenic mouse line with increased beige fat but with genetic deletion of *Ucp1* retain most of the metabolic benefits of having greater beige fat mass, suggesting that UCP1 is dispensable for physiological effects of beige fat. Among these functions of thermogenic adipocytes include their ability to secrete specific set of bioactive polypeptides, collectively referred to batokines (Cohen and Kajimura, 2021; Villarroya et al., 2017).

Our proteomic profiling experiments from Chapter 2 validated that brown adipocytes secrete a distinct set of proteins that formed a cluster with functional enrichment. With these data, we sought to identify a novel factor whose secretion level is enriched in brown fat. To this end, we cross-referenced 66 proteins uniquely identified in Brown CM (**Figure 2.9B**) with transcriptomic datasets to search for factors whose expression is enriched in brown adipocytes at both protein and mRNA levels. From this search strategy, we identified an uncharacterized protein-coding ORF with gene symbol *4931406C07Rik*, also called ester hydrolase homolog of C11orf54, as a putative batokine.

3.2 *C11orf54* is a beige/brown-enriched gene

We first sought to measure *C11orf54* gene expression levels by qPCR to validate the search strategy. C11orf54, encoded by *4931406C07Rik*, has four transcript variants that code for two protein isoforms. We defined the longer protein (315 amino acids long) encoded by three transcript variants as isoform 1 and the shorter peptide (282 amino acids long) isoform 2 (**Figure 3.1**).

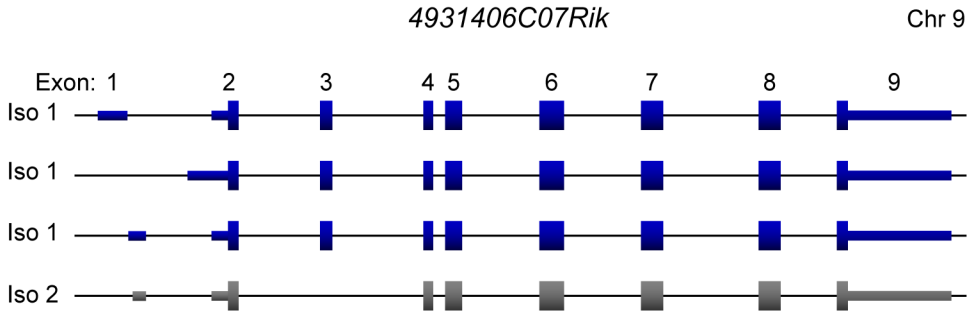

Figure 3.1. Exon structure of *4931406C07Rik* that encodes C11orf54

Protein coding regions depicted as wide bands, untranslated regions (UTRs) as narrow bands. Top three transcript variants (in dark blue) code for C11orf54 protein isoform 1, bottom transcript variant (in gray) lacks exon 3 and codes for isoform 2.

We designed qPCR primer pairs specifically targeting each of the two protein isoforms, and performed qPCR to measure *C11orf54* expression levels in eWAT, iWAT, and BAT harvested from 8-week-old B6 male mice housed at room temperature (**Figure 3.2**). Consistent with the MS dataset that detected C11orf54 protein only in Brown CM, expression of *C11orf54* was highest in BAT, with both isoforms demonstrating virtually identical expression patterns. Many BAT-

enriched genes are induced in iWAT in response to beige fat-activating stimuli, such as cold exposure. To examine if *C11orf54* expression is also enriched in beige fat, we housed the mice at 6ºC for one week and harvested the tissues. qPCR analysis demonstrated highly significant induction of *C11orf54* in iWAT, indicating that *C11orf54* is a brown/beige-enriched gene (**Figure 3.2**).

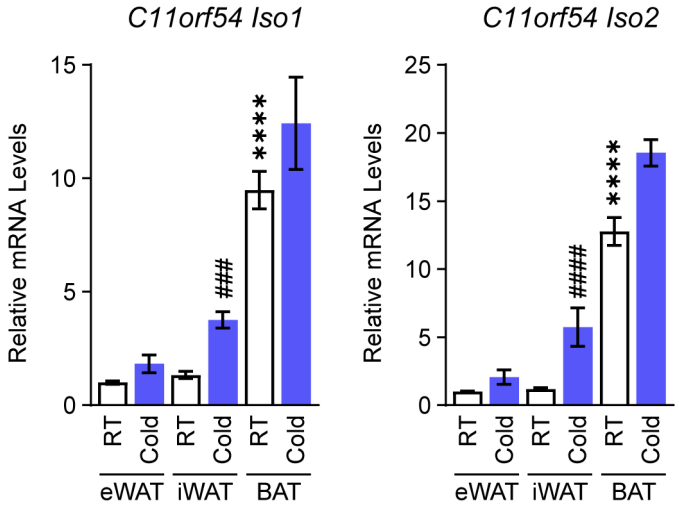

Figure 3.2. *C11orf54* is a brown/beige-enriched gene
Relative mRNA levels of *C11orf54* isoforms 1 and 2 in eWAT, iWAT, and BAT from 8-week-old B6 male mice housed at RT or 6ºC (cold) for 7 days. Data are presented as mean ± SEM. Tukey post hoc test results from two-way ANOVA are indicated. ****$P < 0.0001$, RT-BAT vs. RT-eWAT. ###$P < 0.001$, ####$P < 0.0001$, Cold-iWAT vs. RT-iWAT. $n = 5$ per group.

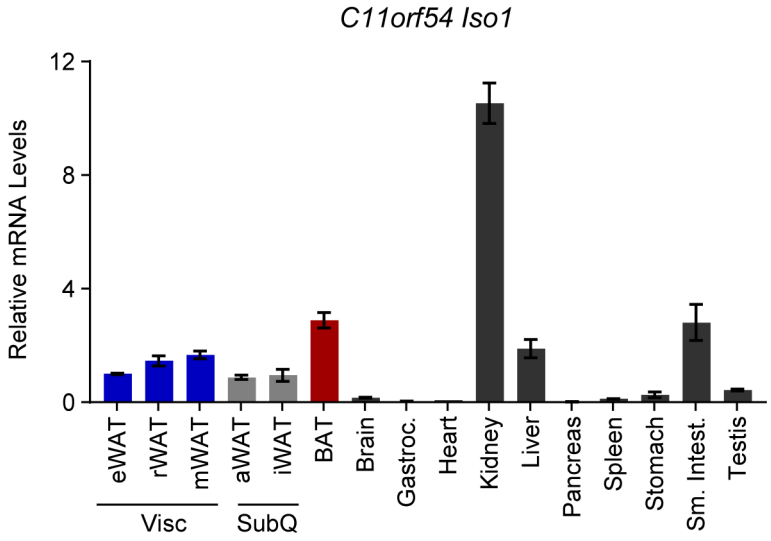

Figure 3.3. *C11orf54* expression in various tissues
Relative *C11orf54 Iso1* mRNA levels across a panel of tissues from 8-week-old male B6 mice. Visc, visceral fat depots; SubQ, subcutaneous fat depots. $n = 5$ per group.

We also measured expression of *C11orf54* across a panel of tissues harvested from 8-week-old B6 males. Interestingly, *C11orf54* was most highly expressed by the kidney, followed by small intestine and BAT (**Figure 3.3**). Again, we observed that the expression pattern for the two protein isoforms was virtually identical. Taken together, these data demonstrated that *C11orf54* is a brown/beige adipocyte-enriched gene, but its expression was also observed in other tissues, mainly kidney and small intestine.

3.3 C11orf54 is secreted via a non-classical pathway

Retrospective secretion prediction analysis performed in Chapter 2 showed that C11orf54 belonged to the 21% of proteins that are not predicted to be secreted by any of the prediction algorithms (**Figure 2.7B**). In addition, there was no difference in prediction results between the two protein isoforms. For instance, SignalP5.0 yielded a secretion likelihood score of 0.0014 for isoform 1 and 0.0011 for isoform 2, in stark contrast to well-characterized secreted factors such as adiponectin (ADIPOQ) which scored 0.9995. These data suggest that C11orf54 is unlikely to be secreted by the classical ER/Golgi pathway.

We set out to validate if C11orf54 is a *bona fide* secreted factor in a cell culture system (**Figure 3.4**). We transfected HEK293A cells with plasmids encoding C-terminally FLAG-tagged C11orf54 isoform 1 (C11orf54Iso1-FL) or 2 (C11orf54Iso2-FL). We subsequently labeled their nascent proteome by pulsing the cells with AHA and collected the CM at various timepoints. Conjugation of CM proteins with TAMRA allowed visualization total nascent protein secreted by cells, while subsequent transfer to a membrane for α-FLAG immunoblot allowed specific detection of C11orf54 protein.

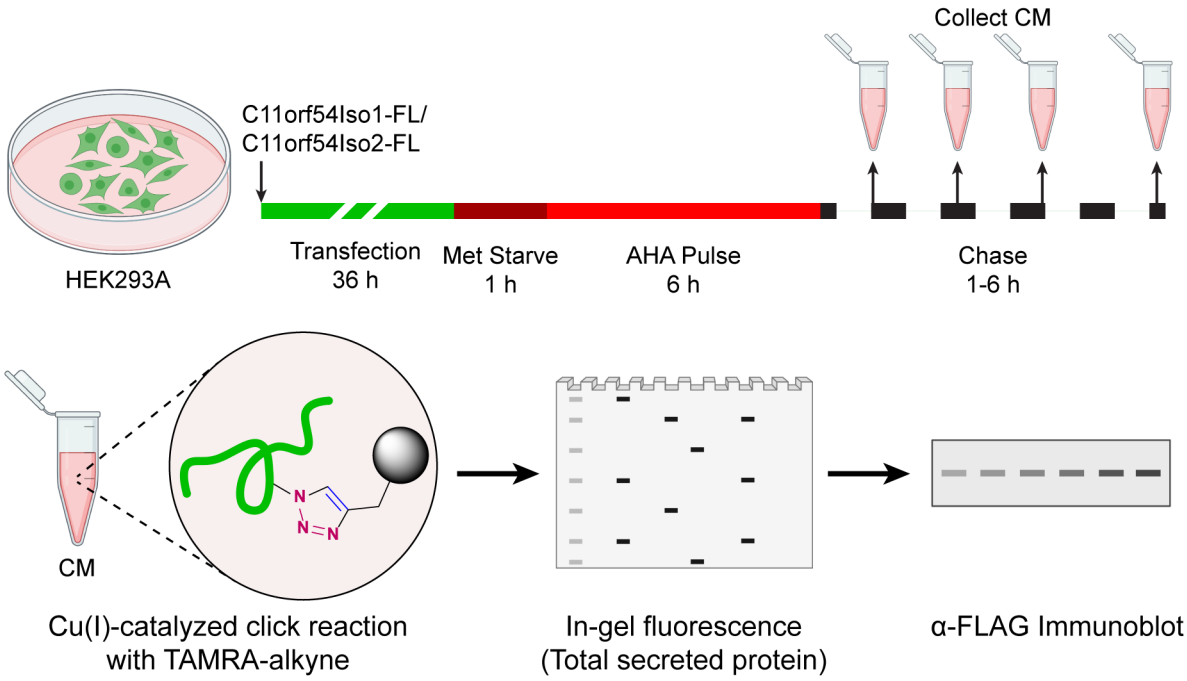

Figure 3.4. Experimental scheme for validation of C11orf54 secretion

Interestingly, while we detected incremental FLAG signal in CM of cells transfected with C11orf54Iso1-FL between 1 and 6 hours, CM of C11orf54Iso2-FL-transfected cells did not show nearly as much signal despite having comparable TAMRA signals (**Figure 3.5**). These results indicate that C11orf54 isoform 1 is secretory while isoform 2 is not.

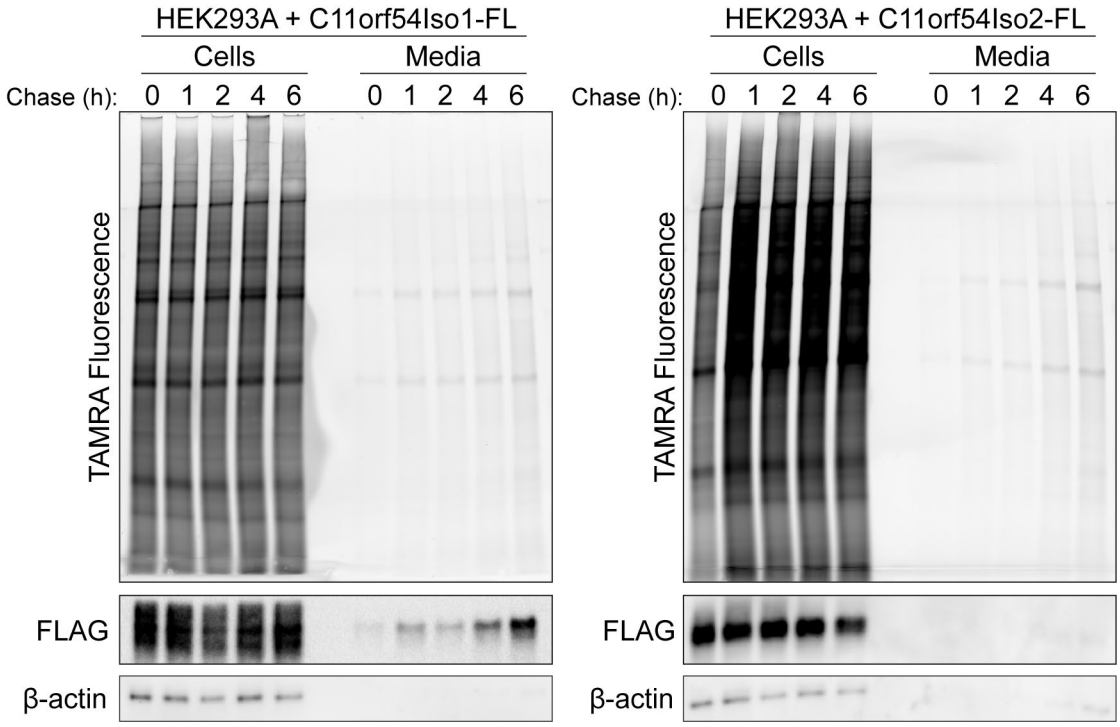

Figure 3.5. *In vitro* study demonstrates C11orf54 isoform 1 is secreted
In-gel fluorescence and immunoblot against FLAG and β-actin from cell lysate and CM of HEK293A transfected with C-terminally FLAG-tagged C11orf54 isoform 1 or 2.

We next tested with *in vivo* models to confirm whether C11orf54 isoform 1 can be detected in mouse circulation. We transduced 8-week-old B6 males with adenovirus encoding C11orf54Iso1-FL (Ad-C11orf54Iso1-FL) or eGFP control (Ad-eGFP) and harvested their blood 5 days after injection. In Ad-eGFP transduced mice, we observed basal levels of C11orf54 protein, which increased in Ad-C11orf54Iso1-FL transduction (**Figure 3.6**). Interestingly, we were no longer able to detect the FLAG epitope even in the overexpression group, suggesting that the protein is cleaved near the C-terminus once it reaches circulation. These data definitively demonstrated that C11orf54Iso1 is a *bona fide* secreted protein.

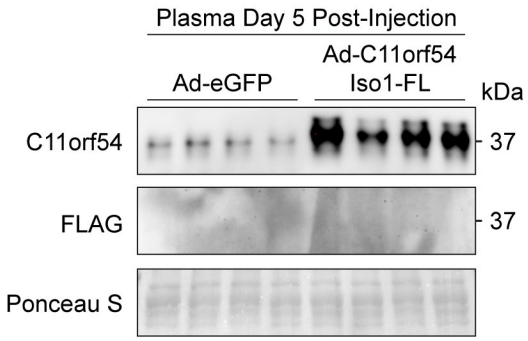

Figure 3.6. *In vivo* validation of C11orf54 secretion
Plasma western blot of C11orf54 5 days after Ad injection.

Confirming the secretion of C11orf54 despite its lack of a signal peptide, we sought to directly observe if C11orf54 protein is localized in the ER/Golgi pathway. To this end, we fixed primary SubQ adipocytes and performed immunofluorescence against native C11orf54 and KDEL, a marker of ER proteins. Observing their subcellular localization via deconvolution microscopy, we found that C11orf54 is localized to both nucleus and cytosol, without any co-localization with KDEL (**Figure 3.7**). Taken together, these results suggest that C11orf54Iso1 is secreted via a non-classical pathway.

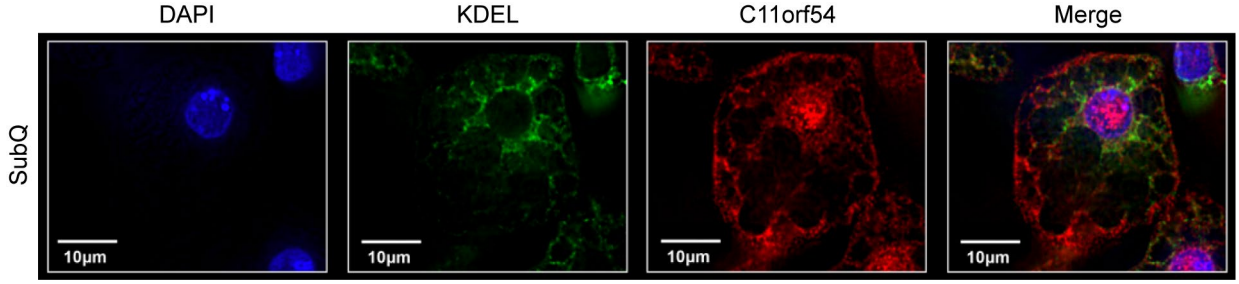

Figure 3.7. C11orf54 does not co-localize with an ER marker
Deconvolution microscope images of primary SubQ adipocytes stained with DAPI (nucleus), α-KDEL antibody (ER), and α-C11orf54 antibody. Scale bars are indicated.

3.4 Functional studies on C11orf54

To explore the effect of C11orf54 loss of function on whole-body metabolism, we generated a KO mouse line in B6 background using CRISPR/Cas9. To be able to differentiate the physiological effects of the secreted form (Iso 1) versus the non-secreted form (Iso 2), we first generated C11orf54Iso1-KO mice using a gRNA that targets exon 3 (**Figure 3.8**). Serum western blot confirmed the absence of C11orf54 protein, also validating that genetic deletion of isoform 1 is sufficient to ablate circulating protein levels (**Figure 3.9**).

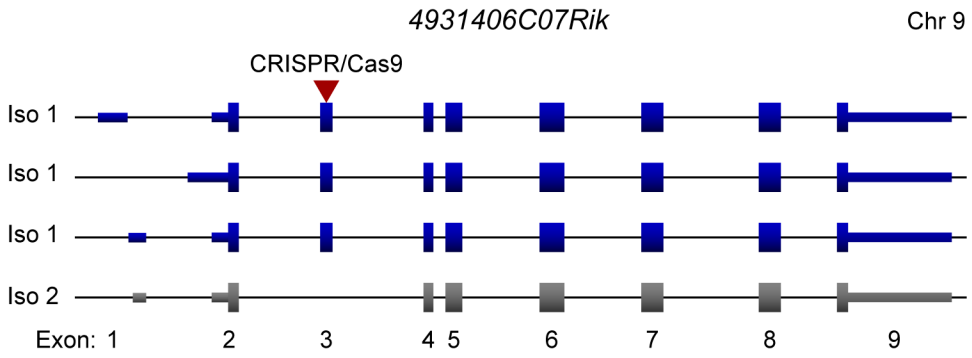

Figure 3.8. Generation of C11orf54Iso1-KO mice using CRISPR/Cas9
Schematic diagram of murine *C11orf54* exon structure. Red arrowhead indicates the region targeted by CRISPR/Cas9 gRNA.

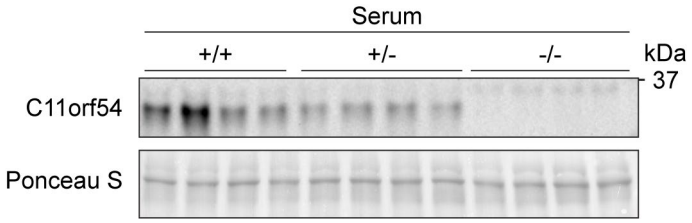

Figure 3.9. Knocking out C11orf54 isoform 1 ablates circulating protein levels
Western blot of C11orf54 in serum of WT (+/+), C11orf54Iso1-heterozygote (+/-), and C11orf54Iso1-KO mice (-/-).

To test whether deletion of C11orf54 alters systemic metabolism, we placed a cohort of C11orf54Iso1-KO mice and their heterozygote and WT littermates in an indirect calorimetry system. Interestingly, we observed that C11orf54Iso1-KO mice had significantly higher oxygen consumption rate compared to their littermate controls ($P = 0.038$). (**Figure 3.10**). While this result needs further validation with larger *n* number, these data suggest that C11orf54 may regulate whole-body energy homeostasis.

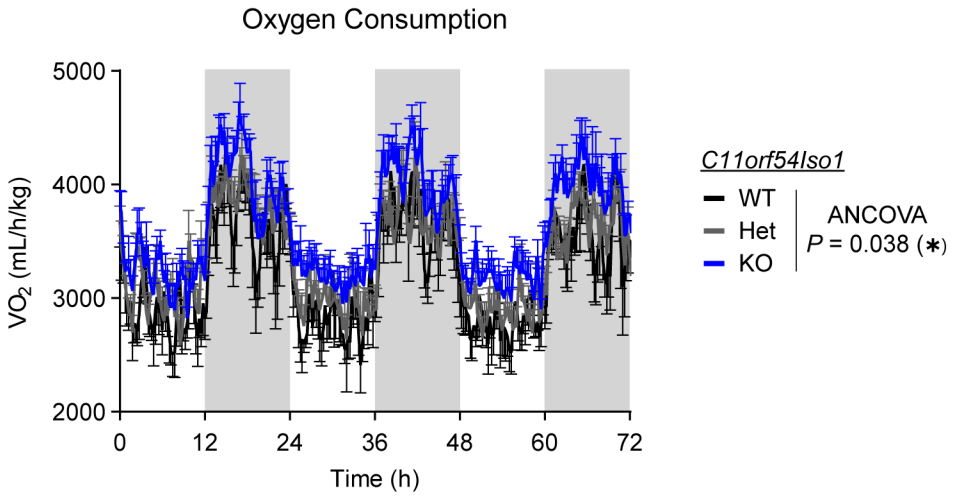

Figure 3.10. Oxygen consumption rates of C11orf54Iso1-KO and littermate controls
Shaded regions indicate 12 h dark cycle. Data are presented as mean ± SEM. ANCOVA *P* indicates group factor *P*-value. **P* < 0.05. *n* = 4-6 per group.

3.5 Discussion and future directions

Increasing evidence suggests that distinct secretory profiles of different adipose cell types mediate the divergent metabolic effects associated with fat distribution or BAT activation. In particular, brown fat-enriched secreted factors, referred to as batokines, likely contribute to the wide array of metabolic benefits associated with BAT activation. Here, we set out to identify a novel secreted factor whose expression is enriched in brown adipocytes. As its name suggests, C11orf54, encoded by *4931406C07Rik*, is a protein of almost completely unknown function. We validated at the gene expression level that *C11orf54* is indeed enriched in brown and beige fat, where its expression was also induced by cold exposure. Neither of the two protein isoforms contains a signal peptide or is predicted to be secreted, but we have validated using both *in vitro* and *in vivo* models that C11orf54 is a *bona fide* secreted protein. Interestingly, we observed that only isoform 1 is secreted, whereas isoform 2 that lacks an internal stretch of 33 amino acids near the N-terminus is retained in the intracellular space. Future work will address how this portion regulates subcellular localization of the protein, and elucidating this mechanism will shed light on mechanisms underlying non-classical secretion.

Preliminary studies demonstrated that mice with whole-body deletion of C11orf54Iso1 have increased oxygen consumption rates. Further characterization studies will be performed whether this phenotype in turn confers other metabolic phenotypes such as resistance to obesity, improved glucose homeostasis, and cold tolerance. We have also generated a mouse line with a full deletion of both isoforms of C11orf54 (**Figure 3.11**). Comparing and contrasting the phenotypes between Iso1-specific KO and full KO will allow us to tease apart the extracellular versus intracellular functions of C11orf54.

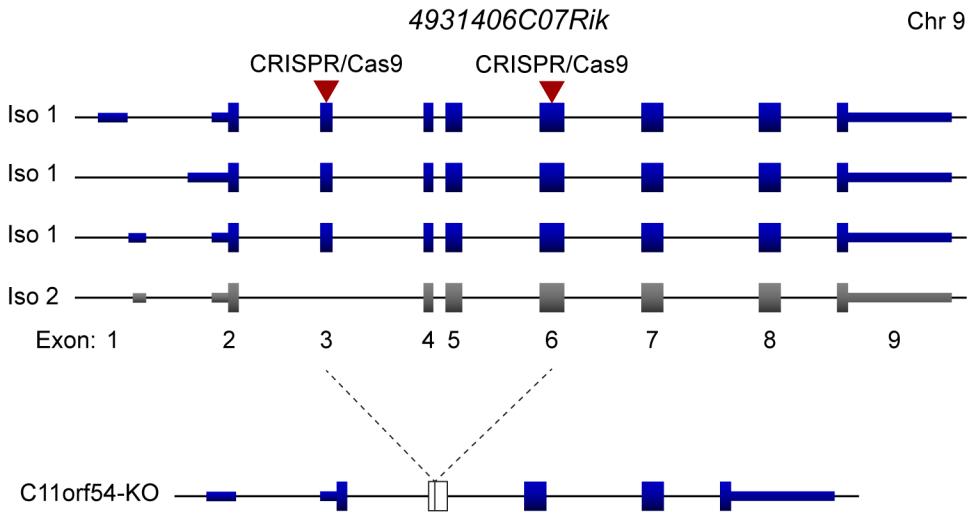

Figure 3.11. Generation of C11orf54-KO mice using CRISPR/Cas9
Schematic diagram of murine *C11orf54* exon structure. Red arrowheads indicate two regions targeted by CRISPR/Cas9 gRNAs. A founder mouse with a germline deletion of the region between exons 3 and 6 as well as a frameshift at the ligation site was identified to generate a mouse line with full deletion of all isoforms of C11orf54.

Further work is also needed to elucidate the molecular basis of C11orf54 function. The crystal structure of human C11orf54 has been solved, which showed that it is a Zinc-binding protein (Manjasetty et al., 2006). A screen for enzymatic activity suggested that C11orf54 is an esterase, capable of catalyzing hydrolysis of 4-nitrophenyl acetate (Manjasetty et al., 2006). It is therefore possible that C11orf54 is a circulating enzyme whose effect is mediated by downstream products. Elucidating the substrates or products of this putative circulating enzyme has the potential of identifying novel pathways that regulate whole-body metabolism.

CHAPTER 4. Leucine-rich α-2 glycoprotein 1 (LRG1) promotes insulin sensitivity and suppresses inflammation

4.1 Introduction

Our next strategy to identify uncharacterized adipokines for further functional analysis focused on discovering potential systemic regulators of metabolism. To this end, we prioritized factors that are 1) detected in adipocyte CM, 2) present in the nascent serum proteome of mice, and 3) enriched in expression in adipose tissues (**Figure 4.1**). We reasoned that such proteins are likely to be adipokines that circulate at meaningful levels and may play a role in regulating whole-body energy homeostasis. Of the 604 proteins detected in CM and the 198 proteins in serum, we selected proteins detected in both datasets and with percentage enrichment scores higher than 80%. This analysis yielded 10 proteins: ADIPOQ, CFD, LRG1, BCHE, RBP4, AMY1, HP, H2-Q10, CP, and AGT. Proteins such as ADIPOQ, CFD, BCHE, and RBP4 have already been identified as adipokines, validating our search strategy. On the other hand, salivary amylase (AMY1), haptoglobin (HP), ceruloplasmin (CP), and angiotensinogen (AGT) have well-characterized biological functions. Therefore, we focused on LRG1, a protein with relatively unknown metabolic function.

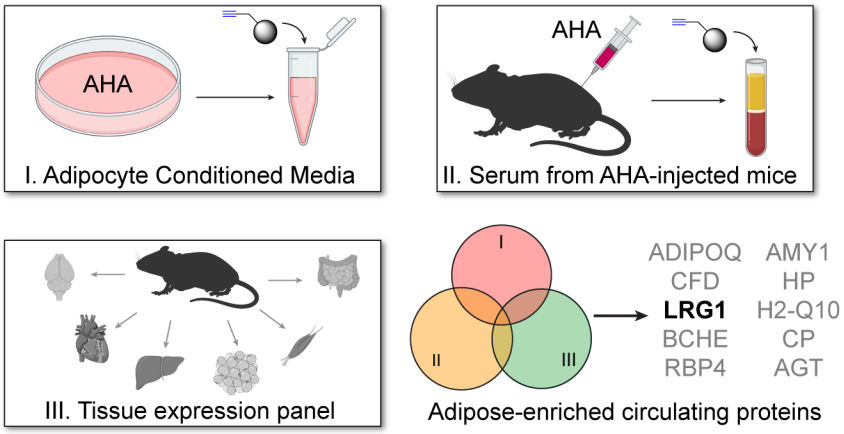

Figure 4.1. Search strategy for identification of novel adipokines with a potential role in whole-body metabolism.

LRG1, or leucine-rich α-2 glycoprotein 1, has been shown to be secreted from skeletal muscle (Boström et al. 2012) and endothelial cells, where it promotes angiogenesis by modulating TGF-β signaling (Wang et al. 2013). In 3T3-L1 adipocytes, *Lrg1* expression correlates with adipogenesis (Birsoy et al., 2011). In BAT, *Lrg1* expression is dependent on an EHMT1-driven brown adipocyte differentiation program (Ohno et al., 2013). Despite these data at the gene expression level, LRG1 has not yet been characterized as an adipokine, and its role in whole-body metabolism has not been studied.

4.2 LRG1 is secreted by mature adipocytes

We first set out to validate the search strategy. Consistent with our tissue enrichment analysis, qPCR from 8-week-old male B6 mice showed that *Lrg1* mRNA was mostly expressed in adipose tissues and liver (**Figure 4.2A**). In addition to mature adipocytes, adipose tissue contains a heterogeneous mixture of various cell types. To determine which cell type(s) within adipose tissue express *Lrg1*, we fractionated eWAT, iWAT, and BAT with collagenase to separate floating

mature adipocytes from the stromal vascular fraction (SVF). *Adipoq*, a specific marker of mature adipocytes, was significantly co-enriched with *Lrg1* in the adipocyte fraction relative to the SVF in all three depots (**Figure 4.2B**).

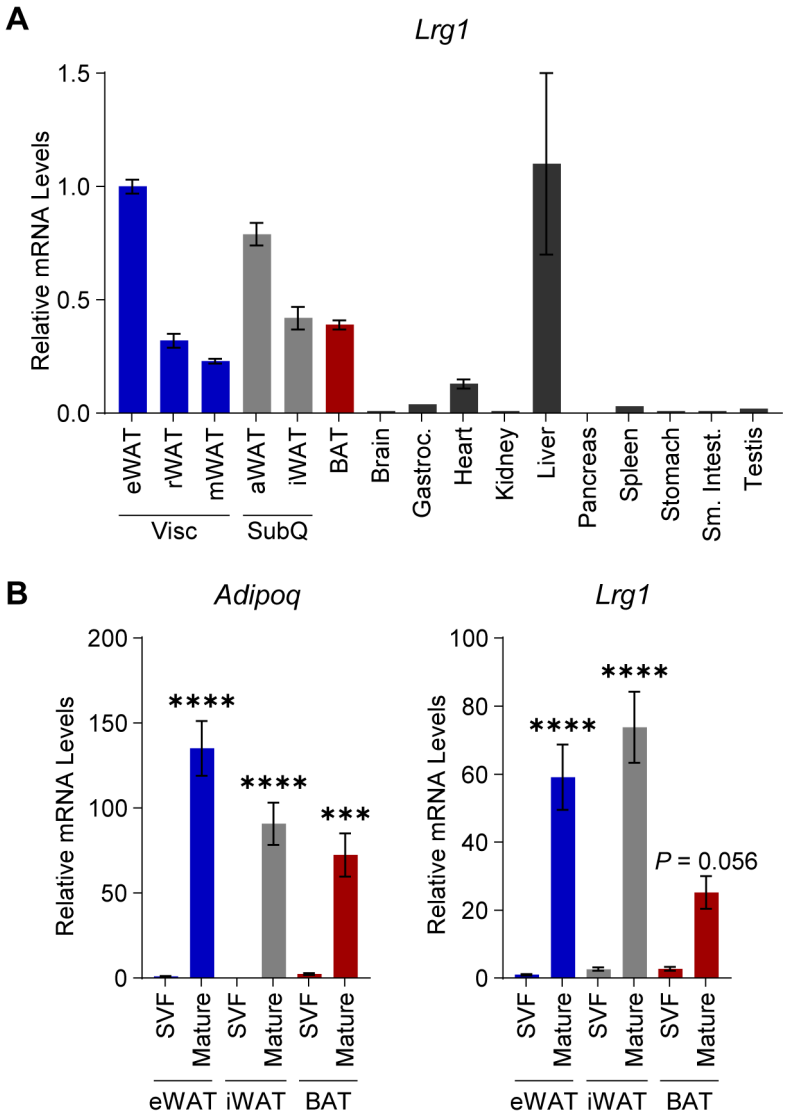

Figure 4.2. *Lrg1* is expressed by mature adipocytes across fat depots
(**A**) Relative *Lrg1* mRNA levels across a panel of tissues from 8-week-old male B6 mice. Visc, visceral fat depots; SubQ, subcutaneous fat depots. $n = 5$ per group. (**B**) Relative *Adipoq* and *Lrg1* mRNA levels of indicated tissues fractionated into mature adipocytes and SVF. Data are presented as mean ± SEM. ***$P < 0.001$, ****$P < 0.0001$ vs. SVF, from Šídák post hoc test following two-way ANOVA. $n = 4$ per group. Data are presented as mean ± SEM.

We also cultured primary Visc, SubQ, and Brown adipocytes and observed how *Lrg1* expression levels change during adipogenic differentiation. We found that *Lrg1* mRNA is induced over 70-fold in all three cell types during *in vitro* adipogenesis (**Figure 4.3A**). Consistent with mRNA data, we found robust levels of LRG1 protein in CM of mature adipocytes, whereas preadipocytes did

not secrete detectable LRG1 (**Figure 4.3B**). While *Lrg1* mRNA levels *in vivo* are higher in WAT than in BAT (**Figure 4.2A**), *in vitro* primary brown adipocytes tend to secrete higher levels of LRG1 protein than primary SubQ or Visc (**Figure 4.3B**), possibly due to more efficient differentiation of primary brown adipocytes typically observed in culture.

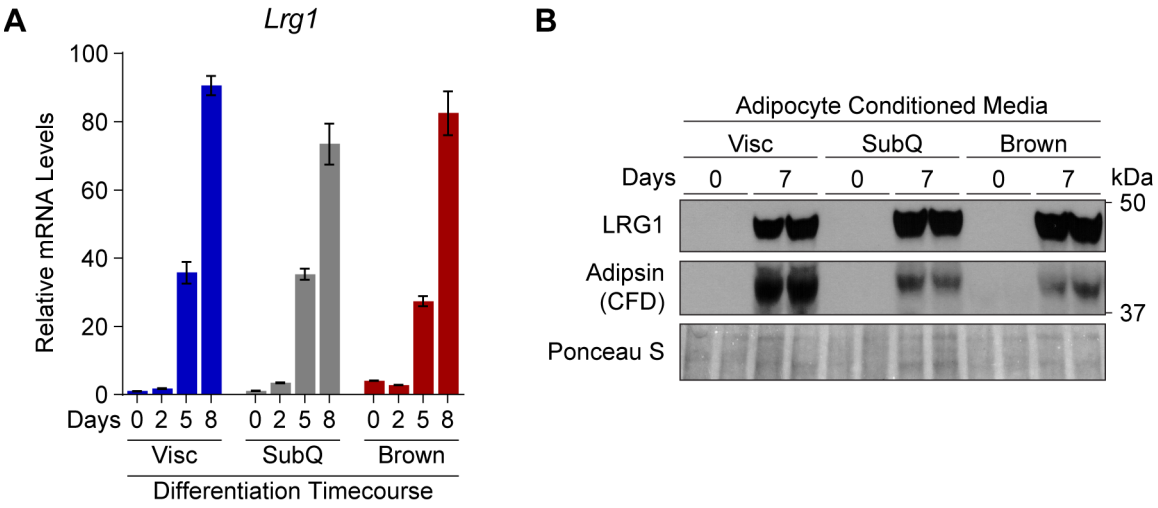

Figure 4.3. *Lrg1* expression in primary adipocytes
(**A**) Relative *Lrg1* mRNA levels during 8 days of *in vitro* differentiation of primary SVF into adipocytes. (**B**) Western blot of LRG1 protein in the CM before (day 0) after (day 7) *in vitro* adipogenic differentiation. Levels of adipsin (CFD), a mature- and Visc fat-enriched protein, shown as a positive control. Ponceau S shown as loading control. Data are presented as mean ± SEM.

4.3 LRG1 is regulated by obesity

To assess whether adipose tissues are a significant contributor to serum LRG1 levels, we collected serum from chow-fed lean B6 mice or diet-induced obese (DIO) mice on high fat diet (HFD) for 4 (10 weeks old) or 9 weeks (15 weeks old). Western blot analysis showed that serum LRG1 levels increased with age and obesity (**Figure 4.4A**). qPCR of major *Lrg1*-expressing tissues, namely eWAT, iWAT, BAT, and liver, showed significant induction of *Lrg1* mRNA in iWAT of DIO mice, but not in liver (**Figure 4.4B**). With the expansion of iWAT in obesity, this induction likely contributes to elevated serum LRG1 levels in this state.

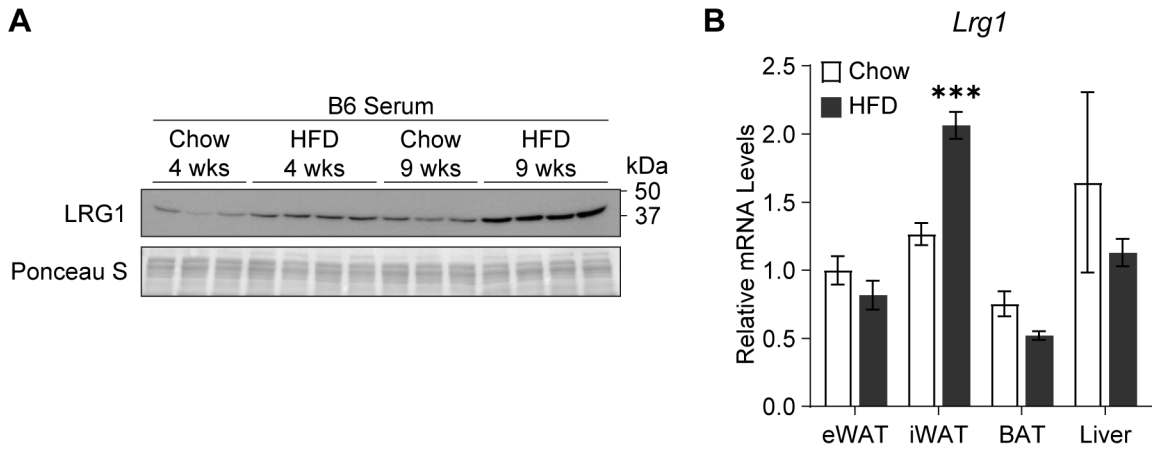

Figure 4.4. Circulating LRG1 levels are increased in obesity
(**A**) Serum western blot of LRG1 from B6 mice on standard chow or HFD for indicated weeks. HFD was started at 6 weeks of age. Ponceau S shown as loading control. (**B**) Relative *Lrg1* mRNA levels of indicated tissues from mice on standard chow or HFD for 15 weeks. HFD was started at 6 weeks of age. Data are presented as mean ± SEM. ***$P < 0.001$ from Welch's *t*-test. $n = 6$ per group.

Obesity is characterized by chronic low-grade inflammation, with elevated circulating inflammatory cytokines (Lackey and Olefsky, 2016). Previous studies using HepG2 cells have shown that *Lrg1* is induced by various pro-inflammatory cytokines (Shirai et al., 2009). We observed that treatment of primary SubQ adipocytes with recombinant human TNFα induced *Lrg1* expression at the level of both mRNA (**Figure 4.5A**) and protein in CM (**Figure 4.5B**). Taken together, these results demonstrate that LRG1 is an obesity-induced adipokine.

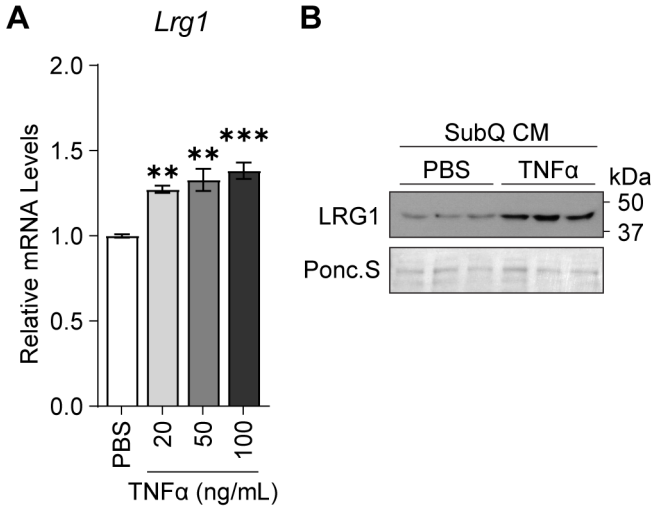

Figure 4.5. LRG1 expression is induced by TNFα
(**A**) Relative *Lrg1* mRNA levels of primary SubQ adipocytes treated with recombinant TNFα and 850 nM insulin for 6 h. Data are presented as mean ± SEM. **$P < 0.01$, ***$P < 0.001$ vs. PBS from Dunnett post hoc test following one-way ANOVA. $n = 3$ per group. (**B**) Western blot of LRG1 in CM of primary SubQ adipocytes treated with PBS or 100 ng/mL recombinant TNFα without insulin for 24 h. Ponceau S shown as loading control.

4.4 LRG1 overexpression improves glucose homeostasis in diet-induced obesity

The above characterization studies demonstrated that *Lrg1* expression in adipose tissue is regulated by obesity. To assess whether LRG1 as an adipokine affects whole-body energy homeostasis in that setting, we used viral vectors to overexpress LRG1 *in vivo* in a DIO model. We first explored the effect of acute adenovirus-mediated LRG1 overexpression in obese mice. Adenovirus encoding eGFP (Ad-eGFP) or C-terminally FLAG-tagged LRG1 (Ad-LRG1-FL) was administered to obese B6 mice that had been on HFD for 10 weeks (**Figure 4.6A**). Plasma western blot showed robust overexpression 5 days after infection in the Ad-LRG1-FL group compared to Ad-eGFP controls (**Figure 4.6B**). We observed no difference in body weights between groups (**Figure 4.6C**), but an insulin tolerance test (ITT) showed that the Ad-LRG1-FL group had significantly enhanced insulin response ($P = 0.045$) (**Figure 4.6D**).

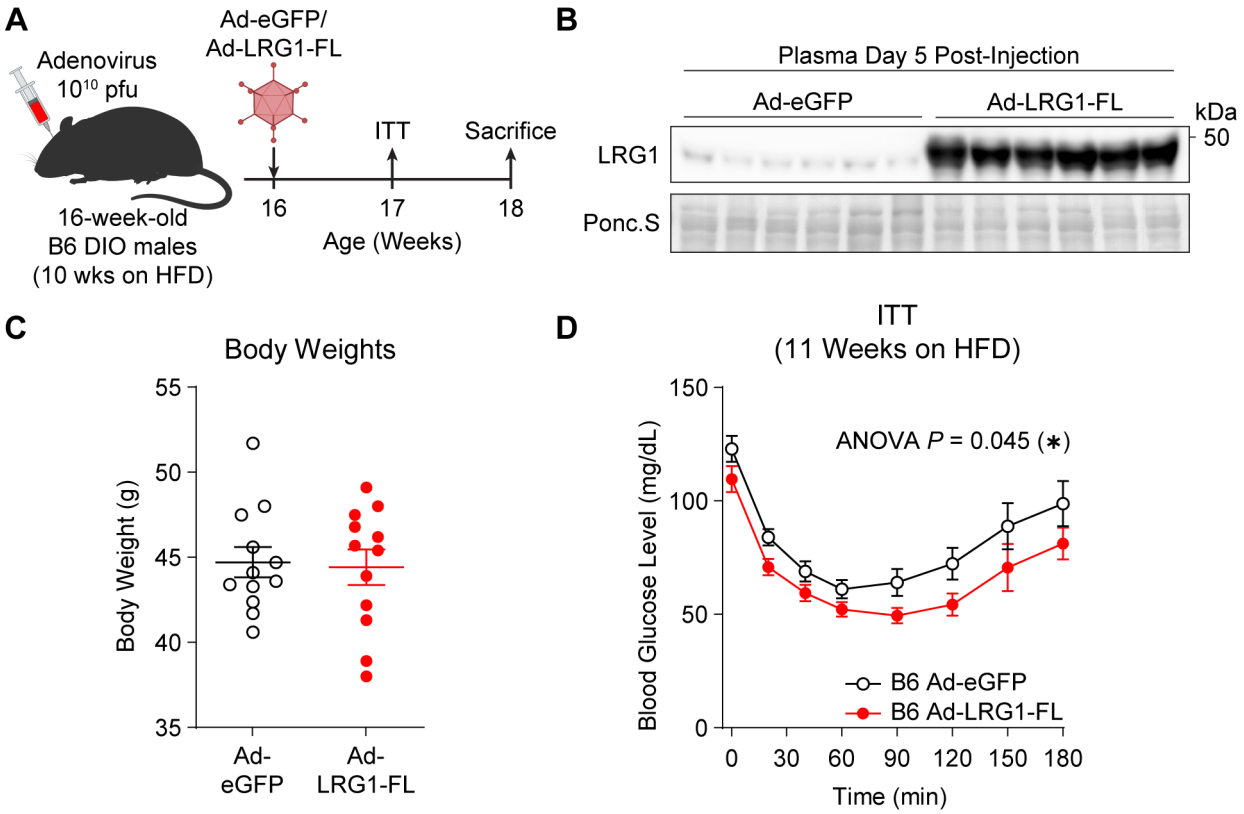

Figure 4.6. Adenovirus-mediated LRG1 overexpression significantly improves insulin tolerance in B6 DIO mice

(**A**) Schematic of Ad vector-mediated acute LRG1 overexpression in B6 DIO male mice. (**B**) Plasma western blot of LRG1 five days after Ad injection. Ponceau S shown as loading control. (**C**) Body weights of 17-week-old B6 DIO males (11 weeks on HFD). (**D**) Insulin tolerance test (1.0 U/kg) in 17-week-old B6 DIO males (11 weeks on HFD). Data are presented as mean ± SEM. ANOVA *P* indicates group factor P-values from repeated measures two-way ANOVA. $*P < 0.05$. $n = 12$ per group.

To study the longitudinal effects of chronic LRG1 overexpression, we administered AAV8-eGFP or AAV8-LRG1-FL to 6-week-old B6 male mice (**Figure 4.7A**). Two weeks after infection, we confirmed overexpression in plasma (**Figure 4.7B**) and started both groups on HFD. Over the following 3 months on HFD, both groups gained an equivalent amount of weight to around 50 g (**Figure 4.7C**). We did not find any significant differences in weights of adipose tissues, liver and gastrocnemius muscle (**Figure 4.7D**). Fasting glucose measurements from 12 to 22 weeks of age (4 to 14 weeks on HFD) showed that the AAV-LRG1-FL group had significantly lower fasting glucose levels ($P = 0.0097$) with a dampened peak (LRG1: 225.9 ± 6.5 mg/dL vs. eGFP: 263.7 ± 10.8 mg/dL, mean ± SEM) at week 18 (**Figure 4.7E**). A glucose tolerance test (GTT) demonstrated that AAV-LRG1-FL mice had markedly improved glucose tolerance ($P = 0.0029$) (**Figure 4.7F**). LRG1-overexpressing animals also showed significantly improved insulin tolerance ($P = 0.023$) (**Figure 4.7G**). Taken together, these observations suggest that LRG1 overexpression prevents obesity-related dysregulation of glucose homeostasis by insulin sensitization.

Figure 4.7. AAV8-mediated chronic LRG1 overexpression significantly improves insulin tolerance in B6 DIO mice

(**A**) Schematic of AAV8-mediated chronic LRG1 overexpression in B6 males. AAV injection was performed in 6-week-old B6 males. HFD was started at 8 weeks of age. (**B**) Plasma western blot of LRG1 two weeks after AAV injection. Ponceau S shown as loading control. (**C**) Body weights of AAV-transduced B6 male mice during HFD challenge. (**D**) Weights of dissected tissues from AAV-transduced B6 male mice at 21 weeks of age (13 weeks on HFD). (**E**) 6 h fasting blood glucose levels of AAV-transduced B6 male mice during HFD feeding. (**F**) Intraperitoneal glucose tolerance test (1.5 g/kg) AAV-transduced B6 males at 18 weeks of age (10 weeks on HFD). (**G**) Insulin tolerance test (1.5 U/kg) of AAV-transduced B6 males at 20 weeks of age (12 weeks on HFD). Data are presented as mean ± SEM. ANOVA *P* indicates group factor *P*-values from repeated measures two-way ANOVA. Where indicated, P-values from Šídák post hoc tests are reported. **P* < 0.05. ***P* < 0.01. ****P* < 0.001. *****P* < 0.0001. *n* = 12 per group.

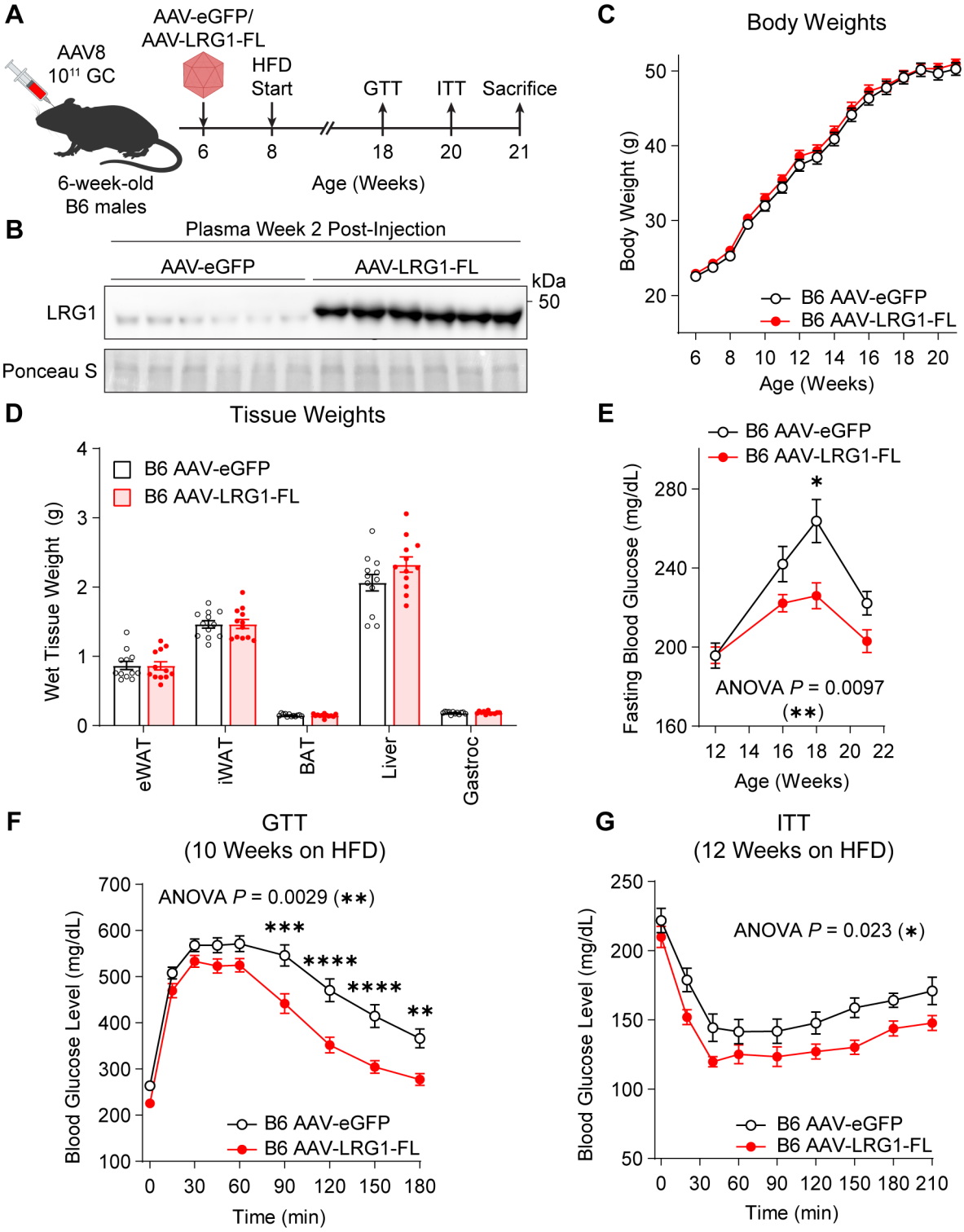
A
AAV8
10^11 GC
AAV-eGFP/
AAV-LRG1-FL
HFD
Start
GTT
ITT
Sacrifice
6
8
18
20
21
Age (Weeks)
6-week-old
B6 males
B
Plasma Week 2 Post-Injection
AAV-eGFP
AAV-LRG1-FL
kDa
50
LRG1
Ponceau S
C
Body Weights
Body Weight (g)
B6 AAV-eGFP
B6 AAV-LRG1-FL
Age (Weeks)
D
Tissue Weights
Wet Tissue Weight (g)
B6 AAV-eGFP
B6 AAV-LRG1-FL
eWAT
iWAT
BAT
Liver
Gastroc
E
Fasting Blood Glucose (mg/dL)
ANOVA P = 0.0097
(**)
Age (Weeks)
F
GTT
(10 Weeks on HFD)
ANOVA P = 0.0029 (**)
Blood Glucose Level (mg/dL)
Time (min)
G
ITT
(12 Weeks on HFD)
ANOVA P = 0.023 (*)
Blood Glucose Level (mg/dL)
Time (min)

4.5 Metabolic characterization of LRG1-KO mice

To test whether LRG1 loss of function affects glucose homeostasis, we generated whole-body LRG1-KO animals in the B6 background using CRISPR-Cas9 with a gRNA targeting the 5' portion of exon 2 of Lrg1 (**Figure 4.8A**). This led to a frameshift mutation in *Lrg1* that eventually led to a premature stop codon (**Figure 4.8B**), and plasma western blot confirmed the absence of LRG1 protein (**Figure 4.8C**).

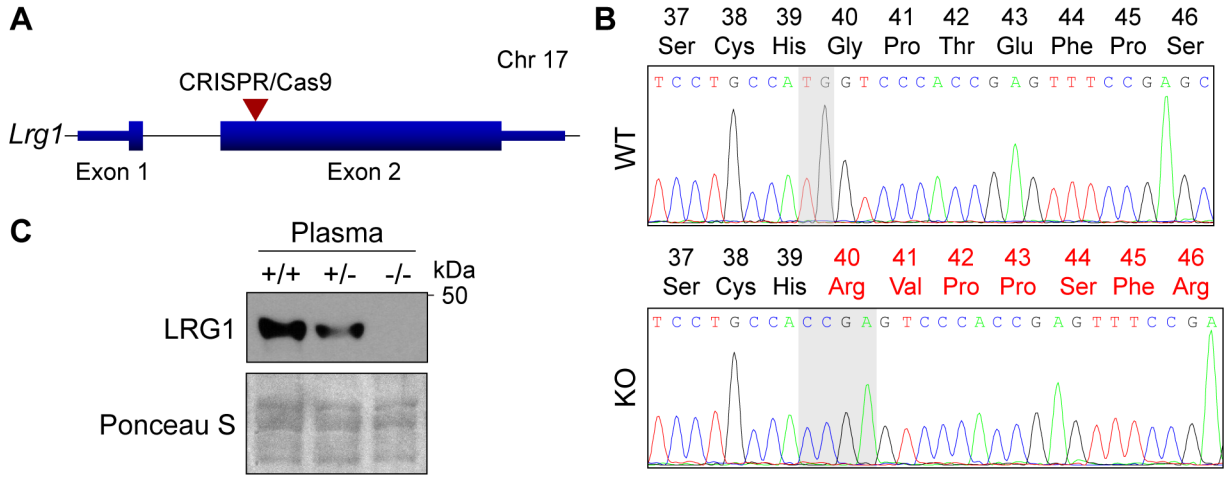

Figure 4.8. Generation of whole-body LRG1-KO (*Lrg1*$^{-/-}$) mice

(**A**) Schematic diagram of murine *Lrg1* exon structure in chromosome 17. Red arrowhead indicates the region targeted by CRISPR/Cas9 gRNA. (**B**) Sanger sequencing chromatogram of PCR products amplifying a portion of *Lrg1* exon 2. Shaded portion highlights where sequences differ between WT and LRG1-KO alleles. LRG1 amino acid positions and residues encoded by each allele are indicated above each trace, mutant amino acid residues highlighted in red. (**C**) Western blot of LRG1 protein in plasma of WT (+/+), LRG1-heterozygote (+/-), and LRG1-KO mice (-/-). Ponceau S shown as loading control.

Having confirmed the successful generation of a KO line, we performed similar metabolic characterization studies on these mice. LRG1-KO (*Lrg1*$^{-/-}$) animals and WT (*Lrg1*$^{+/+}$) littermate controls were fed HFD starting at 6 weeks of age. We observed no difference in body weight between the two genotypes in males or females (**Figure 4.9A**) or in tissue weights (**Figure 4.9B**).

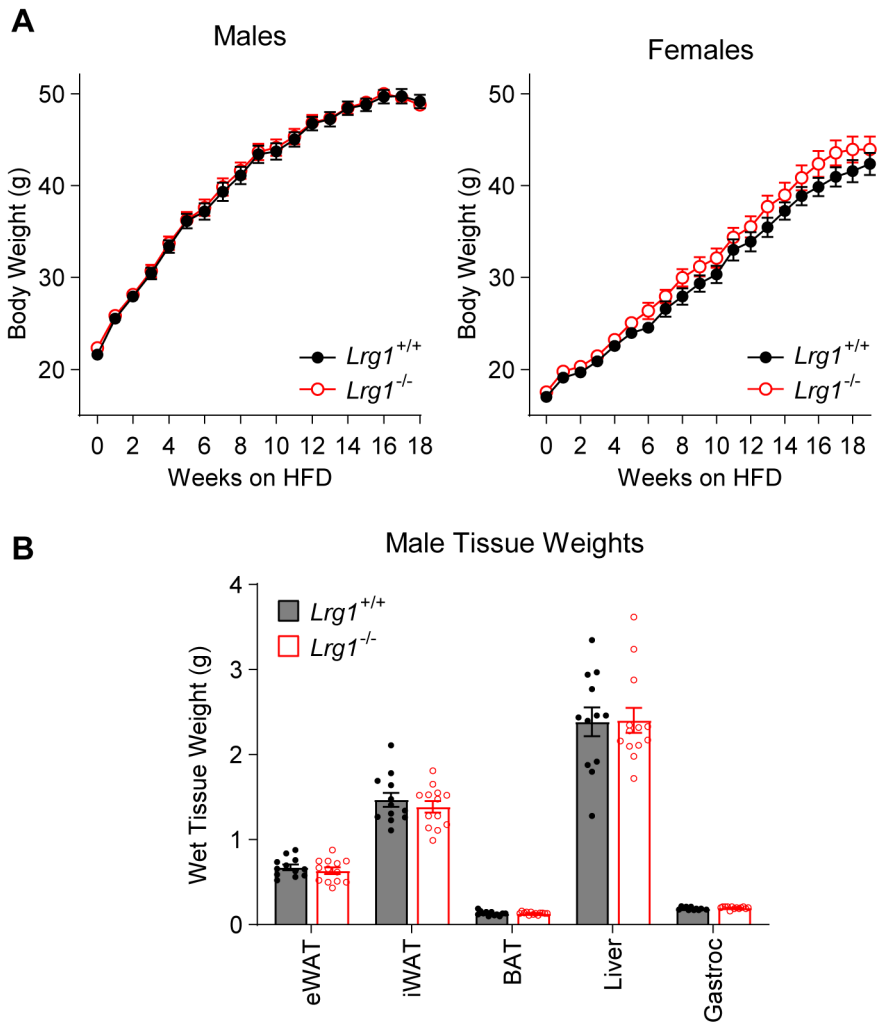

Figure 4.9. Whole body and tissue weights of LRG1-KO and WT littermate mice
(**A**) Body weights of LRG1-KO and WT littermate males (left) and females (right) on HFD started at 6 weeks of age. (**B**) Weights of dissected tissues from LRG1-KO and WT littermate males at 24 weeks of age (18 weeks on HFD). Data are presented as mean ± SEM. Males: n = 12 for WT and n = 13 for LRG1-KO. Females: n = 12 for WT and n = 16 for LRG1-KO.

Interestingly, male LRG1-KO animals demonstrated significantly higher fasting glucose levels compared to WT littermates throughout the HFD challenge (P = 0.010) with a higher peak (KO: 261.6 ± 11.3 mg/dL vs. eGFP: 225.0 ± 10.9 mg/dL, mean ± SEM) at week 12 on HFD (**Figure 4.10A**). However, GTT and ITT did not show differences in glucose homeostasis between the genotypes (**Figures 4.10B-E**). Therefore, while LRG1 overexpression significantly improves metabolic health in B6 animals upon HFD challenge, the impact of LRG1 loss of function on whole-body energy homeostasis appears more subtle in a DIO model.

Figure 4.10. Metabolic characterization of LRG1-KO mice
(**A**) 6 h fasting blood glucose levels of LRG1-KO and WT littermate males during HFD feeding. (**B**) Intraperitoneal glucose tolerance test (1.5 g/kg) of LRG1-KO and WT littermate male mice performed at 18 weeks of age (12 weeks on HFD). (**C**) Insulin tolerance test (1.5 U/kg) of LRG1-KO and WT littermate male mice performed at 22 weeks of age (16 weeks on HFD). (**D**) Intraperitoneal glucose tolerance test (1.75 g/kg) of LRG1-KO and WT littermate female mice performed at 22 weeks of age (16 weeks on HFD). (**E**) Insulin tolerance test (1.0 U/kg) of LRG1-KO and WT littermate female mice performed at 24 weeks of age (18 weeks on HFD). Data are presented as mean ± SEM. ANOVA *P* indicates group factor P-values from repeated measures two-way ANOVA. **P* < 0.05. Males: *n* = 12 for WT and *n* = 13 for LRG1-KO. Females: *n* = 12 for WT and *n* = 16 for LRG1-KO.

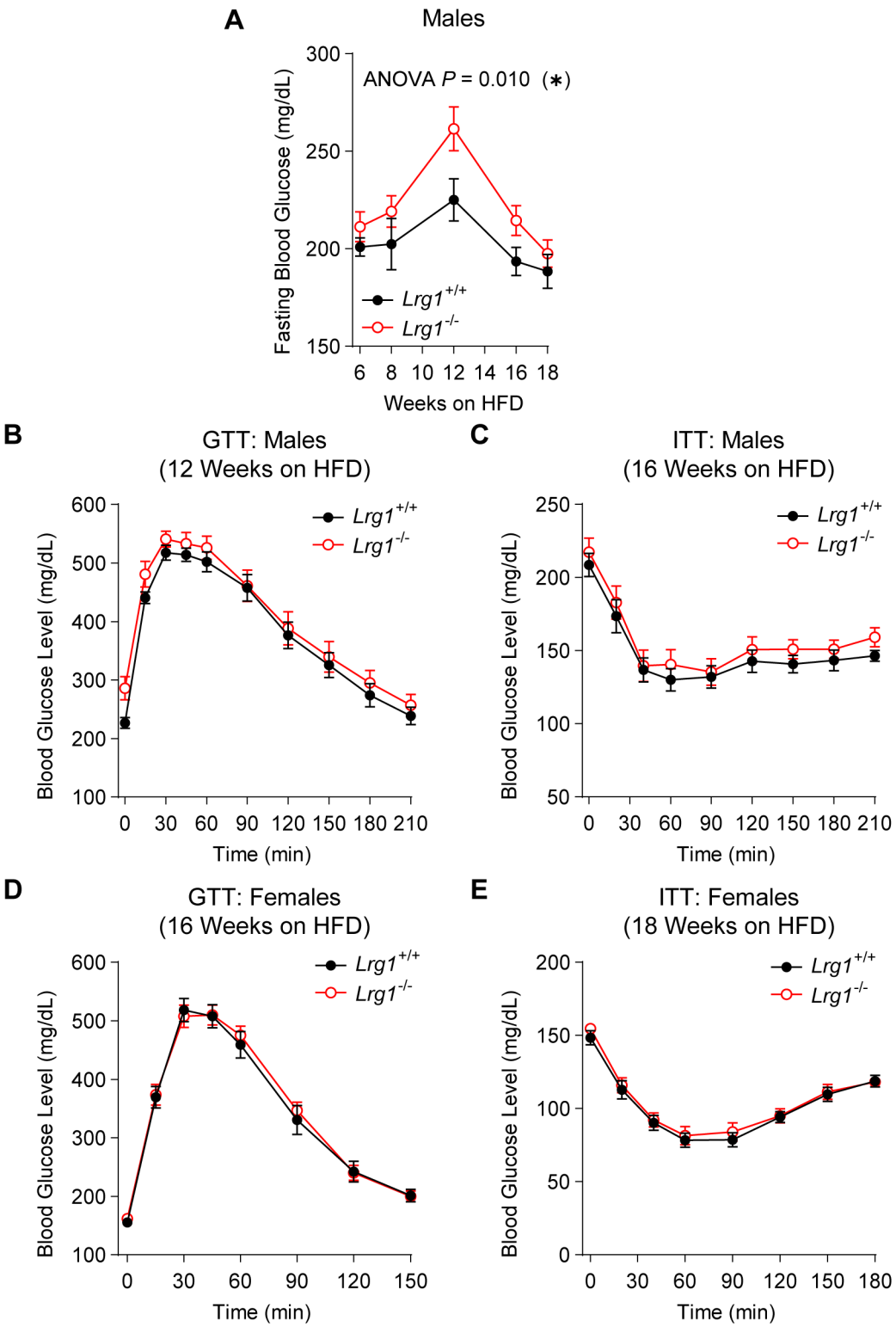
A
Males
ANOVA P = 0.010 (*)
Fasting Blood Glucose (mg/dL)
Weeks on HFD
Lrg1+/+
Lrg1-/-
B
GTT: Males
(12 Weeks on HFD)
Blood Glucose Level (mg/dL)
Time (min)
C
ITT: Males
(16 Weeks on HFD)
D
GTT: Females
(16 Weeks on HFD)
E
ITT: Females
(18 Weeks on HFD)

4.6 LRG1 overexpression delays onset of diabetic phenotype and promotes WAT expansion in *db/db* mice

While B6 mice develop severe obesity upon HFD feeding, they demonstrate only transient and mild hyperglycemia with moderate insulin resistance (Winzell and Ahrén, 2004; Kleinert et al., 2018). Because LRG1 overexpression in B6 animals mitigated hyperglycemia, we explored whether LRG1 can improve glucose homeostasis in C57BLKS/J-*Lepr*$^{db/db}$ (*db/db*) mice, a more extreme model of obesity-related type 2 diabetes. Due to the interaction between a leptin receptor (*Lepr*) mutation and genetic background, *db/db* animals demonstrate hyperphagia and early-onset obesity, along with profound hyperglycemia and hyperinsulinemia (Kleinert et al., 2018). We confirmed that *db/db* animals develop profound obesity with 40 g of body weight and hyperglycemia over 400 mg/dL as early as 7 weeks of age, while littermate misty mice with a WT *Lepr* gene (*m/m*) maintain body weights below 25 g and fasting glucose levels under 200 mg/dL (**Figures 4.11A and B**). Similar to B6 DIO animals, *db/db* animals showed higher circulating LRG1 levels compared to lean littermates (**Figure 4.11C**).

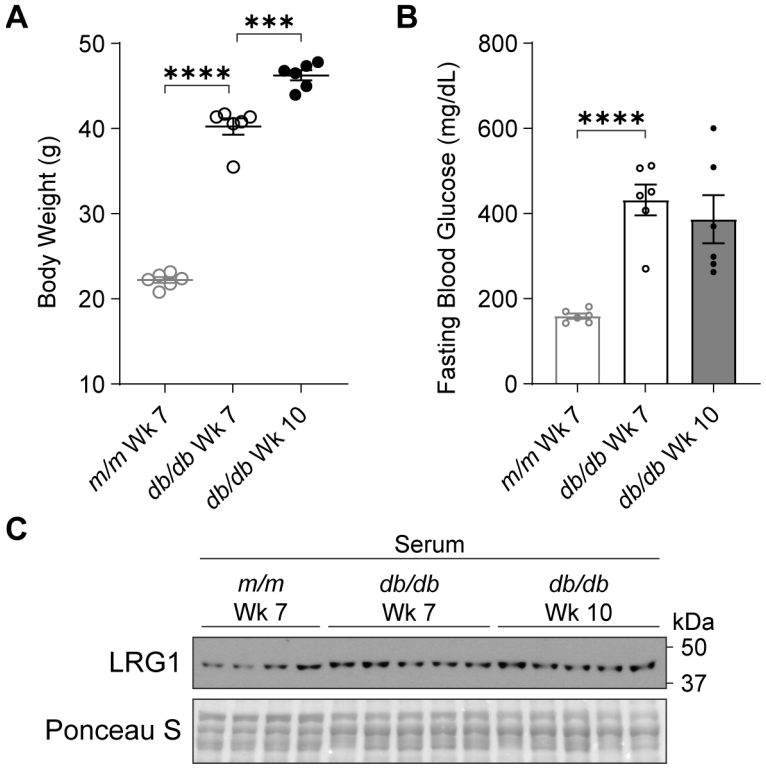

Figure 4.11. Characterization of *db/db* and littermate *m/m* mice

(**A**) Body weights of *db/db* and littermate *m/m* male mice with WT *Lepr* gene at 7 and 10 weeks of age. ***$P < 0.001$, ****$P < 0.0001$ from Welch's *t*-test. $n = 6$ per group. (**B**) 6 h fasting blood glucose levels of *db/db* and littermate *m/m* male mice at 7 and 10 weeks of age. ****$P < 0.0001$ from Welch's *t*-test. $n = 6$ per group. Data are presented as mean ± SEM. (**C**) Western blot of LRG1 in serum of *db/db* and littermate *m/m* male mice. Ponceau S shown as loading control.

We administered AAV-eGFP or AAV-LRG1-FL to *db/db* animals at 4 weeks of age, before development of severe hyperglycemia (**Figures 4.12A and B**). Starting two weeks post injection, LRG1-overexpressing animals demonstrated accelerated weight gain, such that by 10 weeks of

age the LRG1 group weighed 19.6% more (P = 0.004) than eGFP controls (**Figures 4.12C**). During this period, we also observed that cages housing LRG1-overexpressing animals tended to have greater food intake.

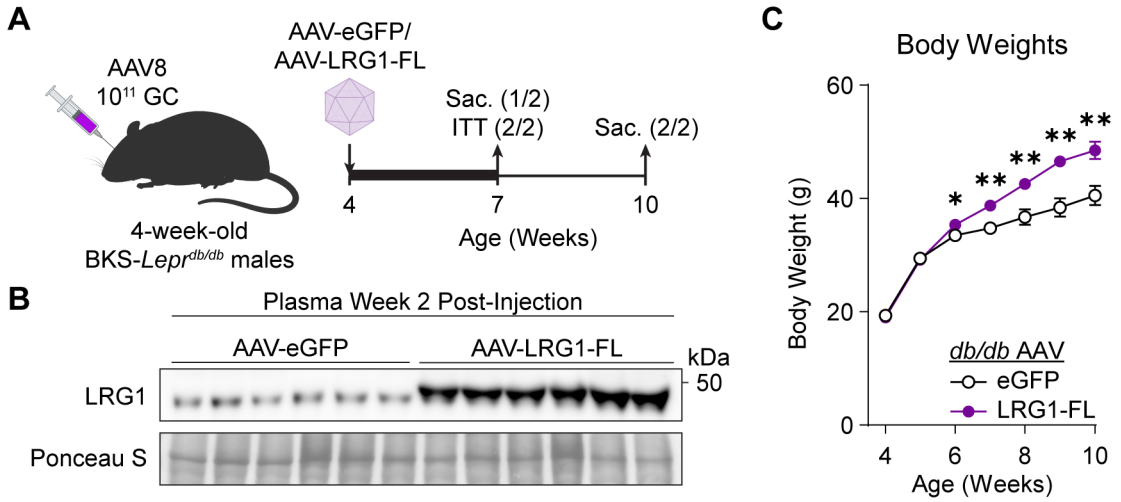

Figure 4.12. AAV8-mediated LRG1 overexpression in *db/db* mice
(**A**) Schematic of AAV8-mediated LRG1 overexpression in *db/db* males. (**B**) Plasma western blot of LRG1 two weeks after AAV injection. Ponceau S shown as loading control. (**C**) Body weights of AAV-transduced *db/db* male mice on standard chow diet. Data are presented as mean ± SEM. *P < 0.05, **P < 0.01 from Welch's t-test. n = 16 per group for weeks 4-6; n = 7-8 per group for weeks 7-10.

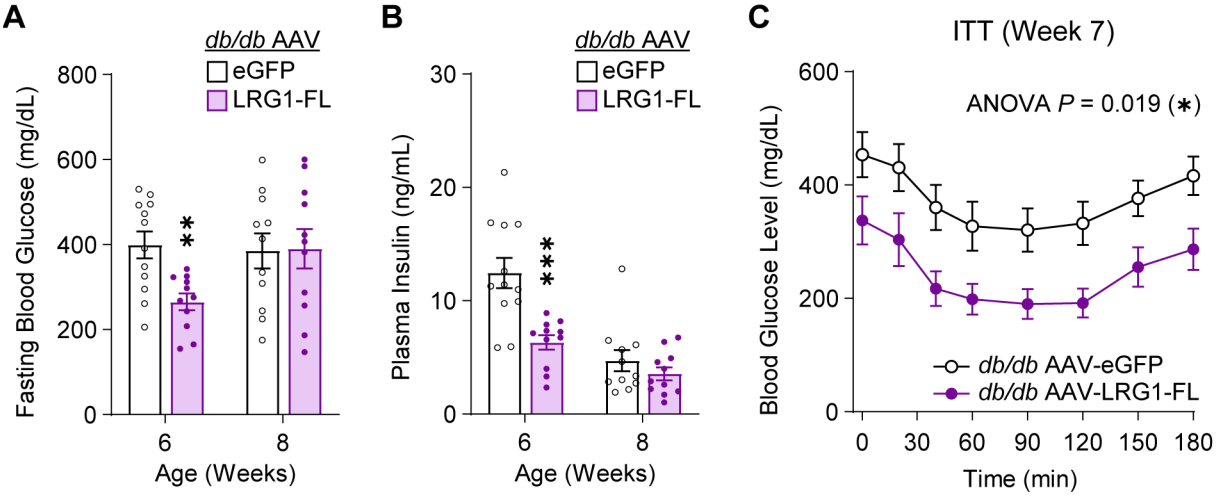

Figure 4.13. LRG1 overexpression delays diabetic phenotype in *db/db* mice
(**A**) 6 h fasting blood glucose levels of AAV-transduced *db/db* male mice at 6 and 8 weeks of age. **P < 0.01 from Welch's t-test. n = 11-12 per group. (**B**) Plasma insulin levels from (**A**). ***P < 0.001 from Welch's t-test. (**C**) Insulin tolerance test (2.0 U/kg) of AAV-transduced 7-week-old *db/db* male mice. Data are presented as mean ± SEM. ANOVA P indicates group factor P-value from repeated measures two-way ANOVA. *P < 0.05. n = 7-8 per group.

Concomitantly, the AAV-LRG1-FL group showed delayed onset of hyperglycemia. At week 6, we observed frank hyperglycemia in eGFP animals, whereas levels in the LRG1 group were 33.6% lower (eGFP: 399.5 ± 31.7 mg/dL vs. LRG1: 265.4 ± 19.6 mg/dL, mean ± SEM; $P = 0.0020$) (**Figure 4.13A**). Fasting plasma insulin levels were almost halved in the LRG1 group (eGFP: 12.5 ± 1.3 ng/mL vs. LRG1: 6.3 ± 0.6 ng/mL, mean ± SEM; $P = 0.0008$) (**Figure 4.13B**). Consistent with these findings, an ITT showed that LRG1-overexpressing animals demonstrated significantly improved insulin sensitivity ($P = 0.019$) (**Figure 4.13C**). By 8 weeks of age, body weights continued to diverge between the groups (**Figure 4.12C**), but we no longer observed significant differences in fasting blood glucose or plasma insulin concentrations (**Figures 4.13A-C**).

Tissue weight measurements revealed that LRG1-overexpressing animals had accelerated gain of eWAT ($P < 0.0001$) and iWAT ($P = 0.0001$) mass, such that by week 10, their eWAT and iWAT were 53% and 40% heavier, respectively, than in eGFP controls (**Figures 4.14A and B**). We observed no difference in weights of BAT, liver, and gastrocnemius muscle (**Figure 4.14A**). These results reveal that LRG1 overexpression in *db/db* animals promotes insulin sensitivity and WAT expansion-driven weight gain.

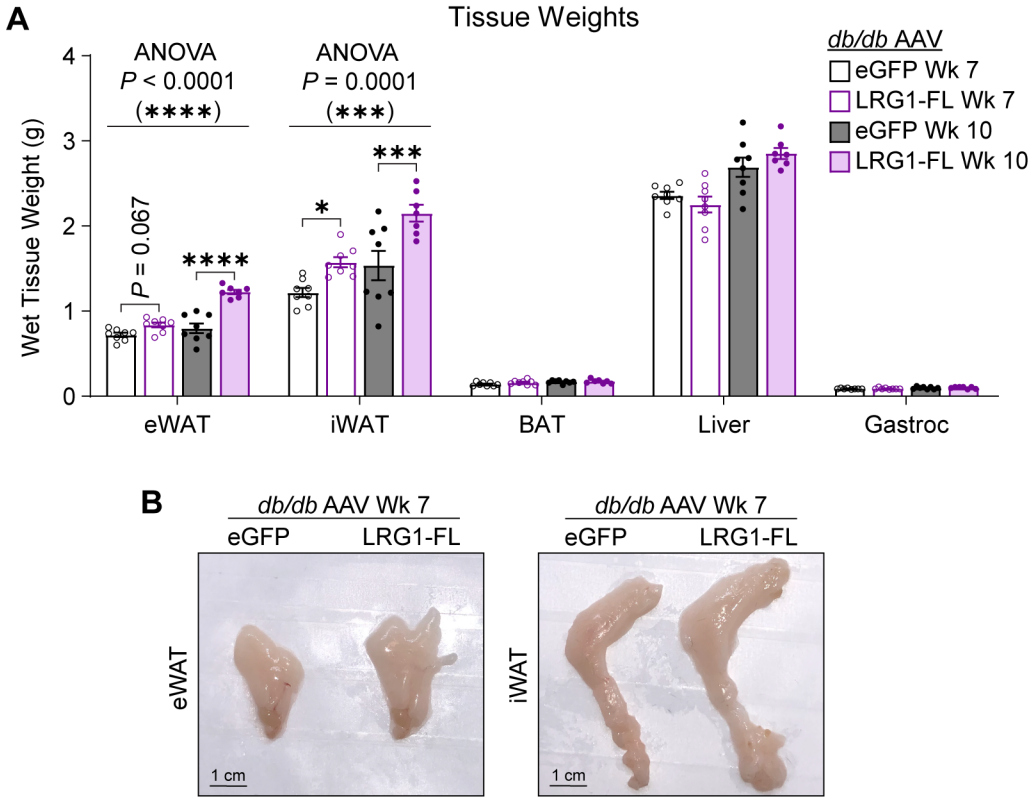

Figure 4.14. LRG1 overexpression in *db/db* mice accelerates white adipose tissue expansion
(**A**) Weights of dissected tissues from AAV-transduced *db/db* male mice at 7 and 10 weeks of age. ANOVA *P* indicates group factor *P*-values from two-way mixed effects ANOVA. Where indicated, *P*-values from Šídák post hoc tests reported. $^{**}P < 0.01$, $^{***}P < 0.001$, $^{****}P < 0.0001$. $n = 7$-8 per group. (**B**) eWAT and iWAT of AAV-eGFP or AAV-LRG1-FL transduced *db/db* male mice at 7 weeks of age. Data are presented as mean ± SEM.

4.7 LRG1 suppresses obesity-associated systemic inflammation

To uncover the physiological process underlying LRG1-mediated insulin sensitization, we turned to our observation that LRG1-overexpressing *db/db* animals demonstrated accelerated eWAT and iWAT expansion and hypothesized that WAT could be one of the targets of LRG1 action. We analyzed paraffin-embedded, hematoxylin and eosin (H&E) stained tissue sections and found that eWAT from B6 animals sacrificed at 21 weeks of age (13 weeks on HFD) was characterized by accumulation of macrophages forming crown-like structures (CLS) (**Figure 4.15A**). The distal portion of eWAT was especially susceptible to CLS formation in eGFP controls, while the same region in LRG1-overexpressing animals displayed an 82% reduction in CLS number ($P < 0.0001$). iWAT from B6 animals contained fewer CLS compared to eWAT and did not show major morphological differences between groups (**Figure 4.15B**).

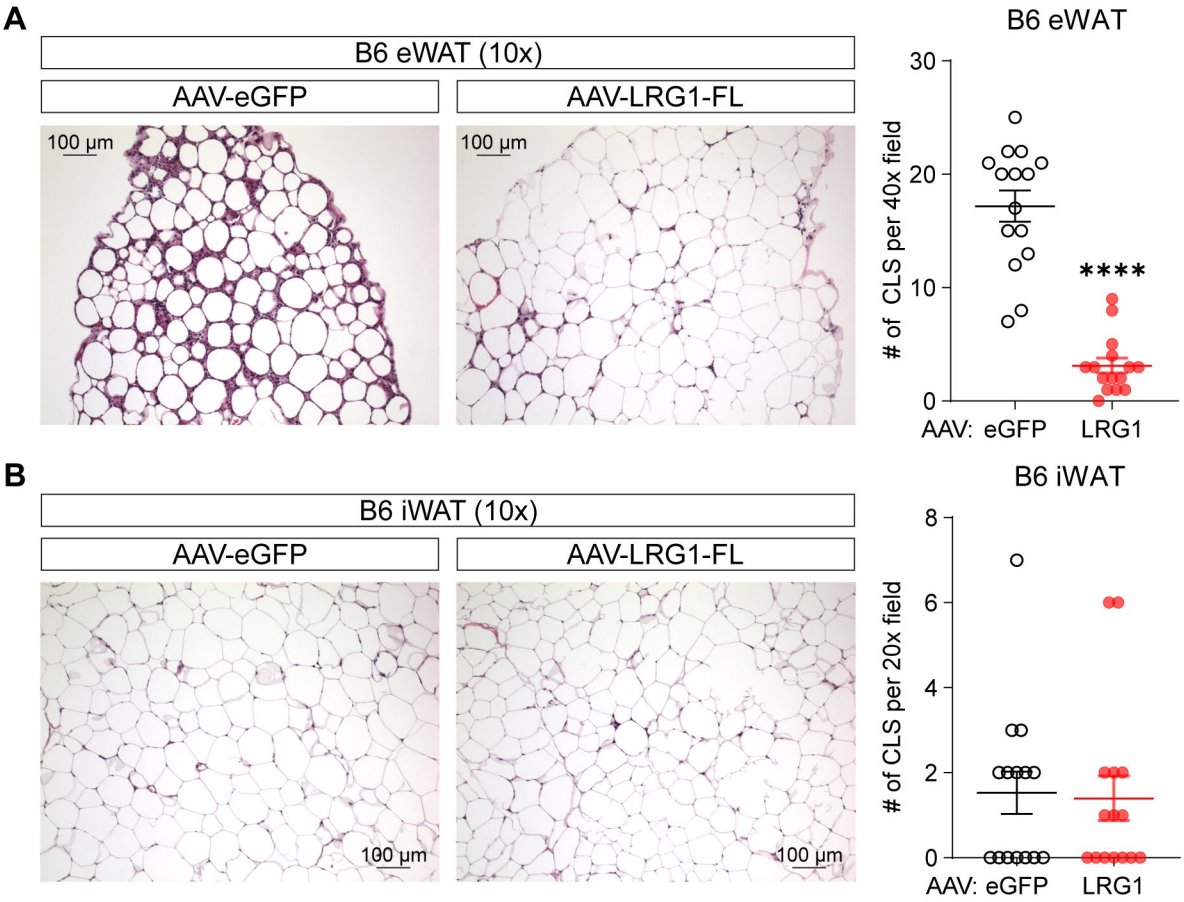

Figure 4.15. LRG1-overexpressing B6 mice have reduced inflammation in eWAT
(**A-B**) Representative images from H&E-stained eWAT (A) and iWAT (B) sections under a 10x objective and quantification of CLS from B6 DIO mice transduced with AAV-eGFP or AAV-LRG1-FL. Scale bars are indicated. Data are presented as mean ± SEM. ****$P < 0.0001$ from Welch's *t*-test. 5 fields under indicated objectives from 3 animals were used for quantification ($n = 15$ per group).

In *db/db* eWAT, we observed significantly reduced CLS in the LRG1 group by 81% at week 7 ($P = 0.0001$) and 85% at week 10 ($P < 0.0001$) (**Figure 4.16**). Similarly, CLS in iWAT from

LRG1-overexpressing animals were reduced by 83% at week 7 (P = 0.0043) and 88% at week 10 (*P* < 0.0001) (**Figure 4.17**).

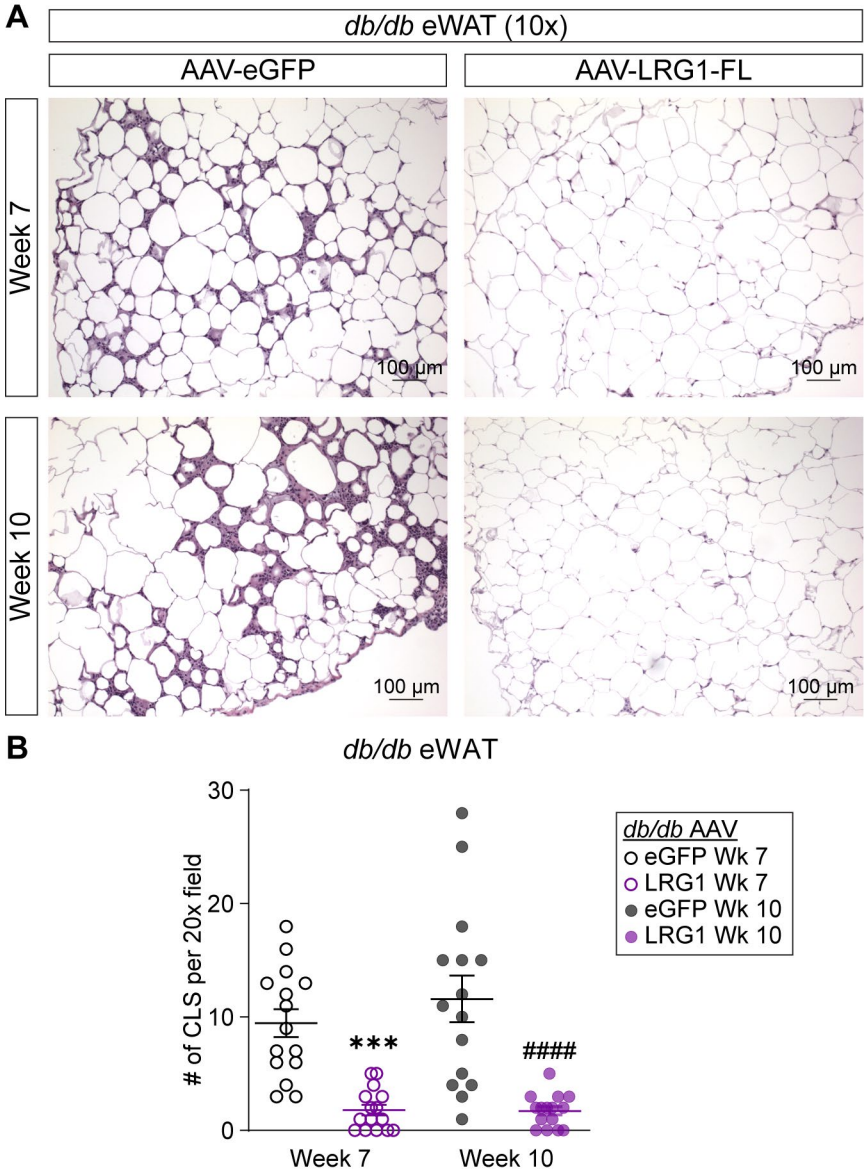

Figure 4.16. LRG1-overexpressing *db/db* mice show reduced eWAT inflammation
(**A**) Representative images from H&E-stained eWAT sections from *db/db* mice transduced with AAV-eGFP or AAV-LRG1-FL. Scale bars are indicated. (**B**) Quantification of CLS in eWAT Data are presented as mean ± SEM. Šídák post hoc test results from two-way ANOVA are indicated. ****P* < 0.001, LRG1 Wk 7 vs. eGFP Wk 7. ####*P* < 0.0001, LRG1 Wk 10 vs. eGFP Wk 10. 5 fields under a 20x objective from 3 animals were used for quantification (*n* = 15 per group).

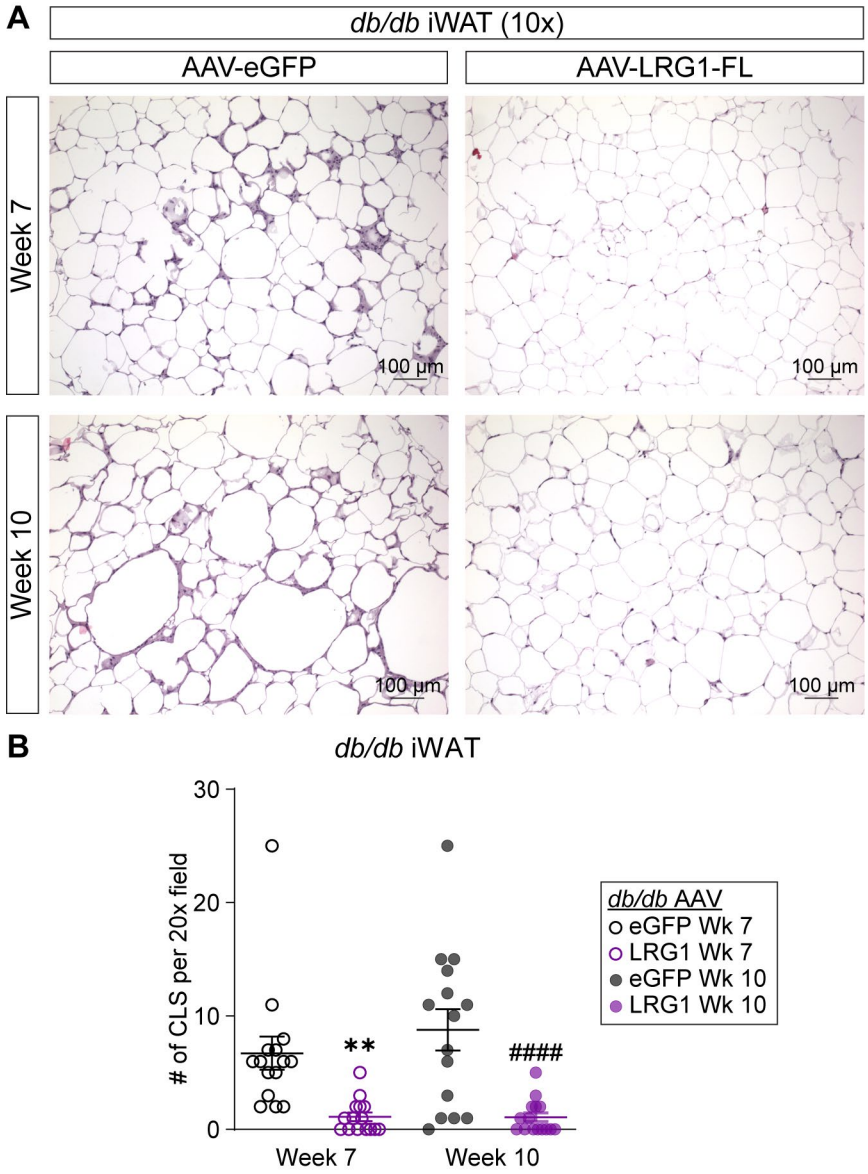

Figure 4.17. LRG1-overexpressing *db/db* mice show reduced iWAT inflammation
(**A**) Representative images from H&E-stained iWAT sections from *db/db* mice transduced with AAV-eGFP or AAV-LRG1-FL. Scale bars are indicated. (**B**) Quantification of CLS in iWAT Data are presented as mean ± SEM. Šídák post hoc test results from two-way ANOVA are indicated. $^{**}P < 0.01$, LRG1 Wk 7 vs. eGFP Wk 7. $^{\#\#\#\#}P < 0.0001$, LRG1 Wk 10 vs. eGFP Wk 10. 5 fields under a 20x objective from 3 animals were used for quantification ($n = 15$ per group).

Obesity is also associated with increased risk of a spectrum of abnormalities in the liver, collectively referred to as non-alcoholic fatty liver disease (NAFLD) (Farrell et al., 2019). NAFLD is characterized by steatosis of the liver with or without inflammation (Farrell et al., 2019). While HFD-fed B6 mice rarely demonstrate liver injury or inflammation, mild necroinflammation can be observed in *db/db* liver as early as 1 month of age (Febbraio et al., 2019; Trak-Smayra et al., 2011). Liver sections from the B6 cohort showed a similar degree of steatosis in both groups, without any inflammatory lesions (**Figure 4.18A**). In the *db/db* cohort, while both eGFP and LRG1 developed

a similar degree of hepatosteatosis, inflammatory foci were found only in eGFP-expressing animals (**Figure 4.18B**).

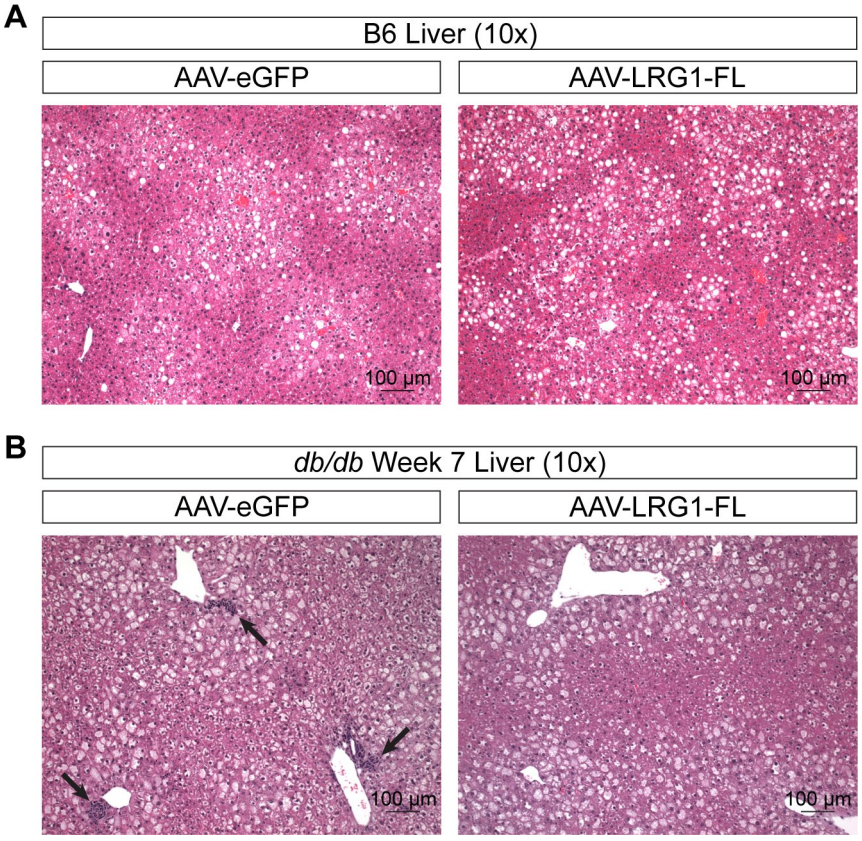

Figure 4.18. LRG1 overexpression reduces liver inflammation in *db/db* mice
(**A-B**) Representative images from H&E-stained liver sections from B6 DIO (A) and *db/db* mice (B) transduced with AAV-eGFP or AAV-LRG1-FL. Arrows indicate liver inflammatory foci. Scale bars are indicated.

Inflammation is a key link between obesity and insulin resistance (Saltiel & Olefsky, 2017). With our observations on tissue morphology, we hypothesized that LRG1 may mediate its insulin sensitizing effect via attenuation of inflammation in susceptible organs. To assess this at the gene expression level, we performed RNA-Seq analysis on eWAT from AAV-treated *db/db* animals harvested at week 7 (midpoint) and week 10 (endpoint). We performed differential gene expression analysis between the eGFP and LRG1 groups at midpoint and subjected the list of significant genes ($P < 0.01$) to GO gene-set enrichment analysis (GSEA). All of the top 20 differentially regulated pathways showed highly significant enrichment ($P = 0.0067$) and were immune-related, including regulation of immune response, regulation of leukocyte activation, innate immune response, and cytokine production (**Figure 4.19**). The enrichment score for each of these pathways was negative in the LRG1 group, indicating down-regulation of inflammatory processes in these animals.

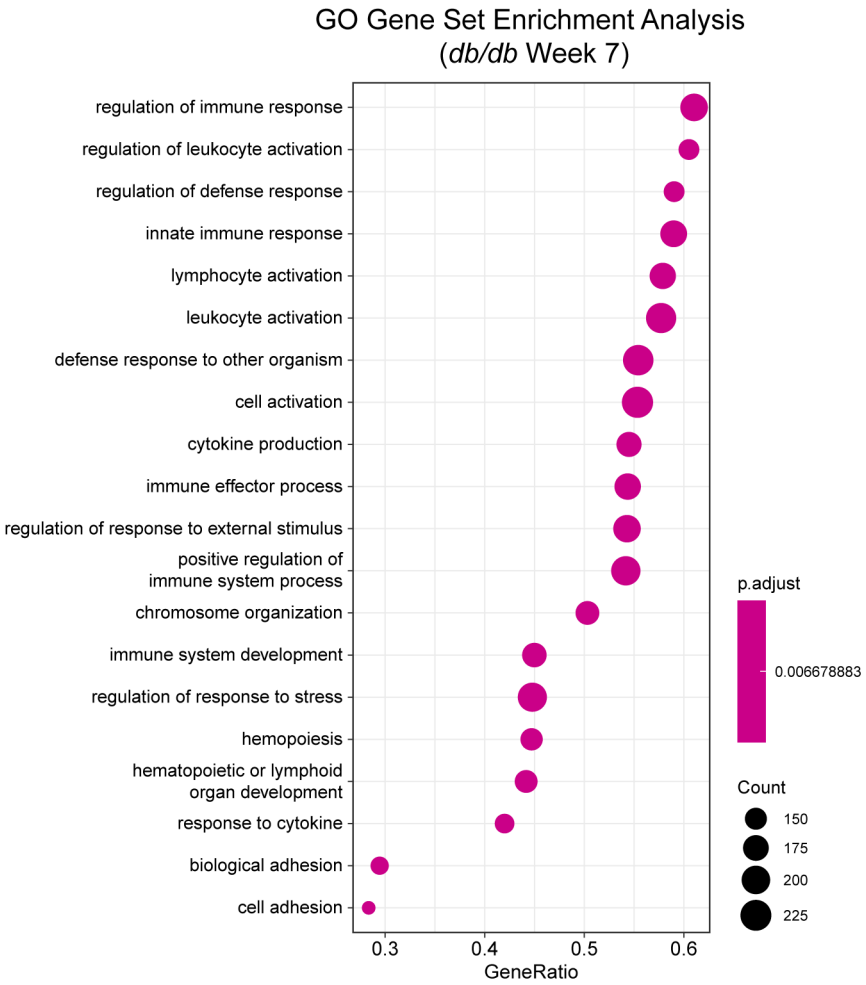

Figure 4.19. Top 20 enriched GO BP pathways from GSEA of significantly differentially expressed genes between *db/db*-LRG1 and *db/db*-eGFP eWAT at 7 weeks of age.

GSEA of significantly regulated genes at the 10-week endpoint yielded similar results. In the LRG1 group, there was significant (P = 0.0082) enrichment and down-regulation of immune-related pathways, including regulation of immune response, immune effector process, leukocyte activation, and cell activation (**Figure 4.20**).

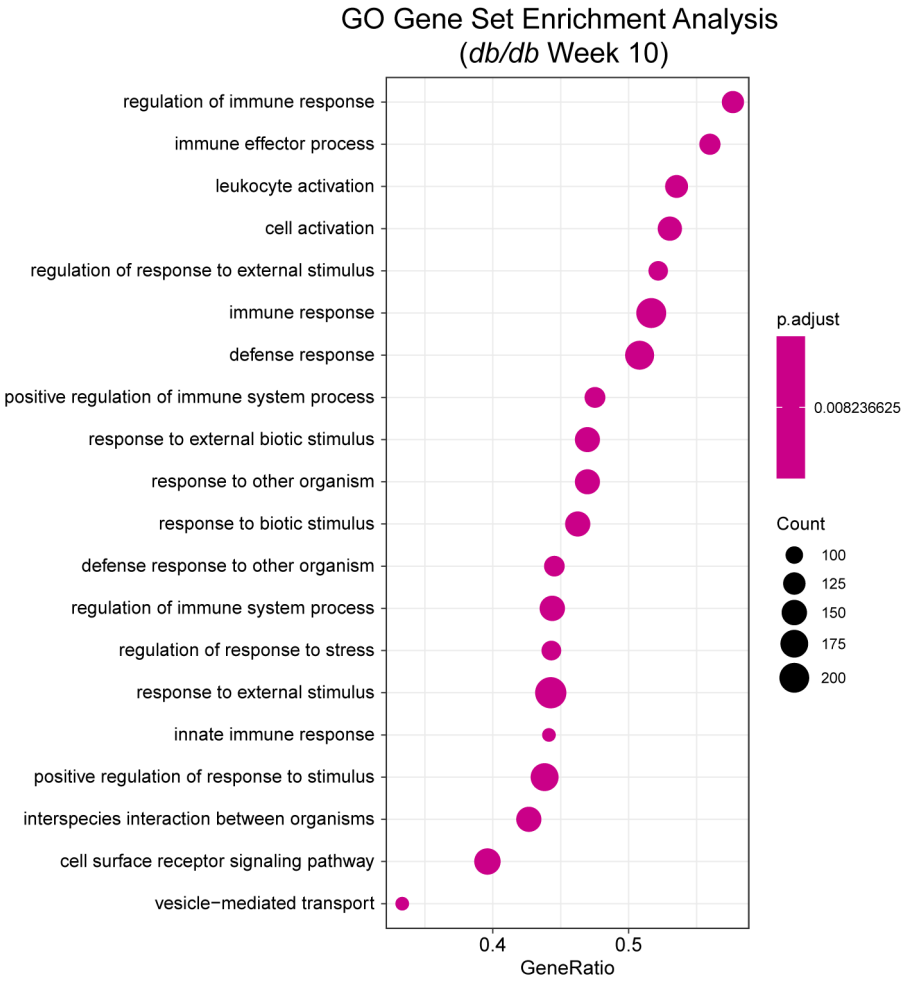

Figure 4.20. Top 20 enriched GO BP pathways from GSEA of significantly differentially expressed genes between *db/db*-LRG1 and *db/db*-eGFP eWAT at 10 weeks of age.

To visualize which genes are most significantly differentially regulated, we plotted a heatmap of 68 genes that showed significant difference (adjusted $P < 0.01$) with Log2 fold-change of >2 or <-2 between the two groups at both week 7 and week 10 time points. Consistent with the pathway analysis, the LRG1 group showed significant down-regulation of cytokines and chemokines such as *Ccl3*, *Ccl4*, and *Cxcl9*; metalloproteinases such as *Mmp12* and *Mmp13* known to be highly expressed by macrophages; and various immunoglobulin subunit genes (**Figure 4.21**). While the vast majority of differentially regulated genes were down-regulated in AAV-LRG1-FL-treated animals, upregulated genes included *Tfr2*, *Spock1*, *Brinp2*, and *Atp4b*, of which *Spock1* has been shown to promote adipogenesis (Alshargabi et al., 2020).

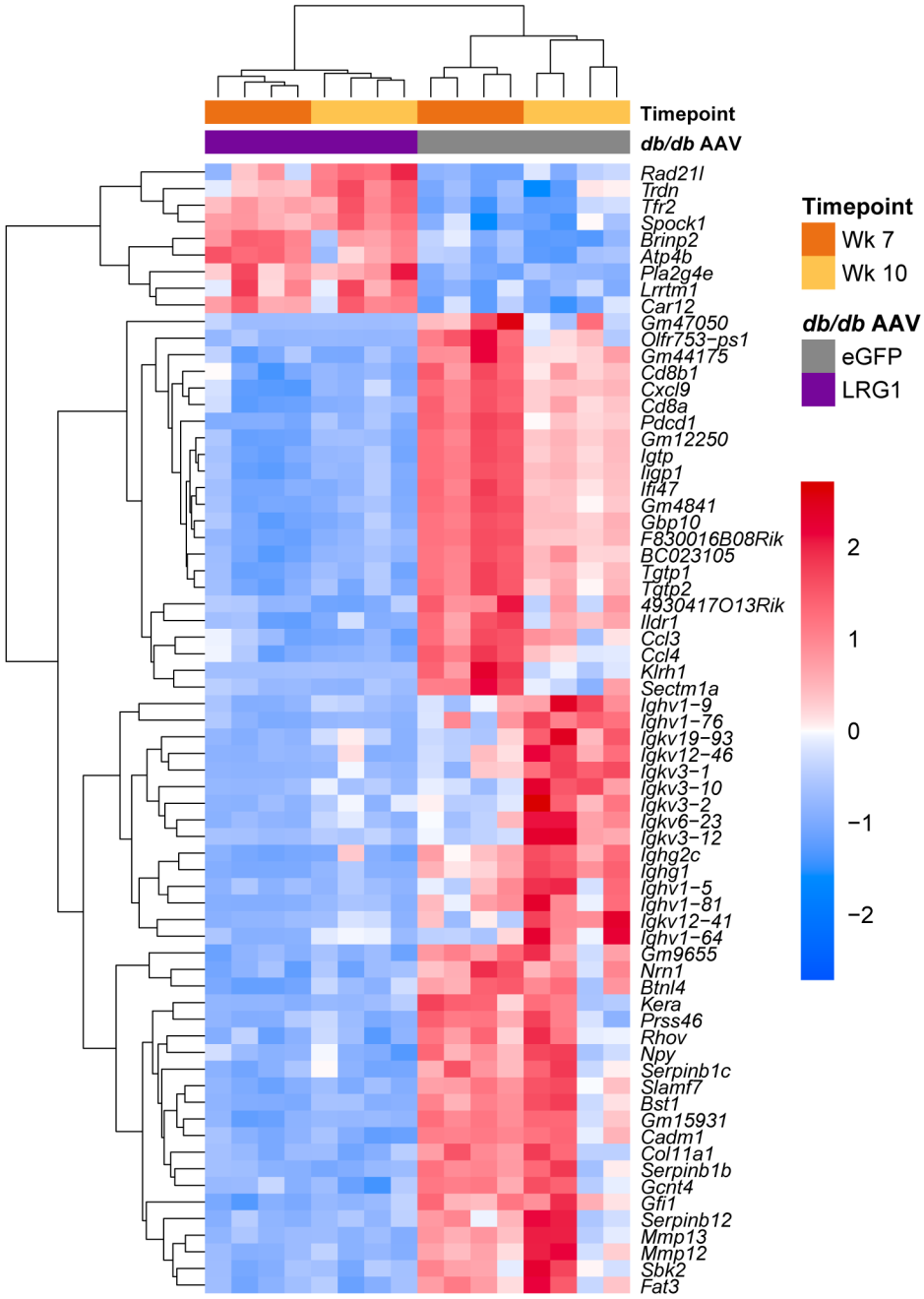

Figure 4.21. Heatmap of 68 differentially regulated genes ($Log_2FC > 2$ or < -2 and adjusted $P < 0.01$) between *db/db*-LRG1 and *db/db*-eGFP eWAT at both 7 and 10 weeks of age.

Our histological analysis demonstrated significantly lower macrophage infiltration in eWAT of LRG1-overexpressing animals. Deconvolution algorithms such as CIBERSORTx allow estimation of cell populations from bulk RNA-Seq datasets (Newman et al., 2019). We performed CIBERSORTx analysis on the expression dataset to gain further insight into differences in immune cell populations. Overall, CIBERSORTx estimated that the LRG1 group contains fewer immune cells (**Figure 4.22A**). Macrophages were predicted to constitute the majority of immune cells in every eWAT sample analyzed, and the LRG1 group demonstrated a lower absolute quantity of macrophages (**Figure 4.22A**), without affecting their relative proportions (**Figure 4.22B**).

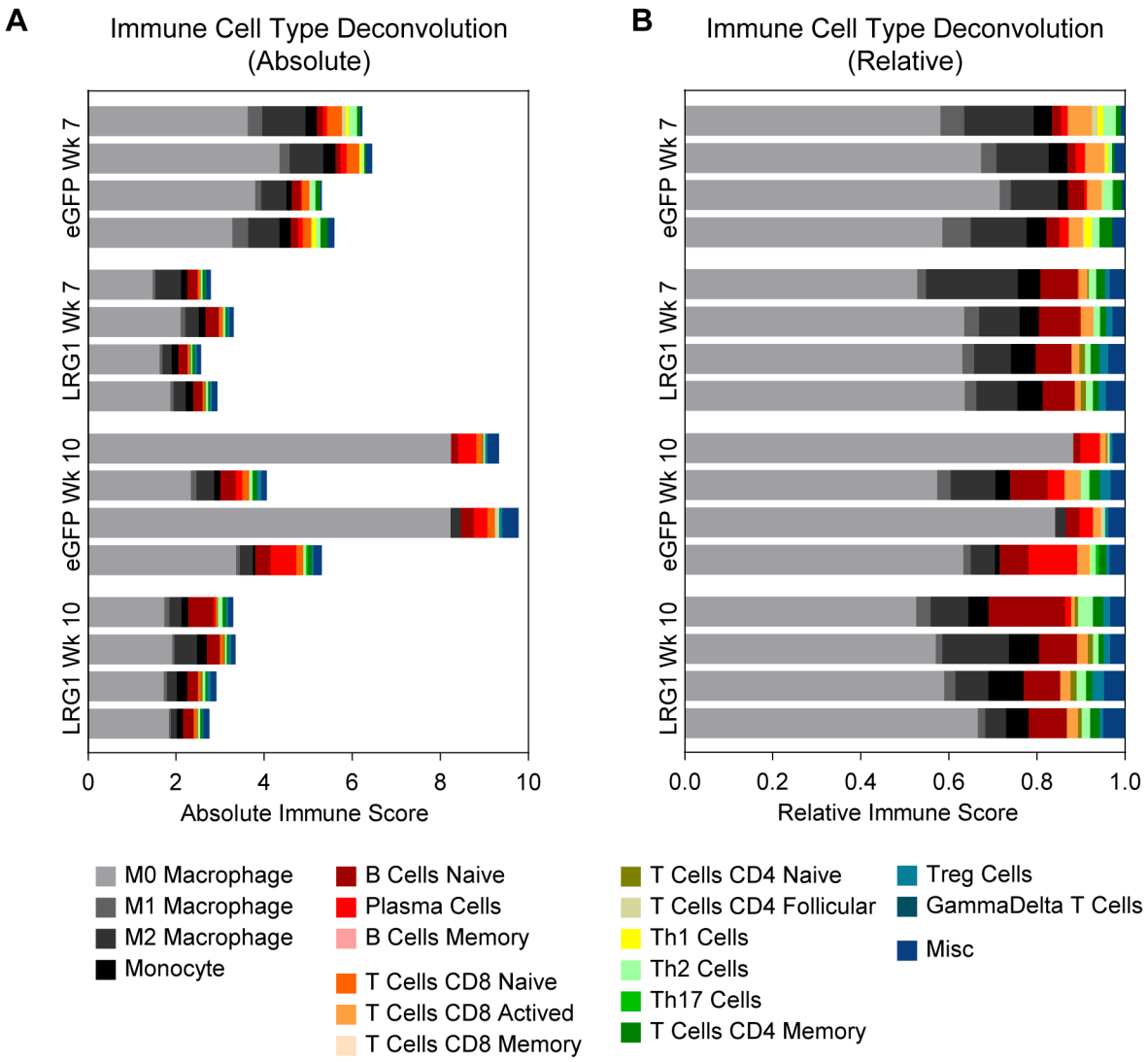

Figure 4.22. Immune cell type deconvolution of *db/db* eWAT.
(**A-B**) Absolute (**A**) and relative (**B**) scores from immune cell type deconvolution analysis of transcriptomes using CIBERSORTx.

Many of the differentially regulated genes between eGFP- and LRG1-overexpressing animals encode chemokines and cytokines. We performed a multiplex cytokine assay to assess whether these differences are reflected in serum levels. Quantification of serum chemokine and cytokine levels showed that at midpoint (week 7), the LRG1 group showed 28-86% reduction of circulating chemokines such as MCP-1, MIP-1α, MIG, and IP-10 and cytokines such as TNFα and IFN-γ (**Figure 4.23A**). Many of these differences subsided by week 10, mostly due to a reduction of cytokines in the eGFP group (**Figure 4.23B**). Taken together, these results suggest that LRG1-overexpression attenuated pro-inflammatory processes associated with obesity.

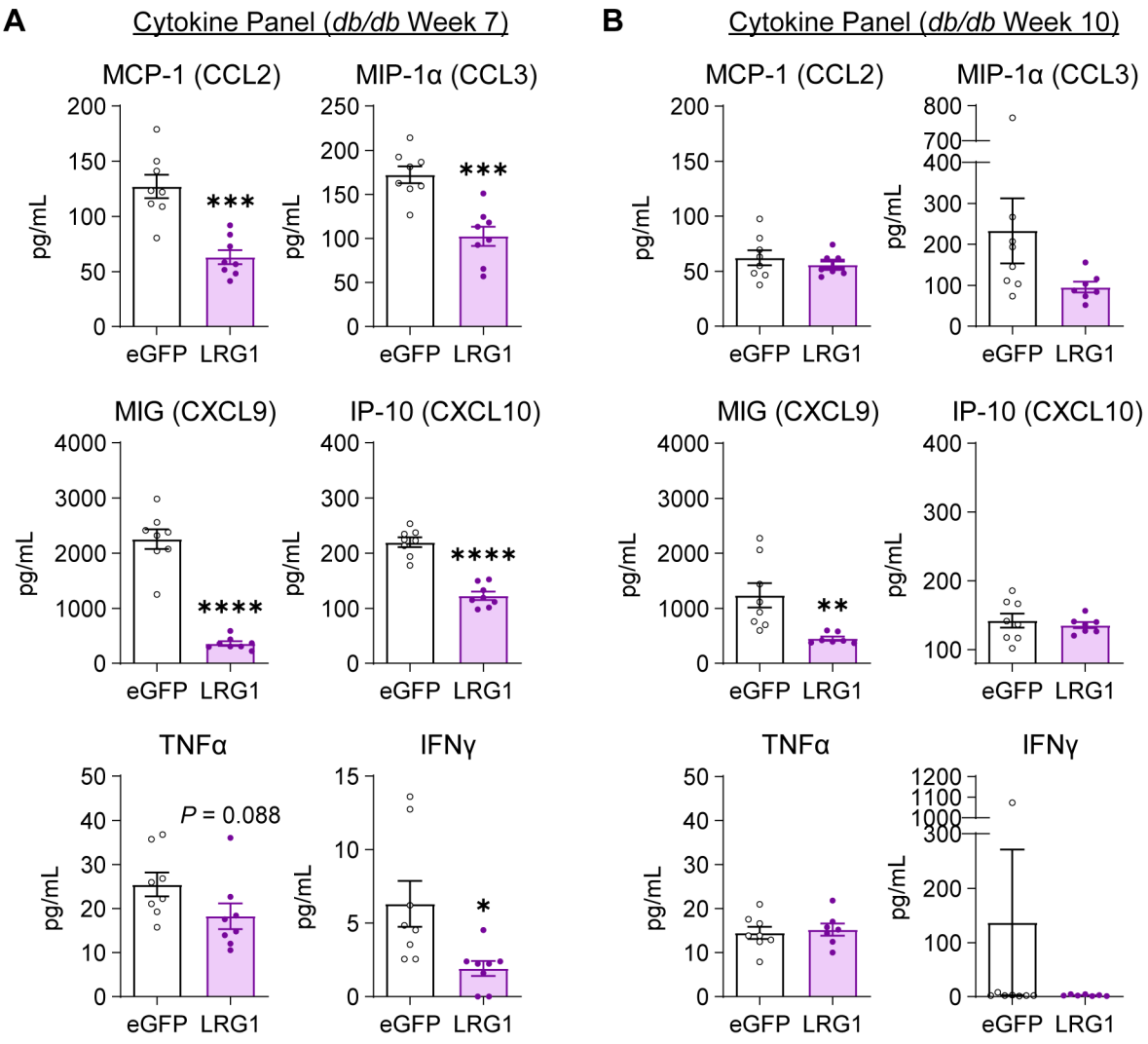

Figure 4.23. Reduction of serum chemokine/cytokine levels in LRG1-overexpressing *db/db* mice

(**A-B**) Quantification of serum levels of MCP-1, MIP-1α, MIG, IP-10, TNFα, and IFNγ in *db/db*-LRG1 and *db/db*-eGFP at 7 weeks (**A**) and 10 weeks (**B**) of age. Data are presented as mean ± SEM. **P* < 0.05, ***P* < 0.01, ****P* < 0.001, *****P* < 0.0001 from Welch's *t*-test. *n* = 7-8 per group.

4.8 LRG1 binds extracellular cytochrome *c* and blocks its pro-inflammatory effect on macrophages

LRG1 was the first protein characterized to contain what are now referred to as leucine-rich repeat (LRR) domains (Haupt & Baudner, 1977). Structural studies have demonstrated that LRR domains correspond to β-α structural units, forming a framework for protein-protein interactions (Kobe & Deisenhofer, 1994). Based on this information, we hypothesized that LRG1's immunomodulatory function is mediated by protein-protein interactions. One of LRG1's binding partners is cytochrome *c* (Cyt *c*), a mitochondrial protein (Cummings et al., 2006; Shirai et al., 2010). In addition to its role in the respiratory chain and intrinsic apoptosis pathway (Liu et al., 1996), Cyt *c* is released into the extracellular space following cell death (Jemmerson et al., 2002; Renz et al.,

2001) and mediates pro-inflammatory signals as a damage-associated molecular pattern (DAMP) (Eleftheriadis et al., 2016; Grazioli & Pugin, 2018). Adipocyte death in obesity is a key event promoting macrophage infiltration and WAT inflammation (Cinti et al., 2005). Hence, we explored whether extracellular Cyt *c* released by dead/dying adipocytes could be a mediator of macrophage recruitment/activation, and if LRG1 in turn modulates the pro-inflammatory action of Cyt *c*. We first sought to validate if LRG1 binds extracellular Cyt *c* in the circulation. We utilized the C-terminal FLAG-tag of overexpressed LRG1 and α-FLAG antibody-conjugated beads to co-immunoprecipitate (IP) LRG1-FL and its interacting partners. In the serum of *db/db* animals transduced with AAV-LRG1-FL, we were able to successfully co-IP both LRG1-FL and Cyt *c* from the serum, indicating that the two proteins indeed circulate as a complex (**Figure 4.24**).

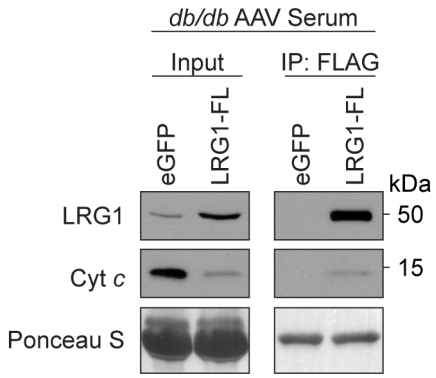

Figure 4.24. LRG1 binds Cyt *c* in serum
α-FLAG co-IP of C-terminally FLAG-tagged LRG1 and Cyt *c* from the serum of AAV-transduced *db/db* mice at 7 weeks of age. Ponceau S shown as loading control.

Elevated Cyt *c* levels in circulation have been observed in conditions involving cell death or inflammation, such as systemic inflammatory response syndrome (Adachi et al., 2004), myocardial infarction (Alleyne et al., 2001), response to chemotherapy (Barczyk et al., 2005), and apoptosis in liver disease (Ben-Ari et al., 2003). However, it is not known whether obesity, which is also known for its inflammatory state, is associated with increased serum Cyt *c* levels. Western blot analysis of serum revealed that Cyt *c* is increased in *db/db* animals compared to lean littermates (**Figure 4.25A**). Interestingly, extracellular Cyt *c* levels at 7 weeks of age trended higher than at 10 weeks of age (**Figure 4.25A**), correlating with the time point when LRG1 overexpression has a potent physiological effect. In B6 mice, HFD feeding led to increased Cyt *c* levels compared to chow-fed lean animals, and the serum levels correlated with the duration of HFD (**Figure 4.25B**).

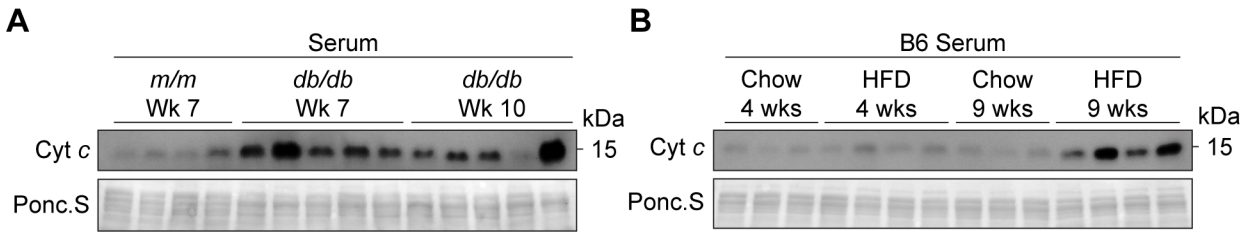

Figure 4.25. Obesity increases circulating Cyt *c*
(**A**) Western blot of Cyt *c* in the serum of *db/db* or littermate *m/m* mice at 7 and 10 weeks of age. (**B**) Western blot of Cyt *c* in the serum of B6 mice on standard chow or HFD for indicated weeks. HFD was started at 6 weeks of age. Ponceau S shown as loading control.

To test if dying adipocytes can contribute to circulating Cyt *c*, we subjected primary SubQ adipocytes to treatments that induce apoptosis or necrosis (**Figure 4.26**). In CM of SubQ adipocytes treated for 24 h with staurosporine (STS), a small molecule inducer of apoptosis, we detected a robust increase in Cyt *c* compared to vehicle controls (**Figure 4.26**). We also treated adipocytes to conditions that mimic obesity. CM collected from adipocytes incubated in hypoxic conditions or treated with TNFα also showed increased Cyt *c* compared to normoxic or vehicle controls, respectively (**Figure 4.26**).

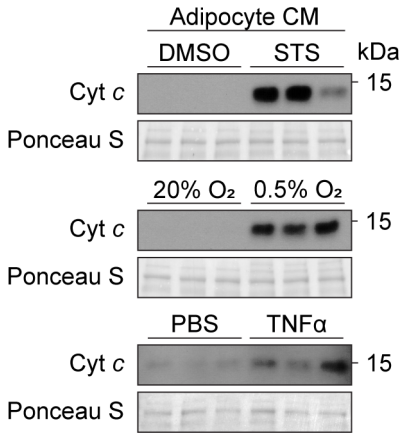

Figure 4.26. Adipocyte death leads to release of Cyt *c* to extracellular space
Western blot of Cyt *c* in the CM of primary SubQ adipocytes under conditions promoting cell death. SubQ cells were treated with 1 μM staurosporine (STS), a small molecule inducer of apoptosis, or DMSO vehicle for 24 h (top); placed in normoxic (20% O_2) or hypoxic (0.5% O_2) chambers for 24 h (middle); and treated with 100 ng/mL recombinant TNFα or PBS vehicle without insulin for 24 h (bottom). Ponceau S shown as loading control.

Extracellular Cyt *c* exerts a pro-inflammatory effect (Gouveia et al., 2017) by acting on the toll-like receptor 4 (TLR4)-mediated innate immune signaling pathway (Wenzel et al., 2019). During obesity-associated adipose tissue inflammation, circulating monocytes migrate into the adipose tissue and progressively polarize into a pro-inflammatory state (Oh et al., 2012). Therefore, we tested whether bone-marrow derived macrophages (BMDMs) also respond to extracellular Cyt *c* by upregulation of pro-inflammatory genes. Treating BMDMs with horse Cyt *c* led to >30-fold induction of lipopolysaccharide (LPS)-responsive pro-inflammatory genes such as *Il1b*, *Cxcl10*,

Il6, and *Nos2* ($P < 0.0001$), while pre-treatment of macrophages with a small molecule TLR4 inhibitor, TAK-242, prevented this induction (**Figure 4.27**). These data confirm that Cyt *c* in the extracellular space acts as a DAMP that activates innate immune signaling and polarizes macrophages into a more pro-inflammatory state.

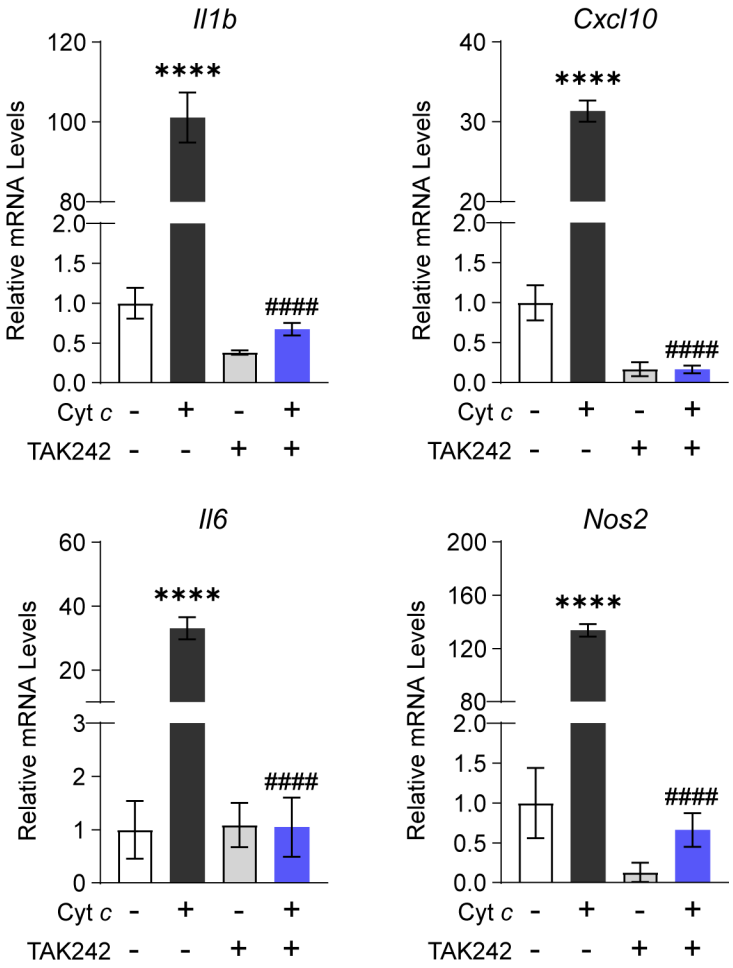

Figure 4.27. Cyt *c* activates macrophages via TLR4 innate immune signaling
Relative mRNA levels of a panel of pro-inflammatory genes in BMDMs in response to 30 µg/mL equine Cyt *c* or 10 µM TAK-242, a TLR4 inhibitor. BMDMs were treated with Cyt *c* or PBS for 6 h following 1 h pre-incubation with TAK-242 or DMSO. Data are presented as mean ± SEM. Tukey post hoc test results from two-way ANOVA are indicated. ****$P < 0.0001$, Cyt *c* vs. PBS. ####$P < 0.0001$, Cyt *c*-TAK-242 vs. Cyt *c*. $n = 3$ per group.

We then explored how co-treatment of Cyt *c* and recombinant human LRG1 (rhLRG1) affects Cyt *c*'s pro-inflammatory effect on macrophages. Prior to treatment, media containing Cyt *c*, rhLRG1, or both were incubated for one hour to allow protein-protein interactions to occur. Compared to single treatment, co-treatment with rhLRG1 significantly dampened Cyt *c*-mediated induction of *Il1b* ($P < 0.0001$), *Cxcl10* ($P = 0.024$), and *Il6* ($P = 0.0008$) (**Figure 4.28**). We noticed that *Nos2* was significantly induced with rhLRG1 treatment by 2.63-fold ($P = 0.0063$), and Cyt *c*-mediated induction of *Nos2* was not affected by co-treatment with rhLRG1 (**Figure 4.28**).

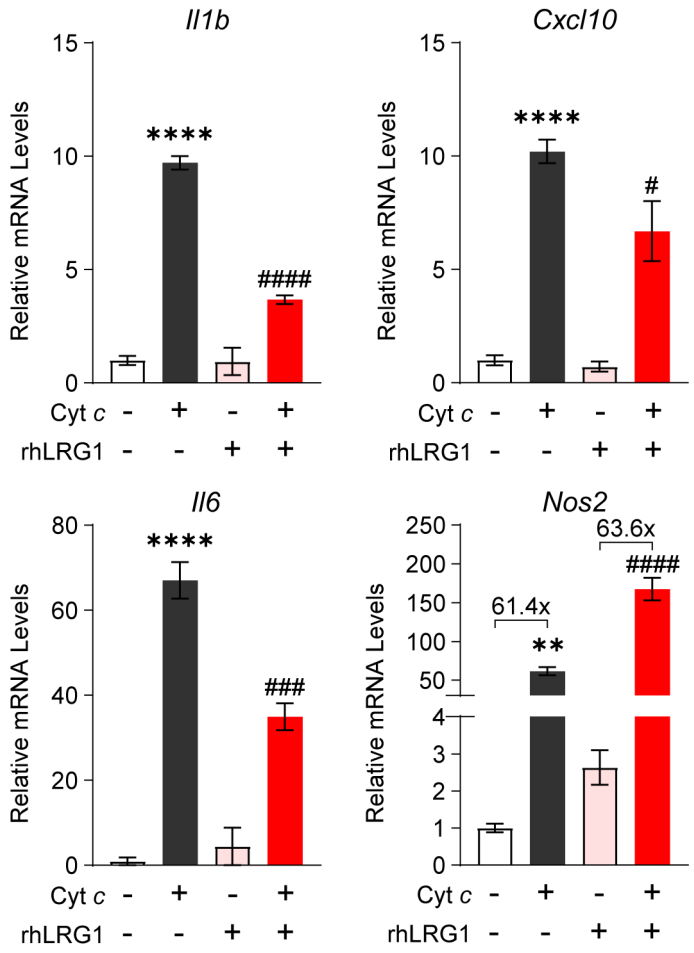

Figure 4.28. LRG1 dampens pro-inflammatory activity of Cyt *c*
Relative mRNA levels of a panel of pro-inflammatory genes in BMDMs in response to 20 µg/mL equine Cyt *c* and 50 µg/mL recombinant human LRG1. Indicated reagents or PBS were rotated for 1 h at RT prior to BMDM treatment for 6 h. Data are presented as mean ± SEM. Tukey post hoc test results from two-way ANOVA are indicated. ***P* < 0.01, *****P* < 0.0001, Cyt *c* vs. PBS. #*P* < 0.05, ###*P* < 0.001, ####*P* < 0.0001, Cyt *c*-rhLRG1 vs. Cyt *c*. *n* = 3-4 per group.

Interestingly, pre-treatment of BMDMs with rhLRG1 for one hour followed by addition of Cyt *c* did not attenuate the latter's pro-inflammatory effect, suggesting that Cyt *c*-LRG1 complex formation is needed for LRG1's modulatory effect (**Figure 4.29**). Taken together, these results demonstrated that LRG1 can modulate many of the pro-inflammatory gene expression responses induced by Cyt *c*, while other genes such as *Nos2* can still be induced by Cyt *c* despite the presence of LRG1.

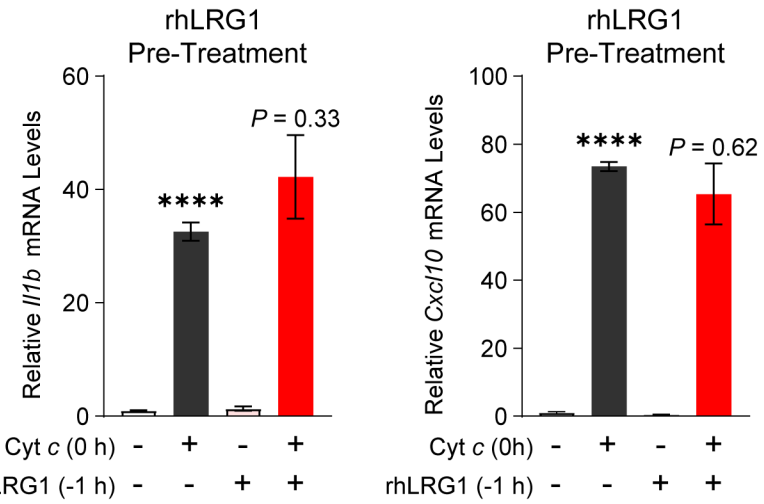

Figure 4.29. LRG1 pre-treatment does not affect Cyt *c*'s pro-inflammatory activity
Relative *Il1b* and *Cxcl10* mRNA levels in BMDMs in response to 20 µg/mL equine Cyt *c* with or without 1 h pre-treatment of 50 µg/mL recombinant human LRG1. Data are presented as mean ± SEM. Tukey post hoc test results from two-way ANOVA are indicated. ****$P < 0.0001$, Cyt *c* vs. PBS. Numerical *P*-values, Cyt *c*-rhLRG1 vs. Cyt *c*. $n = 3$ per group.

Cyt *c* is a small (12.5 kDa), globular protein with a short half-life in circulation (Radhakrishnan et al., 2007). Small proteins such as Cyt *c* are expected to be rapidly cleared from circulation via glomerular filtration in the kidney (Tojo and Endou, 1992). With the tight binding interaction between LRG1 and Cyt *c*, it is expected that much of extracellular Cyt *c* circulates as a complex with LRG1. LRG1 has an apparent molecular weight of around 45 kDa, which is larger than the size cutoff for glomerular filtration. Therefore, we sought to assess whether this interaction affects Cyt *c* clearance. We performed retroorbital injection of equine Cyt *c* into WT and LRG1-KO mice and collected blood at various time points, from 5 minutes to 6 hours post-injection. Plasma western blot showed that LRG1-KO animals almost completely cleared Cyt *c* by 2 hours, whereas in WT animals, an initial decrease in Cyt *c* signal was followed by nearly constant levels between 1 and 4 hours post injection (**Figure 4.30**).

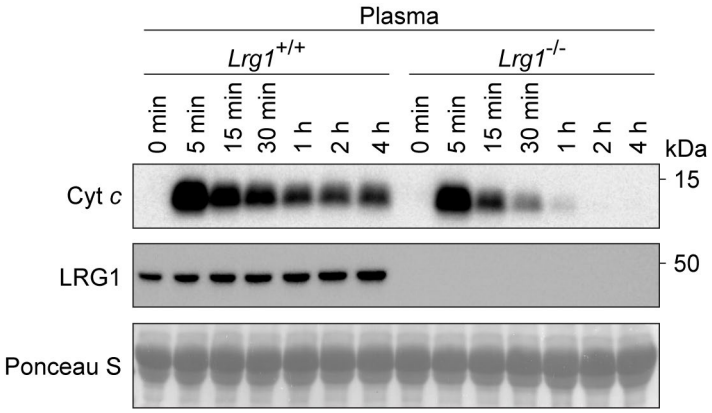

Figure 4.30. LRG1-KO mice demonstrate enhanced clearance of extracellular Cyt *c*
Representative western blot of Cyt *c* in plasma of LRG1-KO and WT littermate male mice following 40 mg/kg retroorbital injection of equine Cyt *c*.

For a more quantitative analysis, we quantified the intensities from Cyt *c* immunoblots. Fitting one phase decay functions to relative Cyt *c* intensities showed that while both WT and LRG1-KO curves have similar half lives (WT: 16.10 min vs. KO: 17.32 min), the WT trace plateaus at 0.2791, whereas the LRG1-KO curve approaches zero (**Figure 4.31**). Of note, while the 95% confidence interval for the estimated half lives overlapped between the two genotypes, interval for the plateau values did not (**Table 4.1**).

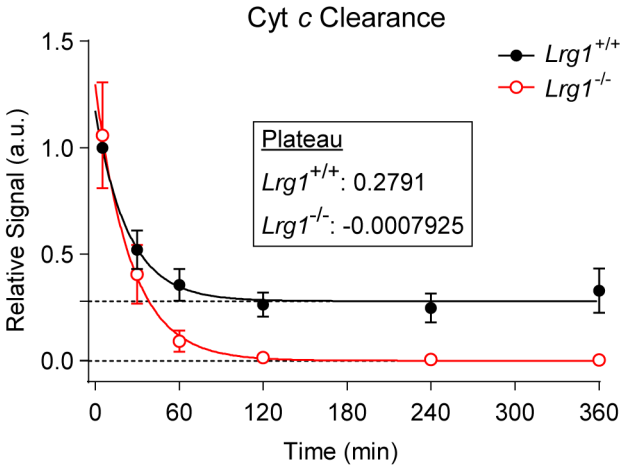

Figure 4.31. Quantified Cyt *c* clearance rates between LRG1-KO and WT
Relative quantification of Cyt *c* intensities in plasma of LRG1-KO and WT littermate male mice following 40 mg/kg retroorbital injection of equine Cyt *c*. Fitted one-phase decay curves and estimated values for the plateau are shown. Data are presented as mean ± SEM. $n = 4$ per group.

Table 4.1. Summary of least squares regression fit of relative Cyt *c* intensities with one-phase decay function

$Y = \text{Plateau} + (Y0 - \text{Plateau})e^{-K*X}$

	WT	LRG1-KO
Best-fit values		
Y0	1.173	1.297
Plateau	0.2791	-0.00079
K	0.04306	0.04002
Half Life	16.1	17.32
Tau	23.23	24.99
Span	0.8936	1.298
95% CI (profile likelihood)		
Y0	0.9578 to 1.454	0.9730 to 1.699
Plateau	0.1925 to 0.3608	-0.1380 to 0.1278
K	0.02460 to 0.08768	0.02225 to 0.08035
Half Life	7.905 to 28.18	8.626 to 31.16
Tau	11.40 to 40.65	12.44 to 44.95
Goodness of Fit		
Degrees of Freedom	21	21
R squared	0.7971	0.7775
Sum of Squares	0.4115	1.006
Sy.x	0.14	0.2189
Constraints		
K	$K > 0$	$K > 0$
Number of points		
# of *X* values	24	24
# *Y* values analyzed	24	24

Concomitantly, appearance of Cyt *c* in the urine was observed as soon as 30 minutes after the injection, demonstrating that clearance of excess Cyt *c* is indeed through the kidneys (**Figure 4.32**). Urine Ponceau S staining showed that detected proteins were all below 25 kDa, the apparent size limit for urinary excretion of proteins (**Figure 4.32**). We reason that in LRG1-KO animals, Cyt *c* circulates as an unbound, free form that can be rapidly excreted by glomerular filtration, whereas the presence of LRG1 in WT animals prevents a portion of Cyt *c* from excretion due to formation of a complex larger than the size cutoff for glomerular filtration. This provides further evidence that extracellular Cyt *c* circulates in a complex with LRG1. Taken together, these data directly demonstrate that Cyt *c* is a native ligand of LRG1.

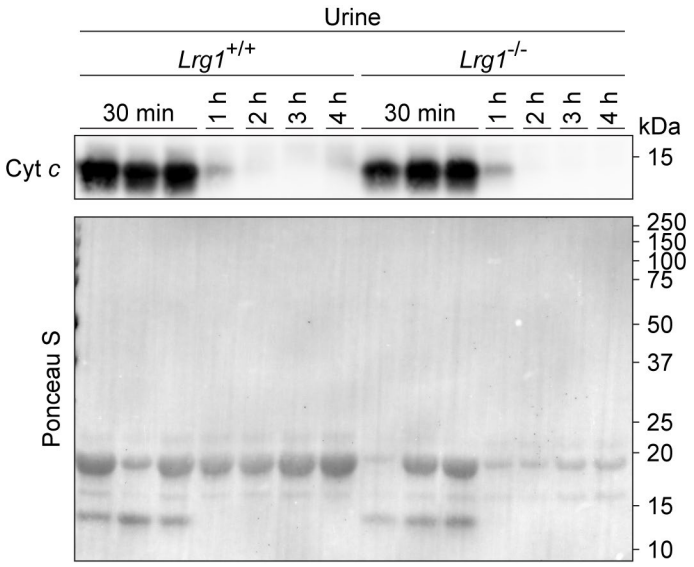

Figure 4.32. Excess circulating Cyt *c* is excreted by the urine
Urine Cyt *c* western blot and Ponceau S stain of urinary proteins from LRG1-KO and WT littermate male mice following 40 mg/kg retroorbital injection of equine Cyt *c*.

4.9 Discussion

Here, we sought to identify novel adipose-derived circulating factors that can regulate whole-body metabolism via crosstalk with distant or neighboring cells and tissues. To that end, we utilized profiling studies from Chapter 2. Specifically, we looked at the intersection between proteins identified in the adipocyte CM and in the nascent serum proteome of mice. To ensure that adipocytes are meaningful contributors to the circulating levels of our candidates, we employed results from the bioinformatic analysis in section 2.3.3 and selected for proteins with percentage adipose enrichment score above 80%. The intersection of all three criteria contained ten proteins, including classical adipokines such as adiponectin (Wang and Scherer, 2016), adipsin (Lo et al., 2014; Gómez-Banoy et al., 2019), and RBP4 (Yang et al., 2005), all of which have important roles in whole-body energy homeostasis. LRG1 shares a similar expression signature with these adipokines, but its metabolic function has thus far not been characterized. We demonstrate, using two types of viral vectors and two different mouse models of obesity, that LRG1 overexpression leads to a significant improvement in glucose homeostasis by promoting insulin sensitization. This insulin-sensitizing effect in LRG1 gain of function is associated with a dramatic reduction in systemic inflammation and with LRG1's ability to bind Cyt *c* and modulate its pro-inflammatory effect as a DAMP (**Figure 4.33**).

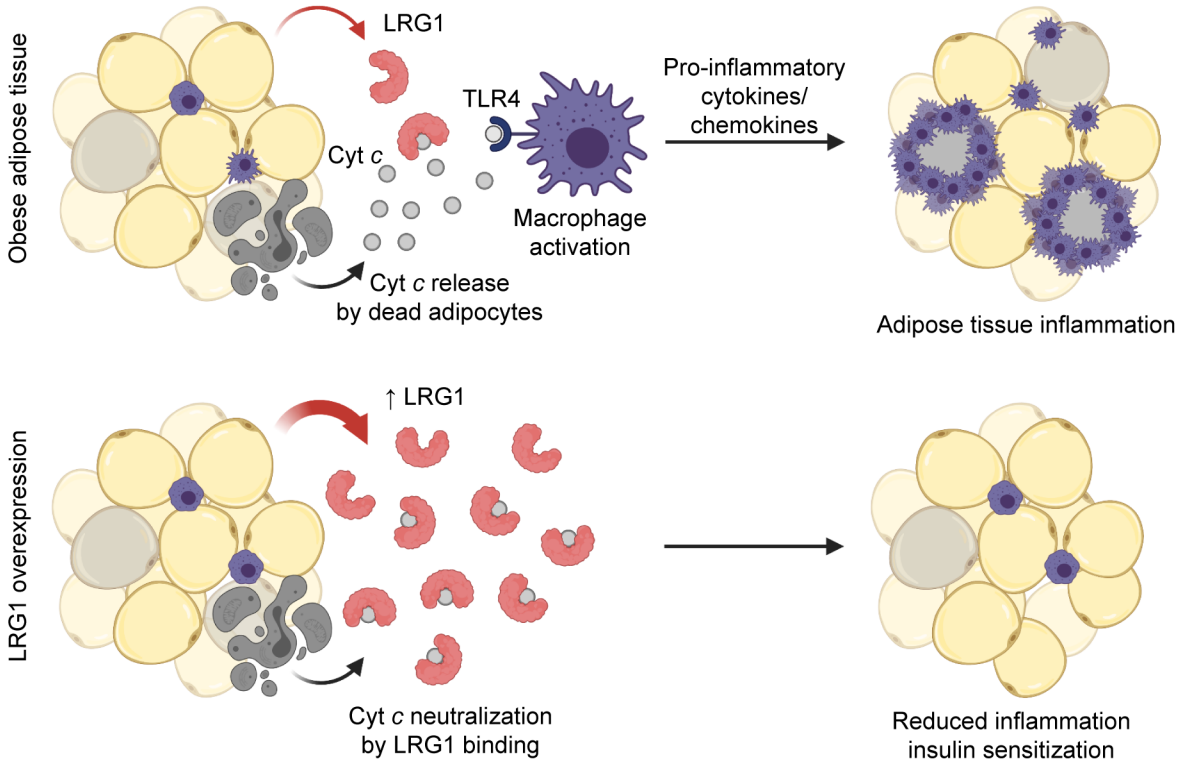

Figure 4.33. Proposed mechanism of LRG1 action

Validating the search strategy, we have confirmed that adipose tissues at various anatomical locations all express *Lrg1*. Among the tissues tested, the only other major *Lrg1*-expressing tissue was the liver. We observe robust enrichment of *Lrg1* mRNA expression in mature adipocytes over SVF within adipose tissue and LRG1 protein secretion from differentiated primary adipocytes. Although the liver also expresses high levels of *Lrg1*, we observe that obese animals have higher circulating levels of LRG1 when iWAT is the only tissue that demonstrates induction of *Lrg1* mRNA. While not definitive, this strongly suggests that adipose tissue is a significant contributor to circulating LRG1.

We have demonstrated with *in vivo* mouse models of obesity that LRG1 overexpression leads to insulin sensitization and suppression of systemic inflammation. Adipose tissue expansion in mice is characterized by periods of rapid adipocyte turnover, during which there is a sharp increase in adipocyte death and monocyte/macrophage accumulation (Rosen and Spiegelman, 2014; Weisberg et al., 2003). In B6 eWAT, adipocyte death and CLS formation peak around 12-16 weeks on HFD (Strissel et al., 2007), which corresponds to when a parallel surge in fasting blood glucose levels is observed. In *db/db* mice, the remodeling seems to be initiated earlier, as CLS in WAT emerge at 7 weeks of age, and chemokine/cytokine expression and circulating levels are more highly induced at week 7 than week 10. Periods when LRG1's insulin-sensitizing and anti-inflammatory effects are particularly effective coincide with these times of rapid adipocyte death and turnover. As inflammation is a key mechanistic link between obesity and insulin resistance (Saltiel & Olefsky, 2017), these findings strongly suggest LRG1 promotes insulin sensitization via modulation of inflammation during adipose tissue remodeling.

Soon after extracellular Cyt *c* was recognized as a marker of cell death, LRG1 was identified as a serum factor that binds Cyt *c* (Cummings et al., 2006). The biochemical interaction between LRG1 and Cyt *c* has been well characterized (Codina et al., 2010; Shirai et al., 2010), but the biological context and function of this interaction have been relatively understudied. We propose that LRG1 functions as a buffer against deleterious effects of extracellular Cyt *c* released from dying/dead cells. During obesity-driven adipose tissue remodeling, a rapid increase in adipocyte death contributes to increased circulating Cyt *c*, which could be an important pro-inflammatory signal triggering monocyte/macrophage recruitment. The pro-inflammatory setting of obesity also induces LRG1 in other adipocytes, and this increase in circulating LRG1 helps modulate inflammation by directly binding Cyt *c*. Of note, both TLR4 and LRG1 contain LRR domains, so the Cyt *c*-neutralizing effect by LRG1 could involve steric interference as the two proteins compete for binding Cyt *c*. While the current study focused on LRG1's effect on adipose tissue, it is important to emphasize that LRG1-mediated anti-inflammatory effects were systemic, as observed by lower circulating cytokine levels and decrease in liver inflammatory foci in LRG1-overexpressing *db/db* mice. Similar mechanisms involving an LRG1-Cyt *c* interaction may be at play, as hepatocyte apoptosis contributes to progression of NASH (non-alcoholic steatohepatitis) in NAFLD (Feldstein et al., 2003). As neither DIO nor chow-fed *db/db* mice are the most suitable model to study NAFLD, further investigation with appropriate mouse models may uncover a hepatoprotective role for LRG1 in NAFLD.

The fact that LRG1-KO mice demonstrate enhanced Cyt *c* clearance provides further evidence that LRG1 binds and forms a complex with Cyt *c* in circulation, and highlights the need to check LRG1 levels in future studies utilizing extracellular Cyt *c* as a biomarker. We have shown that excess extracellular Cyt *c* is predominantly cleared via renal excretion. Similar serum Cyt *c* half-lives between WT and LRG1-KO suggest LRG1 loss of function does not affect kidney function. Divergence in Cyt *c* clearance profiles occurs towards the plateau, and we believe this difference represents the portion of Cyt *c* that stays bound to LRG1 in WT animals. It is unclear how this complex is ultimately cleared, but this may involve a different mechanism such as the reticuloendothelial system. Enhanced clearance of Cyt *c* observed in LRG1-KO animals may also provide an explanation for the relative dearth of effect of LRG1 loss of function on metabolic health, other than worsened fasting glucose levels. Inflammation in obesity, especially in B6 DIO mice, is chronic and relatively low grade, so enhanced clearance of Cyt *c* may be sufficient to counteract Cyt *c* release and protect from its deleterious effects. It is possible that the effect of LRG1 loss of function may be more pronounced in conditions that involve more acute or high-grade inflammation.

Multiple biomarker studies in humans have shown that increased LRG1 is associated with not only obesity (Pek et al., 2018) but also other conditions involving cell death and inflammation, such as appendicitis (Kentsis et al., 2010, 2012), solid tumors (Belczacka et al., 2019) and autoimmune diseases (Naka and Fujimoto 2018). Our study suggests that induction of LRG1 in these settings could be a compensatory mechanism to modulate inflammation. However, LRG1 has also been shown to perform other functions, such as induction of angiogenesis via TGF-β signaling (Hong et al., 2019; Wang et al., 2013) or direct inhibition of apoptosis (Codina et al., 2010; Jemmerson et al., 2021). While our work focused on LRG1's metabolic and immunomodulatory function in relation to its Cyt *c* binding activity, it is likely that LRG1 functions in a multi-faceted role in different contexts.

CHAPTER 5. Conclusion

Advances in transcriptomic and proteomic profiling strategies have greatly expanded our understanding of the adipose secretome. However, much remains to be uncovered, especially considering the unique set of technical challenges involved in secretome analysis. In addition, compared to the rapid advances made in these profiling efforts, our understanding of the functional impact of these factors on whole-body metabolism is relatively lacking.

Here, we employed a chemoproteomic technology called BONCAT to profile the adipose secretome that is more physiologically relevant. We provide a comprehensive picture of the adipose secretome across the three major types of adipocytes as well as its predicted contribution to the nascent serum proteome. From these data, we identified a novel protein called C11orf54, whose expression is enriched in brown and beige adipocytes and induced by cold exposure. C11orf54 does not contain a signal peptide and is not predicted to be secreted based on *in silico* analysis. However, we have validated both *in vitro* and *in vivo* that it is a *bona fide* secreted factor, demonstrating the value of directly measuring proteins in CM. Moreover, functional studies with a genetic knockout of its secreted isoform demonstrate that C11orf54 may regulate total body energy expenditure rate. We also identified a novel adipokine called LRG1 with previously unknown metabolic function and discovered its role as an insulin sensitizer and suppressor of inflammation. LRG1's *in vivo* function is associated with binding interaction with extracellular Cyt *c*, and mechanistic studies on this interaction shed light on molecular players involved in adipocyte-macrophage interaction during adipose tissue expansion and remodeling.

Future work on C11orf54 will focus on determining the physiological basis of its ability as a secreted factor to regulate whole-body energy expenditure. Elucidation of its molecular function as a putative enzyme will help corroborate these mechanistic studies. Our preliminary results with deconvolution microscopy on fixed primary adipocytes suggest that C11orf54's subcellular location may change dynamically with acute norepinephrine treatment. Future studies with live-cell imaging will validate these findings. We are also exploring whether acute sympathetic stimulus regulates the secretion of C11orf54. Metabolomic analysis of HEK293 cell lysates overexpressing isoform 1 of C11orf54 demonstrated decreased levels of myo-inositol and kynurenic acid, and serum metabolomic analysis of C11orf54 isoform 1 KO animals also showed decreased levels of the same metabolites in circulation compared to WT littermates. Deciphering the molecular mechanisms underlying these changes in metabolite levels will potentially shed light on the enzymatic function of C11orf54.

The causative agent of adipose tissue inflammation in the setting of obesity is yet to be identified. The binding interaction between LRG1 and extracellular Cyt *c* that leads to mitigation of the latter's pro-inflammatory activity highlights Cyt *c* as a potential trigger for obesity-mediated inflammation. LRG1 or targeting extracellular Cyt *c* could be an attractive therapeutic approach for treatment of not only obesity but a variety of inflammatory conditions. Specifically, development of neutralizing antibodies against extracellular Cyt c could be utilized to uncouple obesity and its complications.

Finally, further development and optimization of technologies that enable analysis of cell type-specific proteomes in the blood will greatly expand our understanding of the role of adipose tissue endocrine function on whole-body energy homeostasis. We believe cell type-specific BONCAT

(Alvarez-Castelao et al., 2017) and TurboID (Branon et al., 2018) will complement each other in providing in-depth description of adipose tissues' contribution to circulating proteins. Such techniques will allow direct identification and quantification of adipose-derived proteins and their circulating levels under various physiological or pathophysiological conditions such as obesity and cold exposure. These methods will therefore directly demonstrate the extent of endocrine dysfunction that occurs in obesity, as well as changes in secretion profiles in cold exposure that can potentially highlight brown fat-derived mediators that contribute to systemic metabolic benefits of BAT activation or useful biomarkers of BAT activity. We believe new opportunities to treat obesity and its sequelae can be opened up by such efforts to uncover and characterize novel secreted factors from adipocytes.

CHAPTER 6. Materials and methods

6.1 Materials

6.1.1 Animals

C57BL/6J mice were purchased from Jackson Laboratories. C57BLKS-*Lepr*^{db} homozygote males and C57BLKS-*Dock*^{7m} homozygote males were purchased from Jackson Laboratories. LRG1-KO (*Lrg1*$^{-/-}$) and C11orf54Iso1-KO lines were generated in C57BL/6J background by the CRISPR and Gene Editing Center at the Rockefeller University and backcrossed with C57BL/6J mice for at least five generations to minimize off-target effects. Cohorts of LRG1-KO or C11orf54Iso1-KO and corresponding WT littermates for characterization studies were obtained by intercrossing male and female heterozygotes. Animals were maintained at the Rockefeller University Comparative Biosciences Center, housed at 23ºC and maintained at 12 h light:dark cycles. The animals were group-housed with ad libitum access to food and water except during metabolic characterization studies. C57BL/6J mice were fed standard chow diet (LabDiet 5053), and where specified, started on 60% high fat diet (HFD, Research Diets D12492) feeding at 6 or 8 weeks of age. C57BLKS-*Lepr*^{db} and C57BLKS-*Dock*^{7m} were fed standard chow diet. Virus injections were performed in designated ABSL-2 housing rooms and the transduced mice were quarantined for 72 hours post-injection before transferred to regular housing rooms. Experiments involving adenoviral and AAV8 vectors were performed in accordance with the institutional ABSL-2 guidelines. All animal studies were performed in accordance with the institutional guidelines of the Rockefeller University Institutional Animal Care and Use Committee (IACUC).

6.1.2 Cells

Mouse primary stromal vascular fraction (SVF) cells were obtained from adipose tissues of 6- to 8-week-old male mice by collagenase digestion and plated on collagen I-coated dishes. SVF cells from epididymal white adipose tissue (eWAT) were grown in ITS media containing 1.5:1 mixture of low-glucose DMEM:MCDB201 supplemented with 2% FBS (Gemini), 1% ITS premix (Corning), 0.1 mM L-ascorbic acid 2-phosphate (Sigma), 10 ng/mL bFGF (Thermo), 0.5% penicillin/streptomycin (P/S, Gibco), and 0.2% primocin (InvivoGen). SVF cells from inguinal white adipose tissue (iWAT) and interscapular brown adipose tissue (BAT) were grown in DMEM/F-12 GlutaMAX medium (Gibco) containing 10% FBS and 1% P/S. Once grown to confluence, differentiation and maintenance of primary adipocytes across cell types were done using DMEM/F-12 GlutaMAX medium containing 10% FBS and 1% P/S. eWAT and iWAT SVF cells were induced to differentiate with an adipogenic cocktail (0.5 mM IBMX, 1 μM dexamethasone, 1 μM rosiglitazone, and 850 nM insulin) for the first 2 days, followed by 2 days of 1 μM rosiglitazone and 850 nM insulin, after which the cells were maintained in 850 nM insulin for additional 2-4 days. SVF cells from BAT were differentiated as above but with 17 nM insulin. Experiments with primary adipocytes were performed between days 6 and 8 of differentiation. All cultured primary adipocytes were checked for lipid accumulation under a phase-contrast microscope before studies. Primary SVF and adipocytes were maintained at 37ºC with 10% CO_2.

Bone marrow-derived macrophages (BMDMs) were obtained from 8- to 10-week-old males. Femurs and tibias were dissected, cleaned, and sterilized with ethanol before flushed of bone marrow cells, which were plated onto petri dishes. Bone marrow cells were differentiated in RPMI-1640 medium (Gibco) supplemented with 20% heat-inactivated FBS (Sigma), 1% P/S, and 100

ng/mL M-CSF (Biolegend) for 6-7 days, changing media every 2-3 days. Differentiated BMDMs were washed, trypsinized, and plated onto TC-treated culture plates for overnight before studies were performed. Experiments with BMDMs were performed between days 6 and 7 of differentiation. BMDMs were differentiated and maintained at 37ºC with 5% CO_2.

HEK293A cells were purchased from Invitrogen and grown using 4.5 g/L glucose DMEM (Gibco) supplemented with 10% FBS and 1% P/S at 37ºC with 5% CO_2. Cells with passage number under 20 were used for adenovirus production. Cells were validated to be mycoplasma free.

6.2 Method details

6.2.1 Proteomic analysis of BONCAT samples

Conditioned medium generation

On day 6 of differentiation, primary adipocytes on collagen-coated 6-well plates were washed twice with warm PBS and pulsed with 1 mL/well of Met-free DMEM containing 10% dialyzed FBS, 1% P/S, 17 nM or 850 nM insulin, and either 0.1 mM AHA or 0.1 mM Met. Following 24 h incubation at 37ºC with 10% CO_2, conditioned media (CM) from 6 wells (1 plate) were collected and pooled, filtered through a 0.22 µm PES membrane syringe filter unit, and supplemented with ½ tabs of EDTA-free cOmplete mini protease inhibitor cocktail (Roche) and PhosSTOP (Roche). CM was concentrated using a 3 kDa centrifugal filter unit (Millipore).

AHA administration and serum collection

Mice were injected with 0.1 g/kg/day AHA or PBS IP for 2 consecutive days and sacrificed 24 hours following the second injection. Following decapitation, truncal blood was collected, allowed to clot for 15 min at room temperature, and centrifuged at 2000×g for 15 min at 4ºC to collect serum.

In-gel fluorescence analysis

Concentrated CM or serum was dialyzed with phosphate-buffered RIPA (10 mM phosphate buffer pH 7.2, 1% Triton X-100, 0.1% Na deoxycholate, 0.1% SDS, 140 mM NaCl) supplemented with EDTA-free cOmplete mini protease inhibitor cocktail (Roche) and PhosSTOP (Roche) using a 3 kDa centrifugal filter unit (Millipore) and protein concentration was determined using Pierce BCA Protein Assay Kit (Thermo Scientific) using a dilution series of bovine serum albumin as protein standards. Copper(I)-catalyzed azide-alkyne cycloaddition reaction with TAMRA-alkyne (Invitrogen) was performed by mixing 200 µg of CM proteins with 0.1 mM TAMRA-alkyne, 1 mM TCEP, 0.1 mM TBTA, and 1 mM of $CuSO_4$ in phosphate-buffered RIPA and rotated end-over-end for 1 h at room temperature under protection from light. Following methanol/chloroform precipitation, the dried protein pellet was dissolved in Laemmli loading buffer. Following polyacrylamide gel electrophoresis, the gel was briefly washed with distilled H_2O and imaged with a Typhoon 5400 imager (GE Healthcare) using 532 nm excitation and a 580 nm detection filter.

Enrichment of labeled proteins

Azide-labeled nascent protein in the concentrated CM was enriched using Click-iT™ Protein Enrichment Kit (Invitrogen). Serum was diluted 1:1 with the lysis buffer provided with the kit and subjected to enrichment. Enrichment and resin wash was performed following the protocol from Eichelbaum and Krijgsveld (2014).

On-bead digestion
Extensively washed beads were incubated with Lys-C endopeptidase (Wako) in 4 M urea and 0.14 M NH_4HCO_3 by shaking at 1400 rpm for 6 h at room temperature. The resin mixture was further digested by adding trypsin (Promega) in 2 M urea and 0.14 M NH_4HCO_3 and incubated by shaking at 1400 rpm overnight at room temperature. The following day, the digestion reaction was quenched by adding trifluoroacetic acid.

LC-MS/MS
Tryptic peptides were desalted (Rappsilber et al., 2007) and separated by reverse phase nano-LC-MS/MS (column: 12cm/75um C18 built-in-emitter column, Nikkyo Technos Co., Ltd. Japan, EasyLC 1200, Thermo Scientific) using a 70-minute analytical gradient, increasing from 2% B/98% A to 38%B/62%A (A: 0.1% formic acid, B: 80% Acetonitrile/0.1% formic acid) at 300 nL/min. The mass spectrometer (Fusion Lumos, Thermo Scientific) was operated in high/high mode (120,000 and 30,000 for MS1 and MS2, respectively). Auto Gain Control was set at 50,000 for MS2. MS1 scan range was set to m/z 375-1500 and m/z 110 was set as lowest recorded mass in MS2. One-point lock mass calibration was used. All data were quantified and searched against a Uniprot mouse database using MaxQuant (v. v. 1.6.0.13) (Cox et al., 2014). Oxidation of methionine and protein N-terminal acetylation were allowed as variable modifications, cysteine carbamidomethyl was set as a fixed modification, and two missed cleavages were allowed. The "match between runs" option was enabled, and false discovery rates for proteins and peptides were set to 1%. Protein abundances measured using label free quantitation (Tyanova et al., 2016).

Proteomic data analysis
Proteomic datasets were analyzed using Perseus v1.6.14.0 (Tyanova et al., 2016). Of the detected proteins, those flagged as reverse, only identified by site, and potential contaminants were excluded from the analysis. For quantitative analysis, LFQ or iBAQ intensities were employed as indicated; LFQ intensities were used for comparisons across samples, while iBAQ intensities were used to compare abundances across different proteins. Imputation of undetected data points for Log_2(LFQ) intensities was performed by assigning values from a normal distribution of 0.3 width and 1.8 down shift. Principal component analysis (PCA) was performed with imputed Log_2(LFQ) intensities. Scatterplot representation of Log_2(LFQ) intensities was generated without imputation. Differentially secreted proteins were identified with ANOVA using permutation-based FDR, with FDR set at 0.01 and number of randomizations at 250.

6.2.2 Other methods

GO cell component analysis
Gene symbols from detected proteins were submitted to Retrieve/ID mapping tool on the UniProt website (https://uniprot.org). List of genes that are annotated with the following gene ontology cell component terms were obtained: extracellular region (5576), extracellular space (5615), extracellular matrix (31012), plasma membrane (5886), cytosol (5829), nucleus (5634), mitochondrion (5739), endoplasmic reticulum (5783), and Golgi apparatus (5794).

Secretion prediction analysis
UniProt accession IDs of the detected proteins were submitted to Retrieve/ID mapping tool on the UniProt website (https://uniprot.org) to obtain the FASTA sequences, which were used as inputs

for various secretion prediction algorithms using the web-based query system. We defined classically secreted proteins as having SignalP5.0 score > 0.5 and 0 or 1 predicted transmembrane domains by TMHMM2.0. Subcellular localization prediction analysis was performed using DeepLoc1.0 and searched for proteins whose predicted location is extracellular. PredGPI specificity score > 99% was used as the threshold to determine if a protein is expected to be GPI-anchored. Finally, proteins with SecretomeP2.0 score > 0.6 and SignalP5.0 score ≤ 0.5 were considered non-classically secreted.

Cluster analysis and functional annotation

Hierarchical clustering was performed on z-score-transformed Log_2(LFQ) values using the complete-linkage method and split into 4 clusters by dendrogram. DAVID v6.8 was used to generate functional annotation of clusters (Huang et al., 2009a, 2009b). List of genes encoding the proteins of each of the 4 clusters were compared to a background gene list of total detected proteins in the proteomic dataset. Per cluster, top 4 overrepresented pathways in the gene ontology biological process terms were reported.

Adipose tissue enrichment analysis

To identify candidate genes enriched within brown and white adipose relative other tissue types as well to each other we used the BioGPS datasets (Su et al., 2004). The Mouse GNF1M Gene Atlas datasets (GSE1133) were downloaded from BioGPS portal (Su et al., 2004) and imported into Limma Bioconductor package (Ritchie et al., 2015) for Log2 transformation and differential expression analysis. All pair-wise comparisons for both brown adipose and white adipose tissues against all other tissue types were performed using limma as well as the direct comparison between brown and white adipose tissues. Genes with a Log2 fold change greater than 4 and a Benjamini-Hochberg-corrected FDR of 0.05 within pair-wise comparisons were considered significantly enriched. Genes were further scored by the total number of pair-wise comparisons where genes were found to be enriched in both adipose tissues, brown adipose tissue or white adipose tissue compared to other tissues in the tissue atlas.

RNA isolation, cDNA synthesis, and RT-qPCR

Total RNA was extracted from cultured cells using RLT buffer (Qiagen) and from tissues using TRIzol (Invitrogen) and purified using RNeasy Mini Kit (Qiagen). cDNA was synthesized from 1 µg of RNA using the High-Capacity cDNA Reverse Transcription Kit (Applied Biosciences). Power SYBR Green (Life Technologies) was used for RT-qPCR reactions performed with QuantStudio 6 Flex Real-Time PCR System (Thermo Scientific) in a 384 well format. Relative fold changes of mRNA levels were calculated using the ΔΔCT method with 18S rRNA as loading control.

Adipose tissue fractionation

Adipose tissues from 8-week-old C57BL/6J WT male mice were dissected and minced. eWAT and iWAT were digested in a buffer containing 10 mg/mL collagenase D (Roche), 2.4 mg/mL Dispase II (Roche), and 10 mM $CaCl_2$ in PBS. For BAT, 2x BAT digestion buffer containing 125 mM NaCl, 5 mM KCl, 1.3 mM $CaCl_2$, 5 mM glucose, 1% P/S, and 4% BSA was prepared, which was diluted 1:1 with PBS and used to dissolve collagenase B (Roche) at a final concentration of 1.5 mg/mL. Following collagenase digestion of the tissues in a 37ºC water bath, the mature adipocyte fraction was separated from the SVF pellet by centrifugation at 500×g for 10 min at 4ºC.

The two fractions were transferred to two separate tubes, washed with DMEM/F-12 GlutaMAX containing 10% FBS and 1%P/S, and vortexed in TRIzol for RNA extraction.

RNA-Sequencing and immune cell deconvolution
Extracted RNA samples were analyzed for RNA integrity number (RIN) using the Bioanalyzer (Agilent) and sequenced using Illumina NovaSeq at the Rockefeller University Genomics Resource Center. Reads were trimmed with Cutadapt, aligned to mm10 reference genome using STAR, and quantified using featureCounts. Differential gene expression analysis was performed using DESeq2 (Love et al., 2014). Pathway analysis was performed using clusterProfiler (Yu et al., 2012). Deconvolution analysis was performed with CIBERSORTx (Newman et al., 2019) using ImmuCC signature matrix (Chen et al. 2017).

Tissue origin prediction
Mouse tissue mRNA sequencing data from ENCODE was downloaded from GSE36026. Reads were mapped and quantified as above and gene expression was normalized using DESeq2. Genes detected in mouse nascent serum were selected for t-SNE analysis. Briefly, average normalized expression in a tissue was divided by summed expression across tissues. Tissue with the highest relative expression was designated as the highest expressing tissue for a gene. t-SNE analysis was performed on relative expression values with R package Rtsne (https://github.com/jkrijthe/Rtsne) using a perplexity of 30 and maximum iteration of 1,000.

Immunoblot
Upon collection, conditioned medium (CM) was filtered using a 0.22 μm PES membrane syringe filter unit to remove cell debris. CM was concentrated using a 3 kDa centrifugal filter units (Millipore), and protein concentration was determined using Pierce BCA Protein Assay Kit (Thermo Scientific) using a dilution series of bovine serum albumin as protein standards. Mouse serum samples were loaded at equal volume. Pre-cast polyacrylamide gels were used for electrophoresis, after which protein was transferred to PVDF membrane using standard techniques. Immunoblots were incubated with indicated primary antibodies and developed using Western Lightning Plus-ECL (PerkinElmer) and imaged on an autoradiographic film or using a Bio-Rad Gel Doc system.

Co-immunoprecipitation
Serum was diluted 1:1 with PBS containing 0.02% Tween-20 (PBS-T) and incubated with α-FLAG M2 beads (Sigma) overnight at 4ºC. Following wash with PBS-T, bound proteins were eluted by heating the beads at 70ºC in Laemmli buffer containing 50 mM glycine buffer pH 2.8 and 9% (v/v) β-mercaptoethanol.

Immunofluorescence
Cells were fixed with cold methanol followed by permeabilization with PBS containing 0.25% Triton X-100, followed by delipidation with ethanol. After washing with buffers B1N and PTxwH (Chi et al., 2018), cells were blocked with 3% donkey serum in PTxwH buffer. Staining was performed by adding 1:200 dilution of α-C11orf54 (Novus) and α-KDEL (Abcam) antibodies. C11orf54 antibody was detected using donkey α-Rabbit Alexa Fluor Plus 647 (Invitrogen), while KDEL was detected using donkey α-Mouse Alexa Fluor 568 (Invitrogen), followed by nuclear

staining with DAPI. Images were taken using DeltaVision Image Restoration Microscope (Applied Precision).

Adenovirus production and purification

Adenoviral vectors were created using the AdEasy system (Luo et al., 2007). C-terminally 3xFLAG-tagged murine LRG1 or C11orf54 isoform 1 or 2 was cloned into pAdTrack-CMV (AddGene) linearized with XhoI (NEB) and HindIII (NEB) using In-Fusion® HD Cloning Kit (Takara). pAdTrack-CMV control and pAdTrack-CMV-LRG1-FL plasmids were linearized with PmeI (NEB) and recombined into pAdEasy-1 vector via electrophoretic transformation of recombination-competent BJ5183-AD-1 cells (Agilent) with the linearized product and selection for kanamycin-resistant clones. Plasmids from validated clones were transformed into recombination-deficient XL-10 Gold ultracompetent cells (Agilent), which were used to generate pAd-eGFP and pAd-LRG1-FL plasmids and purified using Plasmid Maxi Kit (Qiagen).

Crude adenovirus was produced by transfecting PacI (NEB)-linearized pAd vectors into HEK293A cells (Invitrogen), which were incubated at 37ºC with 5% CO2 for 10-14 days with media supplementation every 3-5 days until most cells showed cytopathic effect/detachment. Both cells and the culture medium were collected, lysed by 3 cycles of freeze-thaw between dry ice-ethanol and room-temperature water baths, and centrifuged at 3500×g for 15 min at 4ºC to obtain the supernatant crude virus. Round 1 amplification product was obtained by transducing HEK293A cells with the crude virus and repeating the above collection, lysis, and centrifugation steps.

To obtain round 2 amplification product, twelve 15 cm plates of HEK293A cells were transduced with round 1 adenovirus and incubated at 37ºC with 5% CO2 until most cells demonstrated cytopathic effect. As with previous rounds, cells and media were collected, lysed by freeze-thaw cycles, and centrifuged to obtain the supernatant. The supernatant was treated with benzonase, and adenoviral particles were purified from the crude mixture using the Vivapure AdenoPACK 100 kit (Sartorius). Purified virus was dialyzed with buffer containing 20 mM Tris pH 8, 25 mM NaCl, and 2.5% (w/v) glycerol and concentrated using a 100 kDa centrifugal filter unit provided with the kit. Titer of the adenovirus was determined using Adeno-X Rapid Titer Kit (Takara).

AAV8 vector preparation

C-terminally 3xFLAG-tagged LRG1 was cloned into pENN.AAV.CB7.CI.eGFP.WPRE.rBG (Addgene) linearized with EcoRI (NEB) and BglII (NEB) using In-Fusion® HD Cloning Kit (Takara). The original eGFP-expressing and cloned LRG1-FL plasmids were transformed into Stable Competent E. coli (NEB), purified using Plasmid Maxi Kit (Qiagen), and shipped to Penn Vector Core (PA, USA) for AAV8 production.

***In vivo* adenovirus/AAV8 transduction**

In vivo adenoviral transduction studies were performed using purified adenovirus from second round of amplification. Adenovirus was injected at a dose of 10^{10} pfu/mouse. AAV8 was injected at 10^{11} GC/mouse. The mice were briefly anesthetized with isoflurane for virus injection via the retroorbital route. Following injection, the mice were quarantined in an ABSL-2 housing room for 72 h before transferred back to regular housing conditions.

Metabolic characterization of mice

For studies involving diet-induced obesity, mouse body weights were monitored once a week, providing fresh 60% high fat diet (Research Diets) at least once a week. For fasting glucose measurements, mice were single housed in the morning in cages with fresh bedding and access to water but without food. Mice were kept in a procedure room free of noise or vibration throughout the experiment. After 6 h, blood was collected from the tail vein, and glucose levels were measured using a glucose meter. For plasma insulin ELISA, blood was also collected in EDTA-coated capillary tubes, which were centrifuged at 2000×g for 15 min at 4ºC to collect plasma. Insulin ELISA was performed using Ultra Sensitive Mouse Insulin ELISA Kit (Crystal Chem). Glucose (GTT) and insulin tolerance tests (ITT) were performed following a similar 6 h fasting procedure and started by intraperitoneally injecting at time 0 indicated doses of glucose or Novolin R human insulin (Novo Nordisk). Following injection, blood glucose measurements were taken from the tail vein at indicated timepoints. During an ITT procedure, mice with glucose measurements below 20 mg/dL or showing signs of hypoglycemia were rescued by 1 g/kg glucose IP injection and excluded from the study. For measurements of energy expenditure, mice were single housed in PhenoMaster indirect calorimetry system (TSE Systems) maintained at 22ºC and 55% relative humidity, with *ad libitum* access to food and drinking water.

Generation of LRG1-KO mice

CRISPR guide RNAs were designed using CRISPOR.org (Concordet and Haeussler, 2018) and were used as two-part synthetic crRNA and tracrRNA (Alt-RTM CRISPR guide RNA, Integrated DNA Technologies, Inc). Cas9 protein, crRNA, and tracrRNA were assembled to ctRNP using protocols described previously (Shola et al., 2021). Two crRNAs were assembled to ctRNPs and electroporated to one-cell-stage mouse embryos to assess their efficiency in generating indels on the Exon 2 of *Lrg1* gene. To prepare for the microinjection mix, crRNA-B which binds to genomic target sequence "AATCTCGGTGGGACCATGGCAGG" was selected for its high on-target efficiency and low off-target potential. The final injection mix was made of 0.6 μM of guide RNA (crRNA + tracrRNA) and 0.3 μM of Cas9 protein according to protocols described previously (Shola et al., 2021). The injection mix was then delivered to 0.5 days of fertilized C57BL/6J mouse embryos using well-established pronuclear injection and surgical protocols (Shola et al., 2021).

H&E section preparation/CLS quantification

Dissected tissues were fixed in 10% neutral buffered formalin for 3 days at room temperature and transferred to 70% ethanol. Paraffin embedding, sectioning, and H&E staining was performed by the Memorial Sloan Kettering Cancer Center Laboratory of Comparative Pathology. The slides were imaged using a wide-field fluorescence/brightfield/DIC microscope (Zeiss) at the Rockefeller University Bioimaging Resource Center. Crown-like structures (CLS) were identified as any adipocyte in a field of view with cellular infiltrates indicated by nuclear staining surrounding a majority of adipocyte perimeter. Objectives were used as indicated and chosen based on CLS enumerability (<30 CLS per field). 5 fields from 3 animals were quantified per group.

Multiplex cytokine panel

Mouse serum samples were diluted 1:1 with PBS, snap frozen using liquid N2 and shipped to Eve Technologies (Alberta, Canada) on dry ice. The Mouse Cytokine Array / Chemokine Array 31-Plex (MD31) panel was used to quantify the levels of cytokines and chemokines

Cytochrome *c* clearance assay

12-week-old chow-fed LRG1-KO and WT littermate males were injected retro-orbitally with 40 mg/kg equine cytochrome c (Cyt *c*) in PBS. Blood was collected from the tail vein immediately prior to injection (0 min) and 5 min, 15 min, 30 min, 1 h, 2 h, 4 h, and 6 h post-injection into EDTA-coated capillary tubes and kept in ice until further processing. During blood collection, each mouse was placed on a metal grating above a clean plastic wrap to allow collection of excreted urine, if any. Plasma was isolated via centrifugation at 2000×g for 15 min at 4ºC. Immunoblot against Cyt *c* was performed with WT and KO plasma samples run pairwise to enable relative quantification of Cyt *c* signal. Quantification was performed using ImageJ (Schneider et al., 2012).

Quantification and Statistical Analysis

Unless otherwise noted, data are presented as mean ± SEM, with n number specified in the figure legends. Statistical analyses were performed with GraphPad Prism 9. Binary comparisons were performed with Welch's *t*-test to account for possible difference in variance. Statistical analysis of data involving 3 or more conditions (levels) of a single variable was performed using one-way ANOVA followed by Dunnett post hoc tests to compare every mean with a control mean. Data measured across multiple time points as in GTT and ITT were analyzed with repeated measures two-way ANOVA, reporting group factor *P*-values. Analysis of data from a two-factor experimental setup was performed with two-way ANOVA or two-way mixed effects ANOVA in the case of an uneven n number, reporting group factor *P*-values. For post hoc tests, Tukey method was used when comparing every mean with every other mean and Šídák method was employed when a selected set of means were compared.

Table 6.1. List of antibodies used

Antibodies	Source	Identifier
α-LRG1	Sigma-Aldrich	Cat# HPA001888, RRID:AB_1079276
α-CFD/Adipsin	R and D Systems	Cat# AF5430, RRID:AB_1655868
α-Cytochrome c	Cell Signaling Technology	Cat# 11940, RRID:AB_2637071
α-FLAG M2 Magnetic Beads	Sigma-Aldrich	Cat# M8823, RRID:AB_2637089
α-C11orf54	Novus	Novus Cat# NBP1-87194, RRID:AB_11033874
α-KDEL	Abcam	Abcam Cat# ab12223, RRID:AB_298945
Donkey α-Rabbit IgG (H+L) Antibody Alexa Fluor Plus 647	Invitrogen	Cat# A32795, RRID:AB_2762835
Donkey α-Mouse IgG (H+L) Antibody Alexa Fluor 568	Invitrogen	Cat# A10037, RRID:AB_2534013

Table 6.2. List of RT-qPCR primers used

Gene	Forward Primer (5' to 3')	Reverse Primer (5' to 3')
Fabp4	ACACCGAGATTTCCTTCAAACTG	CCATCTAGGGTTATGATGCTCTTCA
Pparg2	GCATGGTGCCTTCGCTGA	TGGCATCTCTGTGTCAACCATG
Adipoq	GCACTGGCAAGTTCTACTGCAA	GTAGGTGAAGAGAACGGCCTTGT
Prdm16	CAGCACGGTGAAGCCATTC	GCGTGCATCCGCTTGTG
Ucp1	CTTTGCCTCACTCAGGATTGG	ACTGCCACACCTCCAGTCATT
C11orf54 Iso1	GAGCTTGCTGAAGTTTTGCAG	CAGATGCCTCTTACAGGAAAGG
C11orf54 Iso2	AGCTTGCTGAAGGCATCTGTG	TGCCCCTGCTCCAAGGATAA
Lrg1	ATCAAGGAAGCCTCCAGGATCT	CTCAGCCGACTGCAGTATCA
Il1b	GCAACTGTTCCTGAACTCAACT	ATCTTTTGGGGTCCGTCAACT
Cxcl10	GGATCCCTCTCGCAAGGA	ATCGTGGCAATGATCTCAACA
Il6	TAGTCCTTCCTACCCCAATTTCC	TTGGTCCTTAGCCACTCCTTC
Nos2	GTTCTCAGCCCAACAATACAAGA	GTGGACGGGTCGATGTCAC
Rn18s	CGATGCTCTTAGCTGAGTGT	GGTCCAAGAATTTCACCTCT

CHAPTER 7. References

Adachi, N., Hirota, M., Hamaguchi, M., Okamoto, K., Watanabe, K., Endo, F., (2004). Serum cytochrome c level as a prognostic indicator in patients with systemic inflammatory response syndrome. *Clinica Chimica Acta* 342, 127–136. https://doi.org/10.1016/j.cccn.2003.12.011

Ahima, R.S., Prabakaran, D., Mantzoros, C., Qu, D., Lowell, B., Maratos-Flier, E., Flier, J.S., (1996). Role of leptin in the neuroendocrine response to fasting. *Nature* 382, 250–252. https://doi.org/10.1038/382250a0

Alleyne, T., Joseph, J., Sampson, V., (2001). Cytochrome- c Detection: A Diagnostic Marker for Myocardial Infarction. *ABAB* 90, 97–106. https://doi.org/10.1385/ABAB:90:2:97

Almagro Armenteros, J.J., Sønderby, C.K., Sønderby, S.K., Nielsen, H., Winther, O., (2017). DeepLoc: prediction of protein subcellular localization using deep learning. *Bioinformatics* 33, 3387–3395. https://doi.org/10.1093/bioinformatics/btx431

Almagro Armenteros, J.J., Tsirigos, K.D., Sønderby, C.K., Petersen, T.N., Winther, O., Brunak, S., von Heijne, G., Nielsen, H., (2019). SignalP 5.0 improves signal peptide predictions using deep neural networks. *Nature Biotechnology* 37, 420–423. https://doi.org/10.1038/s41587-019-0036-z

Alshargabi, R., Shinjo, T., Iwashita, M., Yamashita, A., Sano, T., Nishimura, Y., Hayashi, M., Zeze, T., Fukuda, T., Sanui, T., Nishimura, F., (2020). SPOCK1 induces adipose tissue maturation: New insights into the function of SPOCK1 in metabolism. *Biochemical and Biophysical Research Communications* 533, 1076–1082. https://doi.org/10.1016/j.bbrc.2020.09.129

Alvarez-Castelao, B., Schanzenbächer, C.T., Hanus, C., Glock, C., tom Dieck, S., Dörrbaum, A.R., Bartnik, I., Nassim-Assir, B., Ciirdaeva, E., Mueller, A., Dieterich, D.C., Tirrell, D.A., Langer, J.D., Schuman, E.M., (2017). Cell-type-specific metabolic labeling of nascent proteomes in vivo. *Nature Biotechnology* 35, 1196–1201. https://doi.org/10.1038/nbt.4016

Angelantonio, E.D., Bhupathiraju, S.N., Wormser, D., Gao, P., Kaptoge, S., Gonzalez, A.B. de, Cairns, B.J., Huxley, R., Jackson, C.L., Joshy, G., et al., (2016). Body-mass index and all-cause mortality: individual-participant-data meta-analysis of 239 prospective studies in four continents. *The Lancet* 388, 776–786. https://doi.org/10.1016/S0140-6736(16)30175-1

Arner, P., Kulyté, A., (2015). MicroRNA regulatory networks in human adipose tissue and obesity. *Nat Rev Endocrinol* 11, 276–288. https://doi.org/10.1038/nrendo.2015.25

Axelrod, L., Trzepacz, P.T., Zusman, R.M., Martin, D.B., (1976). Antilipolytic effect of prostaglandin E2 analogues: Therapeutic implications. *Life Sciences* 18, 627–632. https://doi.org/10.1016/0024-3205(76)90343-X

Axelrod, L., Levine, L., (1981). Prostacyclin Production by Isolated Adipocytes. *Diabetes* 30, 163–167. https://doi.org/10.2337/diab.30.2.163

Barczyk, K., Kreuter, M., Pryjma, J., Booy, E.P., Maddika, S., Ghavami, S., Berdel, W.E., Roth, J., Los, M., (2005). Serum cytochrome c indicates in vivo apoptosis and can serve as a prognostic marker during cancer therapy. *International Journal of Cancer* 116, 167–173. https://doi.org/10.1002/ijc.21037

Becher, T., Palanisamy, S., Kramer, D.J., Eljalby, M., Marx, S.J., Wibmer, A.G., Butler, S.D., Jiang, C.S., Vaughan, R., Schöder, H., Mark, A., Cohen, P., (2021). Brown adipose tissue is associated with cardiometabolic health. *Nature Medicine* 27, 58–65. https://doi.org/10.1038/s41591-020-1126-7

Belczacka, I., Latosinska, A., Metzger, J., Marx, D., Vlahou, A., Mischak, H., Frantzi, M., (2019). Proteomics biomarkers for solid tumors: Current status and future prospects. *Mass Spectrometry Reviews* 38, 49–78. https://doi.org/10.1002/mas.21572

Bendtsen, J.D., Jensen, L.J., Blom, N., von Heijne, G., Brunak, S., (2004). Feature-based prediction of non-classical and leaderless protein secretion. *Protein Engineering, Design and Selection* 17, 349–356. https://doi.org/10.1093/protein/gzh037

Ben-Ari, Z., Schmilovotz‐Weiss, H., Belinki, A., Pappo, O., Sulkes, J., Neuman, M.G., Kaganovsky, E., Kfir, B., Tur‐Kaspa, R., Klein, T., (2003). Circulating soluble cytochrome c in liver disease as a marker of apoptosis. *Journal of Internal Medicine* 254, 168–175. https://doi.org/10.1046/j.1365-2796.2003.01171.x

Berg, A.H., Combs, T.P., Du, X., Brownlee, M., Scherer, P.E., (2001). The adipocyte-secreted protein Acrp30 enhances hepatic insulin action. *Nature Medicine* 7, 947–953. https://doi.org/10.1038/90992

Berndt, J., Klöting, N., Kralisch, S., Kovacs, P., Fasshauer, M., Schön, M.R., Stumvoll, M., Blüher, M., (2005). Plasma Visfatin Concentrations and Fat Depot–Specific mRNA Expression in Humans. *Diabetes* 54, 2911–2916. https://doi.org/10.2337/diabetes.54.10.2911

Birsoy, K., Berry, R., Wang, T., Ceyhan, O., Tavazoie, S., Friedman, J.M., Rodeheffer, M.S., (2011). Analysis of gene networks in white adipose tissue development reveals a role for ETS2 in adipogenesis. *Development* 138, 4709–4719. https://doi.org/10.1242/dev.067710

Boström, P., Wu, J., Jedrychowski, M.P., Korde, A., Ye, L., Lo, J.C., Rasbach, K.A., Boström, E.A., Choi, J.H., Long, J.Z., Kajimura, S., Zingaretti, M.C., Vind, B.F., Tu, H., Cinti, S., Højlund, K., Gygi, S.P., Spiegelman, B.M., (2012). A PGC1-α-dependent myokine that drives brown-fat-like development of white fat and thermogenesis. *Nature* 481, 463–468. https://doi.org/10.1038/nature10777

Branon, T.C., Bosch, J.A., Sanchez, A.D., Udeshi, N.D., Svinkina, T., Carr, S.A., Feldman, J.L., Perrimon, N., Ting, A.Y., (2018). Efficient proximity labeling in living cells and organisms with TurboID. *Nature Biotechnology* 36, 880–887. https://doi.org/10.1038/nbt.4201

Brunetti, L., Recinella, L., Di Nisio, C., Chiavaroli, A., Leone, S., Ferrante, C., Orlando, G., Vacca, M., (2012). Effects of visfatin/PBEF/NAMPT on feeding behaviour and hypothalamic neuromodulators in the rat. *J. Biol. Regul. Homeost. Agents* 26, 295–302.

Calve, S., Witten, A.J., Ocken, A.R., Kinzer-Ursem, T.L., (2016). Incorporation of non-canonical amino acids into the developing murine proteome. *Scientific Reports* 6, 32377. https://doi.org/10.1038/srep32377

Cao, H., Gerhold, K., Mayers, J.R., Wiest, M.M., Watkins, S.M., Hotamisligil, G.S., (2008). Identification of a Lipokine, a Lipid Hormone Linking Adipose Tissue to Systemic Metabolism. *Cell* 134, 933–944. https://doi.org/10.1016/j.cell.2008.07.048

Cao, H., Sekiya, M., Ertunc, M.E., Burak, M.F., Mayers, J.R., White, A., Inouye, K., Rickey, L.M., Ercal, B.C., Furuhashi, M., Tuncman, G., Hotamisligil, G.S., (2013). Adipocyte Lipid Chaperone aP2 Is a Secreted Adipokine Regulating Hepatic Glucose Production. *Cell Metabolism* 17, 768–778. https://doi.org/10.1016/j.cmet.2013.04.012

Chan, K.L., Pillon, N.J., Sivaloganathan, D.M., Costford, S.R., Liu, Z., Théret, M., Chazaud, B., Klip, A., (2015). Palmitoleate Reverses High Fat-induced Proinflammatory Macrophage Polarization via AMP-activated Protein Kinase (AMPK). *J. Biol. Chem.* 290, 16979–16988. https://doi.org/10.1074/jbc.M115.646992

Chau, Y.-Y., Bandiera, R., Serrels, A., Martínez-Estrada, O.M., Qing, W., Lee, M., Slight, J., Thornburn, A., Berry, R., McHaffie, S., Stimson, R.H., Walker, B.R., Chapuli, R.M., Schedl, A., Hastie, N., (2014). Visceral and subcutaneous fat have different origins and evidence supports a mesothelial source. *Nature Cell Biology* 16, 367–375. https://doi.org/10.1038/ncb2922

Chen, Z., Huang, A., Sun, J., Jiang, T., Qin, F.X.-F., Wu, A., (2017). Inference of immune cell composition on the expression profiles of mouse tissue. *Scientific Reports* 7, 40508. https://doi.org/10.1038/srep40508

Chi, J., Wu, Z., Choi, C.H.J., Nguyen, L., Tegegne, S., Ackerman, S.E., Crane, A., Marchildon, F., Tessier-Lavigne, M., Cohen, P., (2018). Three-Dimensional Adipose Tissue Imaging Reveals Regional Variation in Beige Fat Biogenesis and PRDM16-Dependent Sympathetic Neurite Density. *Cell Metabolism* 27, 226-236.e3. https://doi.org/10.1016/j.cmet.2017.12.011

Chi, J., Lin, Z., Barr, W., Crane, A., Zhu, X.G., Cohen, P., (2021). Early postnatal interactions between beige adipocytes and sympathetic neurites regulate innervation of subcutaneous fat. *eLife* 10, e64693. https://doi.org/10.7554/eLife.64693

Çimen, I., Kocatürk, B., Koyuncu, S., Tufanlı, Ö., Onat, U.I., Yıldırım, A.D., Apaydın, O., Demirsoy, Ş., Aykut, Z.G., Nguyen, U.T., Watkins, S.M., Hotamışlıgil, G.S., Erbay, E., (2016). Prevention of atherosclerosis by bioactive palmitoleate through suppression of organelle stress and inflammasome activation. *Science Translational Medicine* 8, 358ra126-358ra126. https://doi.org/10.1126/scitranslmed.aaf9087

Cinti, S., Mitchell, G., Barbatelli, G., Murano, I., Ceresi, E., Faloia, E., Wang, S., Fortier, M., Greenberg, A.S., Obin, M.S., (2005). Adipocyte death defines macrophage localization and function in adipose tissue of obese mice and humans. *Journal of Lipid Research* 46, 2347–2355. https://doi.org/10.1194/jlr.M500294-JLR200

Codina, R., Vanasse, A., Kelekar, A., Vezys, V., Jemmerson, R., (2010). Cytochrome c-induced lymphocyte death from the outside in: inhibition by serum leucine-rich alpha-2-glycoprotein-1. *Apoptosis* 15, 139–152. https://doi.org/10.1007/s10495-009-0412-0

Cohen, P., Kajimura, S., (2021). The cellular and functional complexity of thermogenic fat. *Nature Reviews Molecular Cell Biology* 1–17. https://doi.org/10.1038/s41580-021-00350-0

Combs, T.P., Berg, A.H., Obici, S., Scherer, P.E., Rossetti, L., (2001). Endogenous glucose production is inhibited by the adipose-derived protein Acrp30. *J Clin Invest* 108, 1875–1881. https://doi.org/10.1172/JCI14120

Concordet, J.-P., Haeussler, M., (2018). CRISPOR: intuitive guide selection for CRISPR/Cas9 genome editing experiments and screens. *Nucleic Acids Research* 46, W242–W245. https://doi.org/10.1093/nar/gky354

Cook, K.S., Min, H.Y., Johnson, D., Chaplinsky, R.J., Flier, J.S., Hunt, C.R., Spiegelman, B.M., (1987). Adipsin: a circulating serine protease homolog secreted by adipose tissue and sciatic nerve. *Science* 237, 402–405. https://doi.org/10.1126/science.3299705

Cox, J., Hein, M.Y., Luber, C.A., Paron, I., Nagaraj, N., Mann, M., (2014). Accurate Proteome-wide Label-free Quantification by Delayed Normalization and Maximal Peptide Ratio Extraction, Termed MaxLFQ *. *Molecular & Cellular Proteomics* 13, 2513–2526. https://doi.org/10.1074/mcp.M113.031591

Cummings, C., Walder, J., Treeful, A., Jemmerson, R., (2006). Serum leucine-rich alpha-2-glycoprotein-1 binds cytochrome c and inhibits antibody detection of this apoptotic marker in enzyme-linked immunosorbent assay. *Apoptosis* 11, 1121–1129. https://doi.org/10.1007/s10495-006-8159-3

Cypess, A.M., Lehman, S., Williams, G., Tal, I., Rodman, D., Goldfine, A.B., Kuo, F.C., Palmer, E.L., Tseng, Y.-H., Doria, A., Kolodny, G.M., Kahn, C.R., (2009). Identification and Importance of Brown Adipose Tissue in Adult Humans. *New England Journal of Medicine* 360, 1509–1517. https://doi.org/10.1056/NEJMoa0810780

Davis, C.A., Hitz, B.C., Sloan, C.A., Chan, E.T., Davidson, J.M., Gabdank, I., Hilton, J.A., Jain, K., Baymuradov, U.K., Narayanan, A.K., Onate, K.C., Graham, K., Miyasato, S.R., Dreszer, T.R., Strattan, J.S., Jolanki, O., Tanaka, F.Y., Cherry, J.M., (2018). The Encyclopedia of DNA elements (ENCODE): data portal update. *Nucleic Acids Research* 46, D794–D801. https://doi.org/10.1093/nar/gkx1081

Deng, Z., Poliakov, A., Hardy, R.W., Clements, R., Liu, C., Liu, Y., Wang, J., Xiang, X., Zhang, S., Zhuang, X., Shah, S.V., Sun, D., Michalek, S., Grizzle, W.E., Garvey, T., Mobley, J., Zhang, H.-G., (2009). Adipose Tissue Exosome-Like Vesicles Mediate Activation of Macrophage-Induced Insulin Resistance. *Diabetes* 58, 2498–2505. https://doi.org/10.2337/db09-0216

Deshmukh, A.S., Peijs, L., Beaudry, J.L., Jespersen, N.Z., Nielsen, C.H., Ma, T., Brunner, A.D., Larsen, T.J., Bayarri-Olmos, R., Prabhakar, B.S., Helgstrand, C., Severinsen, M.C.K., Holst, B., Kjaer, A., Tang-Christensen, M., Sanfridson, A., Garred, P., Privé, G.G., Pedersen, B.K., Gerhart-Hines, Z., Nielsen, S., Drucker, D.J., Mann, M., Scheele, C., (2019). Proteomics-Based Comparative Mapping of the Secretomes of Human Brown and White Adipocytes Reveals EPDR1 as a Novel Batokine. *Cell Metabolism* 0. https://doi.org/10.1016/j.cmet.2019.10.001

Dieterich, D.C., Link, A.J., Graumann, J., Tirrell, D.A., Schuman, E.M., 2006. Selective identification of newly synthesized proteins in mammalian cells using bioorthogonal noncanonical amino acid tagging (BONCAT). *PNAS* 103, 9482–9487. https://doi.org/10.1073/pnas.0601637103

Dobson, D.E., Kambe, A., Block, E., Dion, T., Lu, H., Castellot, J.J., Spiegelman, B.M., (1990). 1-Butyryl-Glycerol: A novel angiogenesis factor secreted by differentiating adipocytes. *Cell* 61, 223–230. https://doi.org/10.1016/0092-8674(90)90803-M

Dunham, I., Kundaje, A., Aldred, S.F., Collins, P.J., Davis, C.A., Doyle, F., Epstein, C.B., Frietze, S., Harrow, J., Kaul, R., et al., (2012). An integrated encyclopedia of DNA elements in the human genome. *Nature* 489, 57–74. https://doi.org/10.1038/nature11247

Eichelbaum, K., Winter, M., Diaz, M.B., Herzig, S., Krijgsveld, J., (2012). Selective enrichment of newly synthesized proteins for quantitative secretome analysis. *Nature Biotechnology* 30, 984–990. https://doi.org/10.1038/nbt.2356

Eichelbaum, K., Krijgsveld, J., (2014). Combining Pulsed SILAC Labeling and Click-Chemistry for Quantitative Secretome Analysis, in: Ivanov, A.I. (Ed.), *Exocytosis and Endocytosis, Methods in Molecular Biology*. Springer New York, pp. 101–114. https://doi.org/10.1007/978-1-4939-0944-5_7

Eleftheriadis, T., Pissas, G., Liakopoulos, V., Stefanidis, I., (2016). Cytochrome c as a Potentially Clinical Useful Marker of Mitochondrial and Cellular Damage. *Front. Immunol.* 7. https://doi.org/10.3389/fimmu.2016.00279

Ertunc, M.E., Sikkeland, J., Fenaroli, F., Griffiths, G., Daniels, M.P., Cao, H., Saatcioglu, F., Hotamisligil, G.S., (2015). Secretion of fatty acid binding protein aP2 from adipocytes through a nonclassical pathway in response to adipocyte lipase activity. *J. Lipid Res*. 56, 423–434. https://doi.org/10.1194/jlr.M055798

Farrell, G., Schattenberg, J.M., Leclercq, I., Yeh, M.M., Goldin, R., Teoh, N., Schuppan, D., (2019). Mouse Models of Nonalcoholic Steatohepatitis: Toward Optimization of Their

Relevance to Human Nonalcoholic Steatohepatitis. *Hepatology* 69, 2241–2257. https://doi.org/10.1002/hep.30333

Febbraio, M.A., Reibe, S., Shalapour, S., Ooi, G.J., Watt, M.J., Karin, M., (2019). Preclinical Models for Studying NASH-Driven HCC: How Useful Are They? *Cell Metabolism* 29, 18–26. https://doi.org/10.1016/j.cmet.2018.10.012

Fedorenko, A., Lishko, P.V., Kirichok, Y., (2012). Mechanism of Fatty-Acid-Dependent UCP1 Uncoupling in Brown Fat Mitochondria. *Cell* 151, 400–413. https://doi.org/10.1016/j.cell.2012.09.010

Feldstein, A.E., Canbay, A., Angulo, P., Taniai, M., Burgart, L.J., Lindor, K.D., Gores, G.J., (2003). Hepatocyte apoptosis and fas expression are prominent features of human nonalcoholic steatohepatitis. *Gastroenterology* 125, 437–443. https://doi.org/10.1016/S0016-5085(03)00907-7

Finkelstein, E.A., Trogdon, J.G., Cohen, J.W., Dietz, W., (2009). Annual Medical Spending Attributable To Obesity: Payer-And Service-Specific Estimates. *Health Affairs* 28, w822–w831. https://doi.org/10.1377/hlthaff.28.5.w822

Flier, J.S., Cook, K.S., Usher, P., Spiegelman, B.M., (1987). Severely impaired adipsin expression in genetic and acquired obesity. *Science* 237, 405–408. https://doi.org/10.1126/science.3299706

Fox C.S., Massaro J.M., Hoffmann U., Pou K.M., Maurovich-Horvat P., Liu C.-Y., Vasan R.S., Murabito J.M., Meigs J.B., Cupples L.A., D'Agostino R.B., O'Donnell C.J., (2007). Abdominal Visceral and Subcutaneous Adipose Tissue Compartments. *Circulation* 116, 39–48. https://doi.org/10.1161/CIRCULATIONAHA.106.675355

Frigolet, M.E., Gutiérrez-Aguilar, R., (2017). The Role of the Novel Lipokine Palmitoleic Acid in Health and Disease. *Adv Nutr* 8, 173S-181S. https://doi.org/10.3945/an.115.011130

Fukuhara, A., Matsuda, M., Nishizawa, M., Segawa, K., Tanaka, M., Kishimoto, K., Matsuki, Y., Murakami, M., Ichisaka, T., Murakami, H., Watanabe, E., Takagi, T., Akiyoshi, M., Ohtsubo, T., Kihara, S., Yamashita, S., Makishima, M., Funahashi, T., Yamanaka, S., Hiramatsu, R., Matsuzawa, Y., Shimomura, I., (2005). Visfatin: A Protein Secreted by Visceral Fat That Mimics the Effects of Insulin. *Science* 307, 426–430. https://doi.org/10.1126/science.1097243

Fukuhara, A., Matsuda, M., Nishizawa, M., Segawa, K., Tanaka, M., Kishimoto, K., Matsuki, Y., Murakami, M., Ichisaka, T., Murakami, H., Watanabe, E., Takagi, T., Akiyoshi, M., Ohtsubo, T., Kihara, S., Yamashita, S., Makishima, M., Funahashi, T., Yamanaka, S., Hiramatsu, R., Matsuzawa, Y., Shimomura, I., (2007). Retraction. *Science* 318, 565–565. https://doi.org/10.1126/science.318.5850.565b

Gabriely, I., Ma, X.H., Yang, X.M., Atzmon, G., Rajala, M.W., Berg, A.H., Scherer, P., Rossetti, L., Barzilai, N., (2002). Removal of Visceral Fat Prevents Insulin Resistance and Glucose

Intolerance of Aging: An Adipokine-Mediated Process? *Diabetes* 51, 2951–2958. https://doi.org/10.2337/diabetes.51.10.2951

Garten, A., Schuster, S., Penke, M., Gorski, T., de Giorgis, T., Kiess, W., (2015). Physiological and pathophysiological roles of NAMPT and NAD metabolism. *Nat Rev Endocrinol* 11, 535–546. https://doi.org/10.1038/nrendo.2015.117

Gómez-Banoy, N., Guseh, J.S., Li, G., Rubio-Navarro, A., Chen, T., Poirier, B., Putzel, G., Rosselot, C., Pabón, M.A., Camporez, J.P., Bhambhani, V., Hwang, S.-J., Yao, C., Perry, R.J., Mukherjee, S., Larson, M.G., Levy, D., Dow, L.E., Shulman, G.I., Dephoure, N., Garcia-Ocana, A., Hao, M., Spiegelman, B.M., Ho, J.E., Lo, J.C., (2019). Adipsin preserves beta cells in diabetic mice and associates with protection from type 2 diabetes in humans. *Nature Medicine* 25, 1739–1747. https://doi.org/10.1038/s41591-019-0610-4

Gouveia, A., Bajwa, E., Klegeris, A., (2017). Extracellular cytochrome c as an intercellular signaling molecule regulating microglial functions. *Biochimica et Biophysica Acta (BBA) - General Subjects* 1861, 2274–2281. https://doi.org/10.1016/j.bbagen.2017.06.017

Grazioli, S., Pugin, J., (2018). Mitochondrial Damage-Associated Molecular Patterns: From Inflammatory Signaling to Human Diseases. *Front. Immunol*. 9. https://doi.org/10.3389/fimmu.2018.00832

Guay, C., Regazzi, R., (2013). Circulating microRNAs as novel biomarkers for diabetes mellitus. *Nat Rev Endocrinol* 9, 513–521. https://doi.org/10.1038/nrendo.2013.86

Haupt, H., Baudner, S., (1977). [Isolation and characterization of an unknown, leucine-rich 3.1-S-alpha2-glycoprotein from human serum (author's transl)]. *Hoppe Seylers Z Physiol Chem* 358, 639–646.

Herman, M.A., Peroni, O.D., Villoria, J., Schön, M.R., Abumrad, N.A., Blüher, M., Klein, S., Kahn, B.B., (2012). A novel ChREBP isoform in adipose tissue regulates systemic glucose metabolism. *Nature* 484, 333–338. https://doi.org/10.1038/nature10986

Heymsfield, S.B., Greenberg, A.S., Fujioka, K., Dixon, R.M., Kushner, R., Hunt, T., Lubina, J.A., Patane, J., Self, B., Hunt, P., McCamish, M., (1999). Recombinant Leptin for Weight Loss in Obese and Lean Adults: A Randomized, Controlled, Dose-Escalation Trial. *JAMA* 282, 1568. https://doi.org/10.1001/jama.282.16.1568

Hocking, S.L., Wu, L.E., Guilhaus, M., Chisholm, D.J., James, D.E., (2010). Intrinsic Depot-Specific Differences in the Secretome of Adipose Tissue, Preadipocytes, and Adipose Tissue–Derived Microvascular Endothelial Cells. *Diabetes* 59, 3008–3016. https://doi.org/10.2337/db10-0483

Holland, W.L., Miller, R.A., Wang, Z.V., Sun, K., Barth, B.M., Bui, H.H., Davis, K.E., Bikman, B.T., Halberg, N., Rutkowski, J.M., Wade, M.R., Tenorio, V.M., Kuo, M.-S., Brozinick, J.T., Zhang, B.B., Birnbaum, M.J., Summers, S.A., Scherer, P.E., (2011). Receptor-mediated

activation of ceramidase activity initiates the pleiotropic actions of adiponectin. *Nature Medicine* 17, 55–63. https://doi.org/10.1038/nm.2277

Hong, Q., Zhang, L., Fu, J., Verghese, D.A., Chauhan, K., Nadkarni, G.N., Li, Z., Ju, W., Kretzler, M., Cai, G.-Y., Chen, X.-M., D'Agati, V.D., Coca, S.G., Schlondorff, D., He, J.C., Lee, K., (2019). LRG1 Promotes Diabetic Kidney Disease Progression by Enhancing TGF-β–Induced Angiogenesis. JASN ASN.2018060599. https://doi.org/10.1681/ASN.2018060599

Hotamisligil, G.S., Bernlohr, D.A., (2015). Metabolic functions of FABPs—mechanisms and therapeutic implications. *Nature Reviews Endocrinology* 11, 592–605. https://doi.org/10.1038/nrendo.2015.122

Huang, D.W., Sherman, B.T., Lempicki, R.A., (2009a). Systematic and integrative analysis of large gene lists using DAVID bioinformatics resources. *Nature Protocols* 4, 44–57. https://doi.org/10.1038/nprot.2008.211

Huang, D.W., Sherman, B.T., Lempicki, R.A., (2009b). Bioinformatics enrichment tools: paths toward the comprehensive functional analysis of large gene lists. *Nucleic Acids Research* 37, 1–13. https://doi.org/10.1093/nar/gkn923

Huang-Doran, I., Zhang, C.-Y., Vidal-Puig, A., (2017). Extracellular Vesicles: Novel Mediators of Cell Communication In Metabolic Disease. *Trends in Endocrinology & Metabolism* 28, 3–18. https://doi.org/10.1016/j.tem.2016.10.003

Huber, A.H., Kleinfeld, A.M., (2017). Unbound free fatty acid profiles in human plasma and the unexpected absence of unbound palmitoleate. *J. Lipid Res*. 58, 578–585. https://doi.org/10.1194/jlr.M074260

Ikeda, K., Kang, Q., Yoneshiro, T., Camporez, J.P., Maki, H., Homma, M., Shinoda, K., Chen, Y., Lu, X., Maretich, P., Tajima, K., Ajuwon, K.M., Soga, T., Kajimura, S., (2017). UCP1-independent signaling involving SERCA2b-mediated calcium cycling regulates beige fat thermogenesis and systemic glucose homeostasis. *Nature Medicine* 23, 1454–1465. https://doi.org/10.1038/nm.4429

Jemmerson, R., LaPlante, B., Treeful, A., (2002). Release of intact, monomeric cytochrome c from apoptotic and necrotic cells. *Cell Death and Differentiation* 9, 538–548. https://doi.org/10.1038/sj.cdd.4400981

Jemmerson, R., Staskus, K., Higgins, L., Conklin, K., Kelekar, A., (2021). Intracellular leucine-rich alpha-2-glycoprotein-1 competes with Apaf-1 for binding cytochrome c in protecting MCF-7 breast cancer cells from apoptosis. *Apoptosis* 26, 71–82. https://doi.org/10.1007/s10495-020-01647-9

Kaess, B.M., Enserro, D.M., McManus, D.D., Xanthakis, V., Chen, M.-H., Sullivan, L.M., Ingram, C., O'Donnell, C.J., Keaney, J.F., Vasan, R.S., Glazer, N.L., (2012). Cardiometabolic Correlates and Heritability of Fetuin-A, Retinol-Binding Protein 4, and Fatty-Acid Binding

Protein 4 in the Framingham Heart Study. *The Journal of Clinical Endocrinology & Metabolism* 97, E1943–E1947. https://doi.org/10.1210/jc.2012-1458

Kajimura, S., Spiegelman, B.M., Seale, P., (2015). Brown and Beige Fat: Physiological Roles beyond Heat Generation. *Cell Metabolism* 22, 546–559. https://doi.org/10.1016/j.cmet.2015.09.007

Karimi, K., Lindgren, T.H., Koch, C.A., Brodell, R.T., (2016). Obesity as a risk factor for malignant melanoma and non-melanoma skin cancer. *Rev Endocr Metab Disord* 17, 389–403. https://doi.org/10.1007/s11154-016-9393-9

Kentsis, A., Lin, Y.Y., Kurek, K., Calicchio, M., Wang, Y.Y., Monigatti, F., Campagne, F., Lee, R., Horwitz, B., Steen, H., Bachur, R., (2010). Discovery and Validation of Urine Markers of Acute Pediatric Appendicitis Using High-Accuracy Mass Spectrometry. *Annals of Emergency Medicine* 55, 62-70.e4. https://doi.org/10.1016/j.annemergmed.2009.04.020

Kentsis, A., Ahmed, S., Kurek, K., Brennan, E., Bradwin, G., Steen, H., Bachur, R., (2012). Detection and Diagnostic Value of Urine Leucine-Rich α-2-Glycoprotein in Children With Suspected Acute Appendicitis. *Annals of Emergency Medicine* 60, 78-83.e1. https://doi.org/10.1016/j.annemergmed.2011.12.015

Khan, A.A., Hansson, J., Weber, P., Foehr, S., Krijgsveld, J., Herzig, S., Scheideler, M., (2018). Comparative Secretome Analyses of Primary Murine White and Brown Adipocytes Reveal Novel Adipokines *. *Molecular & Cellular Proteomics* 17, 2358–2370. https://doi.org/10.1074/mcp.RA118.000704

Kim, J.-Y., Wall, E. van de, Laplante, M., Azzara, A., Trujillo, M.E., Hofmann, S.M., Schraw, T., Durand, J.L., Li, H., Li, G., Jelicks, L.A., Mehler, M.F., Hui, D.Y., Deshaies, Y., Shulman, G.I., Schwartz, G.J., Scherer, P.E., (2007). Obesity-associated improvements in metabolic profile through expansion of adipose tissue. *J Clin Invest* 117, 2621–2637. https://doi.org/10.1172/JCI31021

Klein, S., Allison, D.B., Heymsfield, S.B., Kelley, D.E., Leibel, R.L., Nonas, C., Kahn, R., (2007). Waist circumference and cardiometabolic risk: a consensus statement from Shaping America's Health: Association for Weight Management and Obesity Prevention; NAASO, The Obesity Society; the American Society for Nutrition; and the American Diabetes Association. *Am J Clin Nutr* 85, 1197–1202.

Kleinert, M., Clemmensen, C., Hofmann, S.M., Moore, M.C., Renner, S., Woods, S.C., Huypens, P., Beckers, J., de Angelis, M.H., Schürmann, A., Bakhti, M., Klingenspor, M., Heiman, M., Cherrington, A.D., Ristow, M., Lickert, H., Wolf, E., Havel, P.J., Müller, T.D., Tschöp, M.H., (2018). Animal models of obesity and diabetes mellitus. *Nature Reviews Endocrinology* 14, 140–162. https://doi.org/10.1038/nrendo.2017.161

Klöting, N., Fasshauer, M., Dietrich, A., Kovacs, P., Schön, M.R., Kern, M., Stumvoll, M., Blüher, M., (2010). Insulin-sensitive obesity. *American Journal of Physiology - Endocrinology and Metabolism* 299, E506–E515. https://doi.org/10.1152/ajpendo.00586.2009

Kobe, B., Deisenhofer, J., (1994). The leucine-rich repeat: a versatile binding motif. *Trends in Biochemical Sciences* 19, 415–421. https://doi.org/10.1016/0968-0004(94)90090-6

Koeck, E.S., Iordanskaia, T., Sevilla, S., Ferrante, S.C., Hubal, M.J., Freishtat, R.J., Nadler, E.P., (2014). Adipocyte exosomes induce transforming growth factor beta pathway dysregulation in hepatocytes: a novel paradigm for obesity-related liver disease. *Journal of Surgical Research* 192, 268–275. https://doi.org/10.1016/j.jss.2014.06.050

Krogager, T.P., Ernst, R.J., Elliott, T.S., Calo, L., Beránek, V., Ciabatti, E., Spillantini, M.G., Tripodi, M., Hastings, M.H., Chin, J.W., (2018). Labeling and identifying cell-specific proteomes in the mouse brain. *Nature Biotechnology* 36, 156–159. https://doi.org/10.1038/nbt.4056

Krogh, A., Larsson, B., von Heijne, G., Sonnhammer, E.L.L., (2001). Predicting transmembrane protein topology with a hidden markov model: application to complete genomes11Edited by F. Cohen. Journal of Molecular Biology 305, 567–580. https://doi.org/10.1006/jmbi.2000.4315

Lackey, D.E., Olefsky, J.M., (2016). Regulation of metabolism by the innate immune system. *Nature Reviews Endocrinology* 12, 15–28. https://doi.org/10.1038/nrendo.2015.189

Lazar, I., Clement, E., Dauvillier, S., Milhas, D., Ducoux-Petit, M., LeGonidec, S., Moro, C., Soldan, V., Dalle, S., Balor, S., Golzio, M., Burlet-Schiltz, O., Valet, P., Muller, C., Nieto, L., (2016). Adipocyte Exosomes Promote Melanoma Aggressiveness through Fatty Acid Oxidation: A Novel Mechanism Linking Obesity and Cancer. *Cancer Res* 76, 4051–4057. https://doi.org/10.1158/0008-5472.CAN-16-0651

Lee, P., Smith, S., Linderman, J., Courville, A.B., Brychta, R.J., Dieckmann, W., Werner, C.D., Chen, K.Y., Celi, F.S., (2014). Temperature-Acclimated Brown Adipose Tissue Modulates Insulin Sensitivity in Humans. *Diabetes* 63, 3686–3698. https://doi.org/10.2337/db14-0513

Lee, J.-E., Moon, P.-G., Lee, I.-K., Baek, M.-C., (2015). Proteomic Analysis of Extracellular Vesicles Released by Adipocytes of Otsuka Long-Evans Tokushima Fatty (OLETF) Rats. *Protein J* 34, 220–235. https://doi.org/10.1007/s10930-015-9616-z

Liu, X., Kim, C.N., Yang, J., Jemmerson, R., Wang, X., (1996). Induction of Apoptotic Program in Cell-Free Extracts: Requirement for dATP and Cytochrome c. *Cell* 86, 147–157. https://doi.org/10.1016/S0092-8674(00)80085-9

Lo, J.C., Ljubicic, S., Leibiger, B., Kern, M., Leibiger, I.B., Moede, T., Kelly, M.E., Chatterjee Bhowmick, D., Murano, I., Cohen, P., Banks, A.S., Khandekar, M.J., Dietrich, A., Flier, J.S., Cinti, S., Blüher, M., Danial, N.N., Berggren, P.-O., Spiegelman, B.M., (2014). Adipsin Is an

Adipokine that Improves β Cell Function in Diabetes. *Cell* 158, 41–53. https://doi.org/10.1016/j.cell.2014.06.005

Long, J.Z., Svensson, K.J., Bateman, L.A., Lin, H., Kamenecka, T., Lokurkar, I.A., Lou, J., Rao, R.R., Chang, M.R., Jedrychowski, M.P., Paulo, J.A., Gygi, S.P., Griffin, P.R., Nomura, D.K., Spiegelman, B.M., (2016). The Secreted Enzyme PM20D1 Regulates Lipidated Amino Acid Uncouplers of Mitochondria. *Cell* 166, 424–435. https://doi.org/10.1016/j.cell.2016.05.071

Lumeng, C.N., Bodzin, J.L., Saltiel, A.R., (2007). Obesity induces a phenotypic switch in adipose tissue macrophage polarization. *J Clin Invest* 117, 175–184. https://doi.org/10.1172/JCI29881

Luo, J., Deng, Z.-L., Luo, X., Tang, N., Song, W.-X., Chen, J., Sharff, K.A., Luu, H.H., Haydon, R.C., Kinzler, K.W., Vogelstein, B., He, T.-C., (2007). A protocol for rapid generation of recombinant adenoviruses using the AdEasy system. *Nat. Protocols* 2, 1236–1247. https://doi.org/10.1038/nprot.2007.135

Maffei, M., Halaas, J., Ravussin, E., Pratley, R.E., Lee, G.H., Zhang, Y., Fei, H., Kim, S., Lallone, R., Ranganathan, S., Kern, P.A., Friedman, J.M., (1995). Leptin levels in human and rodent: Measurement of plasma leptin and ob RNA in obese and weight-reduced subjects. *Nature Medicine* 1, 1155–1161. https://doi.org/10.1038/nm1195-1155

Manjasetty, B.A., Büssow, K., Fieber-Erdmann, M., Roske, Y., Gobom, J., Scheich, C., Götz, F., Niesen, F.H., Heinemann, U., (2006). Crystal structure of Homo sapiens PTD012 reveals a zinc-containing hydrolase fold. *Protein Sci* 15, 914–920. https://doi.org/10.1110/ps.052037006

Masters, R.K., Reither, E.N., Powers, D.A., Yang, Y.C., Burger, A.E., Link, B.G., (2013). The Impact of Obesity on US Mortality Levels: The Importance of Age and Cohort Factors in Population Estimates. *Am J Public Health* 103, 1895–1901. https://doi.org/10.2105/AJPH.2013.301379

McClatchy, D.B., Ma, Y., Liu, C., Stein, B.D., Martínez-Bartolomé, S., Vasquez, D., Hellberg, K., Shaw, R.J., Yates, J.R., (2015). Pulsed Azidohomoalanine Labeling in Mammals (PALM) Detects Changes in Liver-Specific LKB1 Knockout Mice. *J. Proteome Res.* 14, 4815–4822. https://doi.org/10.1021/acs.jproteome.5b00653

Moraes-Vieira, P.M., Saghatelian, A., Kahn, B.B., (2016). GLUT4 Expression in Adipocytes Regulates De Novo Lipogenesis and Levels of a Novel Class of Lipids With Antidiabetic and Anti-inflammatory Effects. *Diabetes* 65, 1808–1815. https://doi.org/10.2337/db16-0221

Naka, T., Fujimoto, M., (2018). LRG is a novel inflammatory marker clinically useful for the evaluation of disease activity in rheumatoid arthritis and inflammatory bowel disease. *Immunological Medicine* 41, 62–67. https://doi.org/10.1080/13497413.2018.1481582

Newman, A.M., Steen, C.B., Liu, C.L., Gentles, A.J., Chaudhuri, A.A., Scherer, F., Khodadoust, M.S., Esfahani, M.S., Luca, B.A., Steiner, D., Diehn, M., Alizadeh, A.A., (2019). Determining

cell type abundance and expression from bulk tissues with digital cytometry. *Nature Biotechnology* 37, 773–782. https://doi.org/10.1038/s41587-019-0114-2

Ogawa, R., Tanaka, C., Sato, M., Nagasaki, H., Sugimura, K., Okumura, K., Nakagawa, Y., Aoki, N., (2010). Adipocyte-derived microvesicles contain RNA that is transported into macrophages and might be secreted into blood circulation. *Biochemical and Biophysical Research Communications* 398, 723–729. https://doi.org/10.1016/j.bbrc.2010.07.008

Oh, D.Y., Morinaga, H., Talukdar, S., Bae, E.J., Olefsky, J.M., (2012). Increased Macrophage Migration Into Adipose Tissue in Obese Mice. *Diabetes* 61, 346–354. https://doi.org/10.2337/db11-0860

Ohno, H., Shinoda, K., Ohyama, K., Sharp, L.Z., Kajimura, S., (2013). EHMT1 controls brown adipose cell fate and thermogenesis through the PRDM16 complex. *Nature* 504, 163–167. https://doi.org/10.1038/nature12652

Oral, E.A., Simha, V., Ruiz, E., Andewelt, A., Premkumar, A., Snell, P., Wagner, A.J., DePaoli, A.M., Reitman, M.L., Taylor, S.I., Gorden, P., Garg, A., (2002). Leptin-Replacement Therapy for Lipodystrophy. *New England Journal of Medicine* 346, 570–578. https://doi.org/10.1056/NEJMoa012437

Ohashi, K., Shibata, R., Murohara, T., Ouchi, N., (2014). Role of anti-inflammatory adipokines in obesity-related diseases. *Trends in Endocrinology & Metabolism* 25, 348–355. https://doi.org/10.1016/j.tem.2014.03.009

Ouchi, N., Parker, J.L., Lugus, J.J., Walsh, K., (2011). Adipokines in inflammation and metabolic disease. *Nat Rev Immunol* 11, 85–97. https://doi.org/10.1038/nri2921

Pek, S.L.T., Cheng, A.K.S., Lin, M.X., Wong, M.S., Chan, E.Z.L., Moh, A.M.C., Sum, C.F., Lim, S.C., Tavintharan, S., (2018). Association of circulating proinflammatory marker, leucine-rich-α2-glycoprotein (LRG1), following metabolic/bariatric surgery. *Diabetes/Metabolism Research and Reviews* 34, e3029. https://doi.org/10.1002/dmrr.3029

Peyrou, M., Cereijo, R., Quesada-López, T., Campderrós, L., Gavaldà-Navarro, A., Liñares-Pose, L., Kaschina, E., Unger, T., López, M., Giralt, M., Villarroya, F., (2020). The kallikrein–kinin pathway as a mechanism for auto-control of brown adipose tissue activity. *Nature Communications* 11, 2132. https://doi.org/10.1038/s41467-020-16009-x

Phoonsawat, W., Aoki-Yoshida, A., Tsuruta, T., Sonoyama, K., (2014). Adiponectin is partially associated with exosomes in mouse serum. *Biochemical and Biophysical Research Communications* 448, 261–266. https://doi.org/10.1016/j.bbrc.2014.04.114

Pierleoni, A., Martelli, P.L., Casadio, R., (2008). PredGPI: a GPI-anchor predictor. *BMC Bioinformatics* 9, 392. https://doi.org/10.1186/1471-2105-9-392

Poirier, P., Giles, T.D., Bray, G.A., Hong, Y., Stern, J.S., Pi-Sunyer, F.X., Eckel, R.H., (2006). Obesity and Cardiovascular Disease: Pathophysiology, Evaluation, and Effect of Weight Loss. *Circulation* 113, 898–918. https://doi.org/10.1161/CIRCULATIONAHA.106.171016

Porter, S.A., Massaro, J.M., Hoffmann, U., Vasan, R.S., O'Donnel, C.J., Fox, C.S., (2009). Abdominal Subcutaneous Adipose Tissue: A Protective Fat Depot? *Diabetes Care* 32, 1068–1075. https://doi.org/10.2337/dc08-2280

Radhakrishnan, J., Wang, S., Ayoub, I.M., Kolarova, J.D., Levine, R.F., Gazmuri, R.J., (2007). Circulating levels of cytochrome c after resuscitation from cardiac arrest: a marker of mitochondrial injury and predictor of survival. *American Journal of Physiology-Heart and Circulatory Physiology* 292, H767–H775. https://doi.org/10.1152/ajpheart.00468.2006

Randle, P.J., Garland, P.B., Hales, C.N., Newsholme, E.A., (1963). THE GLUCOSE FATTY-ACID CYCLE ITS ROLE IN INSULIN SENSITIVITY AND THE METABOLIC DISTURBANCES OF DIABETES MELLITUS. *The Lancet* 281, 785–789. https://doi.org/10.1016/S0140-6736(63)91500-9

Rappsilber, J., Mann, M., Ishihama, Y., (2007). Protocol for micro-purification, enrichment, pre-fractionation and storage of peptides for proteomics using StageTips. *Nature Protocols* 2, 1896–1906. https://doi.org/10.1038/nprot.2007.261

Raposo, G., Stoorvogel, W., (2013). Extracellular vesicles: Exosomes, microvesicles, and friends. *J Cell Biol* 200, 373–383. https://doi.org/10.1083/jcb.201211138
Renz, A., Berdel, W.E., Kreuter, M., Belka, C., Schulze-Osthoff, K., Los, M., (2001). Rapid extracellular release of cytochrome c is specific for apoptosis and marks cell death in vivo. *Blood* 98, 1542–1548. https://doi.org/10.1182/blood.V98.5.1542

Revollo, J.R., Körner, A., Mills, K.F., Satoh, A., Wang, T., Garten, A., Dasgupta, B., Sasaki, Y., Wolberger, C., Townsend, R.R., Milbrandt, J., Kiess, W., Imai, S., (2007). Nampt/PBEF/Visfatin Regulates Insulin Secretion in β Cells as a Systemic NAD Biosynthetic Enzyme. *Cell Metabolism* 6, 363–375. https://doi.org/10.1016/j.cmet.2007.09.003

Ritchie, M.E., Phipson, B., Wu, D., Hu, Y., Law, C.W., Shi, W., Smyth, G.K., (2015). limma powers differential expression analyses for RNA-sequencing and microarray studies. *Nucleic Acids Research* 43, e47–e47. https://doi.org/10.1093/nar/gkv007

Roca-Rivada, A., Belen Bravo, S., Pérez-Sotelo, D., Alonso, J., Isabel Castro, A., Baamonde, I., Baltar, J., Casanueva, F.F., Pardo, M., (2015). CILAIR-Based Secretome Analysis of Obese Visceral and Subcutaneous Adipose Tissues Reveals Distinctive ECM Remodeling and Inflammation Mediators. *Scientific Reports* 5, 12214. https://doi.org/10.1038/srep12214

Roden, M., Price, T.B., Perseghin, G., Petersen, K.F., Rothman, D.L., Cline, G.W., Shulman, G.I., (1996). Mechanism of free fatty acid-induced insulin resistance in humans. *J Clin Invest* 97, 2859–2865. https://doi.org/10.1172/JCI118742

Rongvaux, A., Shea, R.J., Mulks, M.H., Gigot, D., Urbain, J., Leo, O., Andris, F., (2002). Pre-B-cell colony-enhancing factor, whose expression is up-regulated in activated lymphocytes, is a nicotinamide phosphoribosyltransferase, a cytosolic enzyme involved in NAD biosynthesis. *Eur. J. Immunol*. 32, 3225–3234. https://doi.org/10.1002/1521-4141(200211)32:11<3225::AID-IMMU3225>3.0.CO;2-L

Rosen, B.S., Cook, K.S., Yaglom, J., Groves, D.L., Volanakis, J.E., Damm, D., White, T., Spiegelman, B.M., (1989). Adipsin and complement factor D activity: an immune-related defect in obesity. *Science* 244, 1483–1487. https://doi.org/10.1126/science.2734615

Rosen, E.D., Spiegelman, B.M., (2014). What We Talk About When We Talk About Fat. *Cell* 156, 20–44. https://doi.org/10.1016/j.cell.2013.12.012

Saltiel, A.R., Olefsky, J.M., (2017). Inflammatory mechanisms linking obesity and metabolic disease. *J Clin Invest* 127, 1–4. https://doi.org/10.1172/JCI92035

Samal, B., Sun, Y., Stearns, G., Xie, C., Suggs, S., McNiece, I., (1994). Cloning and characterization of the cDNA encoding a novel human pre-B-cell colony-enhancing factor. Mol. Cell. Biol. 14, 1431–1437. https://doi.org/10.1128/MCB.14.2.1431

Scherer, P.E., Williams, S., Fogliano, M., Baldini, G., Lodish, H.F., (1995). A Novel Serum Protein Similar to C1q, Produced Exclusively in Adipocytes (*). *Journal of Biological Chemistry* 270, 26746–26749. https://doi.org/10.1074/jbc.270.45.26746

Schwanhäusser, B., Busse, D., Li, N., Dittmar, G., Schuchhardt, J., Wolf, J., Chen, W., Selbach, M., (2011). Global quantification of mammalian gene expression control. *Nature* 473, 337–342. https://doi.org/10.1038/nature10098

Shao, M., Wang, Q.A., Song, A., Vishvanath, L., Busbuso, N.C., Scherer, P.E., Gupta, R.K., (2019). Cellular Origins of Beige Fat Cells Revisited. *Diabetes* 68, 1874–1885. https://doi.org/10.2337/db19-0308

Sharp, L.Z., Shinoda, K., Ohno, H., Scheel, D.W., Tomoda, E., Ruiz, L., Hu, H., Wang, L., Pavlova, Z., Gilsanz, V., Kajimura, S., (2012). Human BAT Possesses Molecular Signatures That Resemble Beige/Brite Cells. *PLOS ONE* 7, e49452. https://doi.org/10.1371/journal.pone.0049452

Shepherd, P.R., Gnudi, L., Tozzo, E., Yang, H., Leach, F., Kahn, B.B., (1993). Adipose cell hyperplasia and enhanced glucose disposal in transgenic mice overexpressing GLUT4 selectively in adipose tissue. *J. Biol. Chem.* 268, 22243–22246.

Shi, H., Strader, A.D., Woods, S.C., Seeley, R.J., (2007). The effect of fat removal on glucose tolerance is depot specific in male and female mice. *American Journal of Physiology-Endocrinology and Metabolism* 293, E1012–E1020. https://doi.org/10.1152/ajpendo.00649.2006

Shin, J.-B., Krey, J.F., Hassan, A., Metlagel, Z., Tauscher, A.N., Pagana, J.M., Sherman, N.E., Jeffery, E.D., Spinelli, K.J., Zhao, H., Wilmarth, P.A., Choi, D., David, L.L., Auer, M., Barr-Gillespie, P.G., (2013). Molecular architecture of the chick vestibular hair bundle. *Nature Neuroscience* 16, 365–374. https://doi.org/10.1038/nn.3312

Shinoda, K., Luijten, I.H.N., Hasegawa, Y., Hong, H., Sonne, S.B., Kim, M., Xue, R., Chondronikola, M., Cypess, A.M., Tseng, Y.-H., Nedergaard, J., Sidossis, L.S., Kajimura, S., (2015). Genetic and functional characterization of clonally derived adult human brown adipocytes. *Nature Medicine* 21, 389–394. https://doi.org/10.1038/nm.3819

Shirai, R., Hirano, F., Ohkura, N., Ikeda, K., Inoue, S., (2009). Up-regulation of the expression of leucine-rich α2-glycoprotein in hepatocytes by the mediators of acute-phase response. *Biochemical and Biophysical Research Communications* 382, 776–779. https://doi.org/10.1016/j.bbrc.2009.03.104

Shirai, R., Gotou, R., Hirano, F., Ikeda, K., Inoue, S., (2010). Autologous Extracellular Cytochrome c Is an Endogenous Ligand for Leucine-rich α2-Glycoprotein and β-Type Phospholipase A2 Inhibitor. *J. Biol. Chem*. 285, 21607–21614. https://doi.org/10.1074/jbc.M110.122788

Shola, D.T.N., Yang, C., Han, C., Norinsky, R., Peraza, R.D., (2021). Generation of Mouse Model (KI and CKO) via Easi-CRISPR, in: Singh, S.R., Hoffman, R.M., Singh, A. (Eds.), *Mouse Genetics : Methods and Protocols, Methods in Molecular Biology*. Springer US, New York, NY, pp. 1–27. https://doi.org/10.1007/978-1-0716-1008-4_1

Souza, C.O., Teixeira, A.A.S., Biondo, L.A., Silveira, L.S., Calder, P., Rosa Neto, J.C., (2017). Palmitoleic acid reduces the inflammation in LPS stimulated macrophages by inhibition of NFκB, independently of PPARs. *Clin Exp Pharmacol Physiol* https://doi.org/10.1111/1440-1681.12736

Strissel, K.J., Stancheva, Z., Miyoshi, H., Perfield, J.W., DeFuria, J., Jick, Z., Greenberg, A.S., Obin, M.S., (2007). Adipocyte Death, Adipose Tissue Remodeling, and Obesity Complications. *Diabetes* 56, 2910–2918. https://doi.org/10.2337/db07-0767

Stromsdorfer, K.L., Yamaguchi, S., Yoon, M.J., Moseley, A.C., Franczyk, M.P., Kelly, S.C., Qi, N., Imai, S., Yoshino, J., (2016). NAMPT-mediated NAD+ biosynthesis in adipocytes regulates adipose tissue function and multi-organ insulin sensitivity in mice. *Cell Rep* 16, 1851–1860. https://doi.org/10.1016/j.celrep.2016.07.027

Su, A.I., Wiltshire, T., Batalov, S., Lapp, H., Ching, K.A., Block, D., Zhang, J., Soden, R., Hayakawa, M., Kreiman, G., Cooke, M.P., Walker, J.R., Hogenesch, J.B., (2004). A gene atlas of the mouse and human protein-encoding transcriptomes. *PNAS* 101, 6062–6067. https://doi.org/10.1073/pnas.0400782101

Svensson, K.J., Long, J.Z., Jedrychowski, M.P., Cohen, P., Lo, J.C., Serag, S., Kir, S., Shinoda, K., Tartaglia, J.A., Rao, R.R., Chédotal, A., Kajimura, S., Gygi, S.P., Spiegelman, B.M., (2016).

A Secreted Slit2 Fragment Regulates Adipose Tissue Thermogenesis and Metabolic Function. *Cell Metabolism* 23, 454–466. https://doi.org/10.1016/j.cmet.2016.01.008

Takenouchi, T., Tsukimoto, M., Iwamaru, Y., Sugama, S., Sekiyama, K., Sato, M., Kojima, S., Hashimoto, M., Kitani, H., (2015). Extracellular ATP induces unconventional release of glyceraldehyde-3-phosphate dehydrogenase from microglial cells. *Immunology Letters* 167, 116–124. https://doi.org/10.1016/j.imlet.2015.08.002

Tchkonia, T., Thomou, T., Zhu, Y., Karagiannides, I., Pothoulakis, C., Jensen, M.D., Kirkland, J.L., (2013). Mechanisms and Metabolic Implications of Regional Differences among Fat Depots. *Cell Metabolism* 17, 644–656. https://doi.org/10.1016/j.cmet.2013.03.008

Thomou, T., Mori, M.A., Dreyfuss, J.M., Konishi, M., Sakaguchi, M., Wolfrum, C., Rao, T.N., Winnay, J.N., Garcia-Martin, R., Grinspoon, S.K., Gorden, P., Kahn, C.R., (2017). Adipose-derived circulating miRNAs regulate gene expression in other tissues. *Nature* 542, 450–455. https://doi.org/10.1038/nature21365

Tojo, A., Endou, H., (1992). Intrarenal handling of proteins in rats using fractional micropuncture technique. *American Journal of Physiology-Renal Physiology* 263, F601–F606. https://doi.org/10.1152/ajprenal.1992.263.4.F601

Trak-Smayra, V., Paradis, V., Massart, J., Nasser, S., Jebara, V., Fromenty, B., (2011). Pathology of the liver in obese and diabetic ob/ob and db/db mice fed a standard or high-calorie diet. *International Journal of Experimental Pathology* 92, 413‐421. https://doi.org/10.1111/j.1365-2613.2011.00793.x

Tran, T.T., Yamamoto, Y., Gesta, S., Kahn, C.R., (2008). Beneficial Effects of Subcutaneous Fat Transplantation on Metabolism. *Cell Metabolism* 7, 410–420. https://doi.org/10.1016/j.cmet.2008.04.004

Tyanova, S., Temu, T., Sinitcyn, P., Carlson, A., Hein, M.Y., Geiger, T., Mann, M., Cox, J., (2016). The Perseus computational platform for comprehensive analysis of (prote)omics data. *Nature Methods* 13, 731–740. https://doi.org/10.1038/nmeth.3901

van Marken Lichtenbelt, W.D., Vanhommerig, J.W., Smulders, N.M., Drossaerts, J.M.A.F.L., Kemerink, G.J., Bouvy, N.D., Schrauwen, P., Teule, G.J.J., (2009). Cold-Activated Brown Adipose Tissue in Healthy Men. *New England Journal of Medicine* 360, 1500–1508. https://doi.org/10.1056/NEJMoa0808718

Vasiliauskaité-Brooks, I., Sounier, R., Rochaix, P., Bellot, G., Fortier, M., Hoh, F., De Colibus, L., Bechara, C., Saied, E.M., Arenz, C., Leyrat, C., Granier, S., (2017). Structural insights into adiponectin receptors suggest ceramidase activity. *Nature* 544, 120–123. https://doi.org/10.1038/nature21714

Villarroya, F., Cereijo, R., Villarroya, J., Giralt, M., (2017). Brown adipose tissue as a secretory organ. *Nat Rev Endocrinol* 13, 26–35. https://doi.org/10.1038/nrendo.2016.136

Virtanen, K.A., Lidell, M.E., Orava, J., Heglind, M., Westergren, R., Niemi, T., Taittonen, M., Laine, J., Savisto, N.-J., Enerbäck, S., Nuutila, P., (2009). Functional Brown Adipose Tissue in Healthy Adults. *New England Journal of Medicine* 360, 1518–1525. https://doi.org/10.1056/NEJMoa0808949

Wang, X., Abraham, S., McKenzie, J.A.G., Jeffs, N., Swire, M., Tripathi, V.B., Luhmann, U.F.O., Lange, C.A.K., Zhai, Z., Arthur, H.M., Bainbridge, J.W.B., Moss, S.E., Greenwood, J., (2013). LRG1 promotes angiogenesis by modulating endothelial TGF-β signalling. *Nature* 499, nature12345. https://doi.org/10.1038/nature12345

Wang, Z.V., Scherer, P.E., (2016). Adiponectin, the past two decades. *Journal of Molecular Cell Biology* 8, 93–100. https://doi.org/10.1093/jmcb/mjw011

Wang, W., Seale, P., (2016). Control of brown and beige fat development. *Nat Rev Mol Cell Biol* 17, 691–702. https://doi.org/10.1038/nrm.2016.96

Wang, P., Loh, K.H., Wu, M., Morgan, D.A., Schneeberger, M., Yu, X., Chi, J., Kosse, C., Kim, D., Rahmouni, K., Cohen, P., Friedman, J., (2020). A leptin–BDNF pathway regulating sympathetic innervation of adipose tissue. *Nature* 583, 839–844. https://doi.org/10.1038/s41586-020-2527-y

Ward, Z.J., Bleich, S.N., Cradock, A.L., Barrett, J.L., Giles, C.M., Flax, C., Long, M.W., Gortmaker, S.L., (2019). Projected U.S. State-Level Prevalence of Adult Obesity and Severe Obesity. *New England Journal of Medicine* 381, 2440–2450. https://doi.org/10.1056/NEJMsa1909301

Wei, W., Riley, N.M., Yang, A.C., Kim, J.T., Terrell, S.M., Li, V.L., Garcia-Contreras, M., Bertozzi, C.R., Long, J.Z., (2021). Cell type-selective secretome profiling in vivo. *Nature Chemical Biology* 17, 326–334. https://doi.org/10.1038/s41589-020-00698-y

Weisberg, S.P., McCann, D., Desai, M., Rosenbaum, M., Leibel, R.L., Ferrante, A.W., (2003). Obesity is associated with macrophage accumulation in adipose tissue. *J Clin Invest* 112, 1796–1808. https://doi.org/10.1172/JCI19246

Wenzel, T.J., Bajwa, E., Klegeris, A., (2019). Cytochrome c can be released into extracellular space and modulate functions of human astrocytes in a toll-like receptor 4-dependent manner. *Biochimica et Biophysica Acta (BBA) - General Subjects* 1863, 129400. https://doi.org/10.1016/j.bbagen.2019.07.009

Winzell, M.S., Ahrén, B., (2004). The High-Fat Diet–Fed Mouse: A Model for Studying Mechanisms and Treatment of Impaired Glucose Tolerance and Type 2 Diabetes. *Diabetes* 53, S215–S219. https://doi.org/10.2337/diabetes.53.suppl_3.S215

Wu, C., Orozco, C., Boyer, J., Leglise, M., Goodale, J., Batalov, S., Hodge, C.L., Haase, J., Janes, J., Huss, J.W., Su, A.I., (2009). BioGPS: an extensible and customizable portal for

querying and organizing gene annotation resources. *Genome Biology* 10, R130. https://doi.org/10.1186/gb-2009-10-11-r130

Wu, J., Boström, P., Sparks, L.M., Ye, L., Choi, J.H., Giang, A.-H., Khandekar, M., Virtanen, K.A., Nuutila, P., Schaart, G., Huang, K., Tu, H., van Marken Lichtenbelt, W.D., Hoeks, J., Enerbäck, S., Schrauwen, P., Spiegelman, B.M., (2012). Beige Adipocytes Are a Distinct Type of Thermogenic Fat Cell in Mouse and Human. *Cell* 150, 366–376. https://doi.org/10.1016/j.cell.2012.05.016

Wu, C., MacLeod, I., Su, A.I., (2013). BioGPS and MyGene.info: organizing online, gene-centric information. *Nucleic Acids Research* 41, D561–D565. https://doi.org/10.1093/nar/gks1114

Wu, C., Jin, X., Tsueng, G., Afrasiabi, C., Su, A.I., (2016). BioGPS: building your own mash-up of gene annotations and expression profiles. *Nucleic Acids Research* 44, D313–D316. https://doi.org/10.1093/nar/gkv1104

Xu, A., Wang, Y., Xu, J.Y., Stejskal, D., Tam, S., Zhang, J., Wat, N.M.S., Wong, W.K., Lam, K.S.L., (2006). Adipocyte Fatty Acid–Binding Protein Is a Plasma Biomarker Closely Associated with Obesity and Metabolic Syndrome. *Clinical Chemistry* 52, 405–413. https://doi.org/10.1373/clinchem.2005.062463

Yamauchi, T., Kamon, J., Ito, Y., Tsuchida, A., Yokomizo, T., Kita, S., Sugiyama, T., Miyagishi, M., Hara, K., Tsunoda, M., Murakami, K., Ohteki, T., Uchida, S., Takekawa, S., Waki, H., Tsuno, N.H., Shibata, Y., Terauchi, Y., Froguel, P., Tobe, K., Koyasu, S., Taira, K., Kitamura, T., Shimizu, T., Nagai, R., Kadowaki, T., (2003). Cloning of adiponectin receptors that mediate antidiabetic metabolic effects. *Nature* 423, 762–769. https://doi.org/10.1038/nature01705

Yang, Q., Graham, T.E., Mody, N., Preitner, F., Peroni, O.D., Zabolotny, J.M., Kotani, K., Quadro, L., Kahn, B.B., (2005). Serum retinol binding protein 4 contributes to insulin resistance in obesity and type 2 diabetes. *Nature* 436, 356–362. https://doi.org/10.1038/nature03711

Yang, Z.-H., Miyahara, H., Hatanaka, A., (2011). Chronic administration of palmitoleic acid reduces insulin resistance and hepatic lipid accumulation in KK-Ay Mice with genetic type 2 diabetes. *Lipids in Health and Disease* 10, 120. https://doi.org/10.1186/1476-511X-10-120

Yilmaz, M., Claiborn, K.C., Hotamisligil, G.S., (2016). De Novo Lipogenesis Products and Endogenous Lipokines. *Diabetes* 65, 1800–1807. https://doi.org/10.2337/db16-0251

Yoneshiro, T., Aita, S., Matsushita, M., Kameya, T., Nakada, K., Kawai, Y., Saito, M., (2011). Brown Adipose Tissue, Whole-Body Energy Expenditure, and Thermogenesis in Healthy Adult Men. *Obesity* 19, 13–16. https://doi.org/10.1038/oby.2010.105

Yoon, M.J., Yoshida, M., Johnson, S., Takikawa, A., Usui, I., Tobe, K., Nakagawa, T., Yoshino, J., Imai, S., (2015). SIRT1-Mediated eNAMPT Secretion from Adipose Tissue Regulates

Hypothalamic NAD+ and Function in Mice. *Cell Metabolism* 21, 706–717. https://doi.org/10.1016/j.cmet.2015.04.002

Yore, M.M., Syed, I., Moraes-Vieira, P.M., Zhang, T., Herman, M.A., Homan, E.A., Patel, R.T., Lee, J., Chen, S., Peroni, O.D., Dhaneshwar, A.S., Hammarstedt, A., Smith, U., McGraw, T.E., Saghatelian, A., Kahn, B.B., (2014). Discovery of a Class of Endogenous Mammalian Lipids with Anti-Diabetic and Anti-inflammatory Effects. *Cell* 159, 318–332. https://doi.org/10.1016/j.cell.2014.09.035

Yu, G., Wang, L.-G., Han, Y., He, Q.-Y., (2012). clusterProfiler: an R Package for Comparing Biological Themes Among Gene Clusters. *OMICS: A Journal of Integrative Biology* 16, 284–287. https://doi.org/10.1089/omi.2011.0118

Zhang, Y., Proenca, R., Maffei, M., Barone, M., Leopold, L., Friedman, J.M., (1994). Positional cloning of the mouse obese gene and its human homologue. *Nature* 372, 425–432. https://doi.org/10.1038/372425a0

Zhang, J., Li, S., Li, L., Li, M., Guo, C., Yao, J., Mi, S., (2015). Exosome and Exosomal MicroRNA: Trafficking, Sorting, and Function. *Genomics, Proteomics & Bioinformatics* 13, 17–24. https://doi.org/10.1016/j.gpb.2015.02.001

Zeng, X., Ye, M., Resch, J.M., Jedrychowski, M.P., Hu, B., Lowell, B.B., Ginty, D.D., Spiegelman, B.M., (2019). Innervation of thermogenic adipose tissue via a calsyntenin 3β–S100b axis. *Nature* 569, 229. https://doi.org/10.1038/s41586-019-1156-9